Studies of Electronic Structure Theory:

Fundamental Understanding of

Chemical Reaction by Transition Metal Complex

and

Exact Solution of Schrödinger and Dirac Equations

Atsushi Ishikawa

2011

Preface

"The underlying physical laws necessary for the mathematical theory of a large part of physics and the whole of chemistry are thus completely known, and the difficulty is only that the exact application of these laws leads to equations much too complicated to be soluble. It therefore becomes desirable that approximate practical methods of applying quantum mechanics should be developed, which can lead to an explanation of the main features of complex atomic systems without too much computation."- P. A. M. Dirac, Proc. R. Soc. Lond. Ser. A. ***1929****, 123, 714.* As shown in the above statement by P. A. M. Dirac, the Schrödinger equation (SE) was believed not to be solved at the early days of the quantum science.

However, thanks to great efforts of excellent physicians and chemists, one can solve the SE based on wave function theory and density functional theory nowadays. Though such solutions are not exact, theoretical and computational insights presented by them are significantly valuable for basic and fundamental understanding of chemical issues. In particular, such theoretical and computational insights are indispensable to make new advancement of chemically interesting systems with complex electronic structure. Transition metal complex is one of such important and chemically interesting systems from both viewpoints of fundamental and applied chemistries. For instance, transition metal complex plays important roles as catalyst in organic synthesis, chemical industry, and biological reactions. To understand correctly their catalyses, we need correct knowledge of the intermediates and transition states. Though it is not easy to experimentally obtain such knowledge of reactive intermediate and transition state, theoretical and computational methods can provide such knowledge. At the same time, we need exact theoretical method to present accurate understanding and correct prediction of the chemical phenomena. This means that we must make a lot of efforts to exactly solve the SE.

In this thesis, the author wishes to report the investigation of the accurate *ab initio* electronic structure theory on chemically important and interesting systems. This thesis

consists of general introduction, part I, part II, and general conclusion. In part I, *ab initio* electronic structure methods are applied to the reactions involving transition metal complexes. The part I contains chapters 1 to 3. In chapter 1, oxygen atom transfer reactions between iridium and osmium complexes are investigated by *ab initio* electronic structure calculations, to clarify the origin of the differences of their reaction rates and reaction behavior. In chapter 2, the C-H bond activation reaction promoted by palladium complex is investigated by DFT and post Hartree-Fock methods to clarify the mechanism of the C-H activation and the role of benzoquinone molecule. In chapter 3, the olefin epoxidation reaction catalyzed by the ruthenium porphyrin is investigated by both single- and multi-reference *ab initio* methods to elucidate the details in the olefin epoxidation reaction. Here, we wish to report the fundamental and deep knowledge of the complex systems based on approximate computational results. In part II, the general method for solving the SE and the Dirac equations (DE) is developed and applied to hydrogen molecular ion and other small molecules. The part II contains chapters 4 and 5. In chapter 4, the nonrelativistic SE and the relativistic DE of H_2^+ are solved accurately in an analytical expansion form by the free-complement method combined with the variational principle. In chapter 5, development of the new general methodology is presented in which calculations of overlap and Hamiltonian integrals are not necessary. By developing this new method called local Schrödinger equation (LSE) method, the free-complement method became applicable to large molecules. Here, we wish to report exact solution of the SE and DE.

The author believes that these results are invaluable for developing accurate theory and reliable application of theoretical computations to chemically important and interesting systems.

Atsushi Ishikawa

2011

Acknowledgements

The studies presented in this thesis were carried out at Department of Synthetic Chemistry and Biological Chemistry, and Department of Molecular Engineering, Graduate School of Engineering, Kyoto University from 2005 to 2010. The author would like to express his deepest appreciation to Professor Shigeyoshi Sakaki for his helpful discussion, useful suggestions and encouragement. His various comments based on theoretical chemistry and physical chemistry was invaluable for this study. The author also expresses the deepest appreciation to Professor Hiroshi Nakatsuji for his helpful discussion and suggestions. The development of theories in this thesis could not be performed without his full corporation. The author would appreciate Professors Hirofumi Sato and Masahiro Ehara, Assistant Professor Yoshihide Nakao, and Lecturer Jun-ya Hasegawa for their valuable comments and suggestions.

The author is also grateful to Dr. Hiroyuki Nakashima for variable suggestions and scientific discussions. Acknowledgement is also presented to all members of the research groups of Prof. Hiroshi Nakatsuji and Prof. Shigeyoshi Sakaki. The discussion with them was stimulative and exciting for the author to induce and activate his motivation of this study.

The author thanks to Japan Society for the Promotion of Science (JSPS) for financial support as Fellowship for Japanese Junior Scents. Finally, the author sincerely thanks to his parents Naoyuki Ishikawa and Nobuko Ishikawa for their understanding, encouragement, and supports.

Atsushi Ishikawa

2011

Contents

General Introduction

1. Importance of Elucidating the Nature of the Chemistry and Developing Accurate Theory

Physical and chemical properties of atoms and molecules are governed by the Schrödinger equation (SE). Because of this, pursuing the methodology to exactly solve the SE is the main subject in the field of quantum chemistry. In these days, *ab initio* quantum chemical calculation methods become indispensable tool for understanding and for predicting of molecular structures, spectroscopic properties, magnetic properties, chemical reactions, and so on.

In order to give reliable theoretical and computational results, various factors like electron correlation effect, non-adiabatic effect *etc.* should be taken into account. Thanks to the recent development of the theoretical methods, algorithms, and computers, theoretical calculations including those factors have become much easier than before. However, the exact solution of the SE has not been calculated yet even nowadays except for very small or model systems; indeed, even computational results by state-of-the-art electron correlation method is still far from the exact solution.

Even if the SE is solved exactly, it is not sufficient yet for the reliable comparison between calculated and experimental results, because the relativistic effects are not considered in the SE. The relativistic effects are especially important for molecules including heavy elements, but even for molecules with light elements, consideration of the relativistic effect is indispensable for correct comparison between theoretical and experimental results. Therefore, the four-component relativistic Dirac or Dirac-Coulomb equations (DE and DCE, respectively) should be solved instead of the SE. Such accurate theoretical method is important not only for the understanding of nature of chemical system but also for presenting

reliable prediction.

On the other hand, such exact solution of SE and DE can be calculated only for small system because of the high computational cost. To perform theoretical calculation of large complex system in reasonable computational cost, various levels of approximation must be introduced. The good examples are Hartree-Fock approximation, functionals in DFT, Gaussian type basis functions, core potential replacing inner-shell electrons, transformation of the four-component DE to the two-component equation, and so on. By employing these approximations, theoretical chemistry can present semi-quantitative computational results. Because of these appropriate approximations, theoretical and computational methods are capable for providing well understanding about many chemical systems and even reliable predictions nowadays.

2. Theoretical Study of Complex Systems Containing Transition Metal Elements

Stoichiometric and catalytic reactions by transition metal complexes have attracted great interests because they play important roles in many metalloenzymes, synthetic chemistry, and chemical industry. In general, catalytic cycles by metal complexes involve several common elementary steps such as substitution, oxidative addition, reductive elimination, σ-bond metathesis, insertion, coupling reaction, and so on. These elementary steps are often found in many catalytic reactions. Thus, quantum chemical knowledge of those elementary steps is necessary to present correct understanding of catalytic reaction, improve catalytic activity, reactivity, and selectivity, find a new catalyst, and construct new catalytic cycle. Indeed, numerous experimental and theoretical studies have been carried out to understand these elementary steps.[1-8] Recent progress in theoretical and computational chemistries has shown that many important problems of those reactions are solved and understood by *ab initio* quantum chemical methods and furthermore prediction is succeeded in several cases.

For many years, extended Hückel MO theory (EHMO) and semi-empirical SCF-MO,

and *ab initio* MO methods have been applied to the transition metal chemistry. These methods successfully explain many phenomena in a qualitative or in semi-quantitative sense.

Since middle of ‘90, the DFT method has become very useful due to Kohn-Sham equation with reliable exchange-correlation functionals. The method is satisfactory accurate in many cases, semi-quantitatively at least, owing to the development of exchange-correlation functional; especially, the hybrid exchange-correlation functional has enlarged the applicability of the DFT method to the transition metal chemistry. However, the DFT method still has several problems; for example, the DFT method cannot be applied to molecules with near degeneracy because it cannot incorporate multi-reference electronic character. Another well known weak point of this method is not to provide reliable results about the dispersion interaction.

Considering the above-mentioned situations, *ab initio* quantum chemical methods play indispensable roles for the theoretical understanding and prediction of geometry, molecular property, and reaction of transition metal complexes. Of course, the appropriate theoretical model should be employed to present reliable computational results. For example, i) oversimplified model for catalysts or substitutes gives rise to various problems because of the neglect of both electronic and steric effects of ligand and substitute. ii) Though the DFT method is very often employed for theoretical and computational studies of transition metal complexes, it cannot be applied to the transition metal complex with near degeneracy, as mentioned above. In such case, the multi-configurational method should be employed instead. And, iii) environmental or statistical factors like solvent effect or entropy effect should be correctly taken into account in the quantum chemical calculations.

Taking these issues account, the use of the proper model systems and computational method is indispensable to present reliable and meaningful theoretical understanding of the geometry, molecular property, and reaction of the transition metal complex.

3. Free-Complement Method – the General Formalism for Solving the Schrödinger and the Dirac Equations

The Schrödinger equation (SE), $H\psi = E\psi$, provides a governing principle of chemistry, physics, and biology. Its exact solution provides correct understanding and prediction of chemical phenomena. However, from its beginning of quantum chemistry, this equation has been believed not to be soluble except for a few limited cases.[9]

To overcome this serious problem in the quantum chemistry, Nakatsuji and coworkers have been formulating a general method to exactly solve the SE of atoms and molecules in analytical expansion form since 2000.[10-16]

First, they clarified the mathematical structure of the exact wave function and proposed a new method, called free complement (FC) method (originally called as iterative complement interaction (ICI) method), that gives a series of functions converging to the exact wave function.

The validity of the FC method was confirmed by applying the method not only to the SE of model systems[17] but also to the SE of atoms and molecules. The FC method, however, inherently includes the integrals of higher powers of the Hamiltonian which diverge when the Hamiltonian involves singular operators like the Coulomb potential.[12-13] This problem, called the singularity problem, always occurs when the FC method is applied to the SE of atoms and molecules. This difficulty has been solved by introducing the inverse Schrödinger equation[12] and the scaled Schrödinger equation (SSE).[13] The method based on the SSE was easier and more general. The SE can be written equivalently in the form of the SSE, as follows:

$$g\left(H-E\right)\psi = 0 \tag{1.1}$$

where g is a function to scale the singularities of the potential to be finite. The simplest ICI (SICI) wave function based on the SSE is represented by eq.1.2

$$\psi_{n+1} = \left[1 + C_n g\left(H - E_n\right)\right]\psi_n \tag{1.2}.$$

This was proved to become exact at convergence[13-14] without encountering the singularity

problem. In order to introduce variational degrees of freedom to the SICI wave function of eq.1.2, the right-hand side of this equation is divided into the independent analytical functions. These functions are called the free complement (FC) functions. Because of the increased freedom, the FC method converges faster to the exact wave function than the original SICI. The variables of the FC wave function are calculated by applying the variational principle.

However, even if the SE is solved exactly, theoretical understanding and prediction of the experimental results are not sufficient since the relativistic effect is not included in the SE. Therefore, the relativistic Dirac equations (DE) should be employed for theoretical calculations. Relativistic effects are responsible for several well-known chemical phenomena; the lanthanide contraction, the properties of coinage metals (Au, Ag, and Cu), the special stability of Hg_2^{2+} ion, the presence of Hg liquid under standard conditions, and so on. All these results indicate that a general theory of atomic and molecular electronic structure must be based on the DE rather than SE. We believe that only such method becomes applicable to all elements of the periodic table. Likewise the SE, the DE can be exactly solved only for one-electron one-center problem. The general procedure for solving DE or the Dirac-Coulomb equation (DCE) which is the many-electron counterpart, has not been established yet. Unfortunately, solving the DE is much more complicated than solving the SE since the wave function consists of four-component spinors. This introduces the so-called "variational collapse" problem; in general, the variational principle does not hold for the relativistic case. Because of these features, the straightforward application of the DE to chemical systems becomes difficult.

The fundamental idea in the FC method is that the wave function should be determined by the Hamiltonian of the system. This encourages us to apply the FC method to the relativistic DE/DCE. The scaled DE/DCE and the SICI wave functions for the DE/DCE have the same form as those of eq.1.1 and eq.1.2 except that the complement function consists of four-component spinor function.

Unlike the non-relativistic case, we also have to solve "variational collapse" problem in the DE. Many studies have been explored to overcome this problem.[18] One important approach to overcome the variational collapse problem is the inverse Hamiltonian method proposed by Hill and Krauthauser,[19] in which the DE is rewritten as eq.1.3:

$$H^{-1}\psi = E^{-1}\psi , \tag{1.3}$$

In the inverse DE, the lowest positive energy state corresponding to the electronic ground state is mapped to the top of the spectrum, i.e., the highest solution against the complete vacuum, and therefore, the following Ritz-like variational principle holds for the inverse Hamiltonian operator.

Generally, the variational collapse arises from an improper, limited representation of the wave function. If the wave function satisfies the proper relationship between the large and small components, known as "atomic balancing condition", the variational collapse does not occur.[20-21] Actually, it is shown that this balancing condition between the large and small components is automatically imposed between those of the adjacent orders in the FC method.[22] This relationship is called as "ICI balance". Thus, within the FC methodology, even the ordinary variational method based on the regular Hamiltonian may give correct variational solutions as far as the order *n* is large enough.

As was discussed above, the FC method is applicable to any problem when the analytic form of the Hamiltonian is defined. However, there are still several problems to be overcome when applying it to chemically interesting systems. The largest one is the "integration difficulty" which is associated with the overlap and Hamiltonian integrals. In principle, analytic integrations are not always possible for arbitrary analytic functions. This is true also for the FC functions. Numerical integration methods cannot be employed from both viewpoints of accuracy and computational cost. Without solving this problem, we cannot apply the present methodology to the SE and DE of general atoms and molecules. Therefore, the method to evaluate the overlap and the Hamiltonian matrices without integration process

must be formulated and developed.

4. Aim of the Present Thesis

In this thesis, the author wishes to report the investigation of the electronic structure theory to overcome the problems mentioned in the previous section. This thesis consists of two parts. In part I, *ab initio* electronic structure calculations based on the DFT and wave function methods are performed for the reactions by transition metal complexes. In part II, the FC method to solve the SE and DE is developed and applied to systems with a few electrons.

In chapter 1, oxygen atom transfer reaction between $Ir(Mes)_3$ and $Ir(Mes)_3$=O (eq.4.1a) and that between $Os(NAr)_3$ and $Os(NAr)_3$=O (eq.4.1b) are investigated by the DFT method.

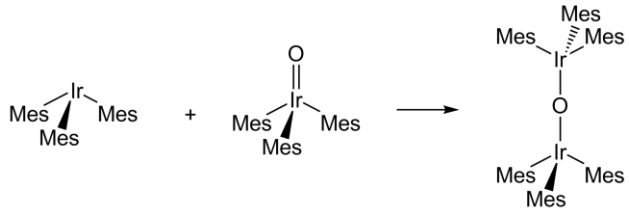

(4.1a)

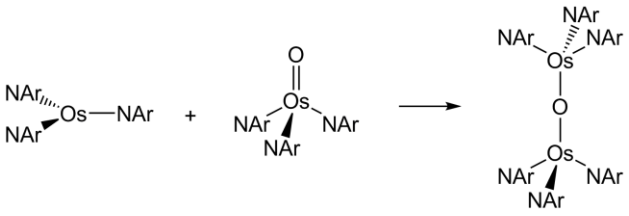

(4.1b)

Experimentally, the oxygen atom transfer reaction easily occurs between $Ir(Mes)_3$ and $Ir(Mes)_3$=O, but does not occur between $Os(NAr)_3$ and $Os(NAr)_3$=O. The reason for this different behavior is not elucidated yet by experimental studies. The structures and the stabilities of the transition state and intermediate are key factor to understand the difference in activation barriers between the iridium and osmium reaction systems. The purposes in this chapter are i) to elucidate what factors induce the difference in the activation barrier between the iridium and osmium reactions, and ii) to make clear comparison between small model and large realistic complexes. The computational results clearly indicate that the small model complexes are insufficient to represent the correct transition state and intermediate of the

iridium and osmium reactions. Also, the author clarified that both electronic and steric factors are important for understanding the difference of activation barriers.

In chapter 2, the C-C bond formation via the C-H bond activation reaction promoted by Pd complex (eq.4.2) is investigated by the DFT and post Hartree-Fock methods.

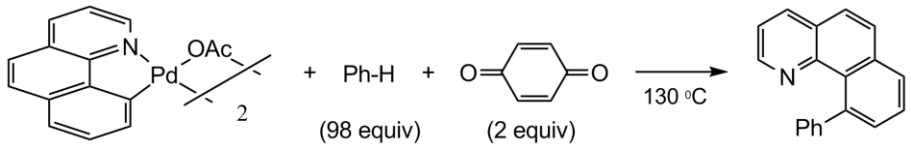

(4.2)

In organometallic chemistry, the C-C bond formation reaction catalyzed by transition metal complex is one of the most important research subjects. From the viewpoint of synthetic chemistry, the cross-coupling reaction of arenes is quite useful.[23-25] However, organic halide are often employed as substrates in the cross-coupling reactions. This is one weak point, because appropriate organic halide must be synthesized. The C-C bond formation via the C-H activation is much more useful, because hydrocarbon compound is directly used for the reaction. In this regard, the result of eq.4.2 is of considerable interest. To make new development of this type of C-C bond formation, theoretical understanding of the reaction mechanism is significantly important. In the arene cross-coupling reaction of eq.4.2, the reaction does not occur in the absence of benzoquinone. Experimentally, the role of benzoquinone has not been elucidated yet. The main purpose here is to clarify the role of benzoquinone in the reaction process. The author investigated the arene cross-coupling reactions both in the presence and the absence of benzoquinone. Also, the comparison between the post Hartree-Fock and DFT methods was made in detail. The present theoretical study leads to clear conclusion that the presence of benzoquinone is favorable for the reductive elimination step both electronically and sterically.

In chapter 3, the olefin epoxidation reaction catalyzed by the ruthenium porphyrins (Scheme 1) was investigated by the DFT and CASSCF methods.

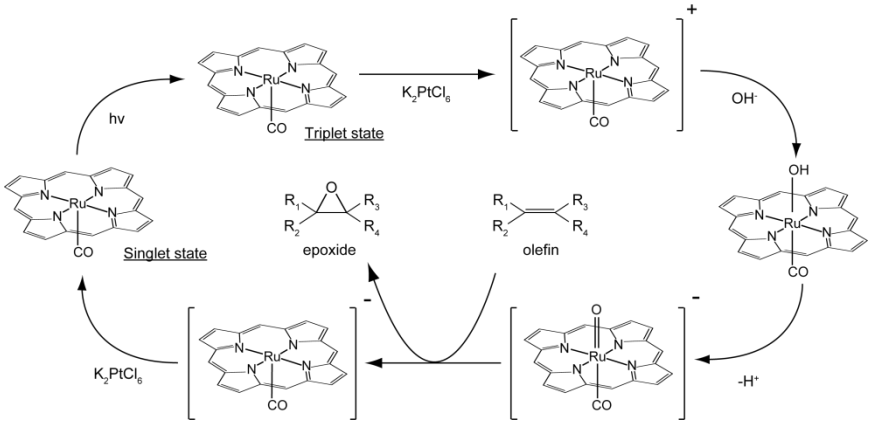

Scheme 1.

A great number of catalytic reactions with remarkable efficiency are found in biological systems.[26-27] In many of them, metalloenzymes play key roles as catalyst.[28-29] The metalloporphyrins are involved in many metalloenzymes as active site. In theoretical chemistry, the metalloporphyrins are also interesting because their ground states often have near-degenerate electronic state. This means that we must be careful for applying such single-reference method as the Hartree-Fock and DFT methods to these molecules. The purposes of this chapter are (i) to clarify the electronic process of their epoxidation reaction, (ii) to make clear comparison between single- and multi-reference methods in metalloporphyrin. Here, the electronic structure of $[Ru(Por)(CO)(O)]^{-}$ was investigated by the DFT and CASSCF methods. It is clearly shown that both methods provide essentially the same electronic structure. After such a detailed comparison, the olefin epoxidation mechanism by $[Ru(Por)(CO)(O)]^{-}$ was mainly investigated by the DFT method. In this work, the author succeeded to present correct understanding of the reaction mechanism based on the charge and spin transfers from the olefin moiety to the porphyrin ring.

In chapter 4, the nonrelativistic SE and the relativistic DE of hydrogen molecular ion (H_2^+) were solved accurately in an analytical expansion form by the FC method combined with the variational principle. H_2^+ is the simplest homonuclear molecule and has been extensively studied so far, especially in the early-stage of the molecular quantum chemistry; indeed, H_2^+ was important for the development of the LCAO-MO method. Not only from

theoretical viewpoint but also from experimental viewpoint, it withdraws a lot of interests since it is recognized as an important interstellar molecule. Quite accurate description of this molecule is necessary for the assignment of astronomical spectroscopy.[30] The purpose of this chapter is to examine if the FC method gives an accurate wave function of H_2^+ in both non-relativistic and relativistic cases. Examinations were carried out both for ground and excited states. The error analysis indicates that the present result is highly accurate.

The conclusions in chapter 4 clearly show that the FC method gives highly accurate wave function for both the non-relativistic SE and the relativistic DE. However, the FC method combined with the variational principle contains serious difficulty for its application to many-electron systems; for instance, evaluation of overlap and Hamiltonian integrals becomes almost impossible because of their high dimensionalities. In chapter 5, the author proposed the new methodology to overcome the difficulty in evaluation of the integrals. By employing the new approach called the local Schrödinger equation (LSE) method, integrations all over the coordinate spaces become unnecessary. The LSE method is based on the locality of the SE, that is, for the exact wave function ψ, the local energy $E_L(\mathbf{x}) = H\psi(\mathbf{x})/\psi(\mathbf{x})$ is constant at every point in the coordinate space. Since the FC method provides quite accurate wave function for the SE, the local energy is almost constant in the coordinate space. Note that the constancy of the local energy is not kept in the conventional *ab initio* method because the wave function is not accurate enough. The purpose of this chapter is the formulation and the development of the LSE method in order to apply the FC method to many-electron system. The author applied the LSE method to such two to five electron systems as He, Li, Be, B, H_2 and LiH. The calculated electronic energies were compared with the highly accurate computational results reported previously and confirmed that the LSE method can present quite accurate wave functions likewise the FC method combined with the variational principle.

From the early stage of quantum chemistry, presenting the chemically important insight

is one of the important purposes of the theoretical and computational chemistry. In Part I of this thesis, theoretical and computational study is performed with the aim of presenting chemical insights by the *ab initio* electronic structure method. The synthetically important reactions by transition metal complexes are investigated here and the computational results are discussed to present well understanding of those reactions.

Although valuable chemical insights could be proposed by the *ab initio* electronic structure theory, there still remain uncertainties in computational results because total energy, geometry, electronic distribution and so on depend on computational method and basis functions. We must always pay attention to the dependencies and uncertainties. This means that exact computational results are hardly provided; this is one of the biggest problems in the field of computational chemistry. We can become free from such problems when the general methodology is established to provide the exact solution of the SE/DE. Therefore, developing the new, general, and accurate electronic structure method is the fundamental target for the theoretical physical chemists.

In part II, the new *ab initio* method called the FC method was developed and applied to molecular systems at both non-relativistic and relativistic levels. The integration difficulty has been overcome by employing the LSE method. Therefore, in principle, its application to the general system becomes possible by the present work. Unfortunately, the straightforward application of the FC method to chemically important systems is still difficult from the viewpoint of computational cost. The author, however, believes that the knowledge and insight provided by this thesis are helpful to establish the highly reliable quantum chemical computational method for the transition metal chemistry.

References

(1) *The Organometallic Chemistry of the Transition Metals*; Crabtree, R. H., Ed.; John Wiley & Sons: New York, 1988.

(2) Cotton, F. A.; Wilkinson, G. *Advanced Inorganic Chemistry*; John Wiley: New York, 1988.

(3) Sakaki, S.; Maruta, K.; Ohkubo, K. *Inorg. Chem.* **1987**, *26*, 2499.

(4) Sakaki, S.; Ujino, Y.; Sugimoto, M. *Bull. Chem. Soc. Jpn.* **1996**, *69*, 3047.

(5) Sakaki, S.; Biswas, B.; Sugimoto, M. *Journal of the Chemical Society-Dalton Transactions* **1997**, 803.

(6) Biswas, B.; Sugimoto, M.; Sakaki, S. *Organometallics* **2000**, *19*, 3895.

(7) Ochi, N.; Nakao, Y.; Sato, H.; Sakaki, S. *J. Am. Chem. Soc.* **2007**, *129*, 8615.

(8) Ohnishi, Y. Y.; Nakao, Y.; Sato, H.; Sakaki, S. *J. Phys. Chem. A* **2008**, *112*, 1946.

(9) Dirac, P. A. M. *Proc. R. soc. Lond. Ser. A-Contain. Pap. Math. Phys. Character* **1929**, *123*, 714.

(10) Nakatsuji, H. *J. Chem. Phys.* **2000**, *113*, 2949.

(11) Nakatsuji, H.; Davidson, E. R. *J. Chem. Phys.* **2001**, *115*, 2000.

(12) Nakatsuji, H. *Phys. Rev. A* **2002**, *65*, 15.

(13) Nakatsuji, H. *Phys. Rev. Lett.* **2004**, *93*, 4.

(14) Nakatsuji, H. *Phys. Rev. A* **2005**, *72*, 12.

(15) Kurokawa, Y.; Nakashima, H.; Nakatsuji, H. *Phys. Rev. A* **2005**, *72*, 11.

(16) Nakashima, H.; Nakatsuji, H. *J. Chem. Phys.* **2007**, *127*, 14.

(17) Nakatsuji, H.; Ehara, M. *J. Chem. Phys.* **2002**, *117*, 9.

(18) Kutzelnigg, W. *Chem. Phys.* **1997**, *225*, 203.

(19) Hill, R. N.; Krauthauser, C. *Phys. Rev. Lett.* **1994**, *72*, 2151.

(20) *Atomic, Molecular & Optical Physics Handbook*; Grant, I. P., Ed.; AIP: New York,

1996.

(21) Grant, I. P.; Quiney, H. M. *Phys. Rev. A* **2000**, *62*, 14.

(22) Nakatsuji, H.; Nakashima, H. *Phys. Rev. Lett.* **2005**, *95*, 4.

(23) Crabtree, R. H. *Chem. Rev.* **1985**, *85*, 245.

(24) Suzuki, A. *Pure Appl. Chem.* **1994**, *66*, 213.

(25) *Metal Catalyzed Cross-Coupling Reactions*; Diederich, F., Ed.; John Wiley & Sons: New York, 2004.

(26) Kowan, J. A. *Inorganic Biochemistry*; Wiley-VCH: New York, 1997.

(27) Lipperd, S. J.; Berg, J. M. *Principles of Bioinorganic Chemistry*; University Science Books: Mill Vallay, 1994.

(28) *Metalloporphyrins in Catalytic Oxidations*; Sheldon, R. A., Ed.; Marcel Dekker: New York, 1994.

(29) *Oxygenases and Model Systems*; Watanabe, Y.; Funabiki, T., Eds.; Kluwer Academic Publishers: Netherlands, 1997.

(30) Khersonskij, V. K. *Astrophys. Space Sci.* **1984**, *98*, 255.

(31) Frisch, M. J.; Trucks, G. W.; Schlegel, H. B.; Scuseria, G. E.; Robb, M. A.; Cheeseman, J. R.; J. A. Montgomery, J.; Vreven, T.; Kudin, K. N.; Burant, J. C.; Millam, J. M.; Iyengar, S. S.; Tomasi, J.; Barone, V.; Mennucci, B.; Cossi, M.; Scalmani, G.; Rega, N.; Petersson, G. A.; Nakatsuji, H.; Hada, M.; Ehara, M.; Toyota, K.; Fukuda, R.; Hasegawa, J.; Ishida, M.; Nakajima, T.; Honda, Y.; Kitao, O.; Nakai, H.; Klene, M.; Li, X.; Knox, J. E.; Hratchian, H. P.; Cross, J. B.; Bakken, V.; Adamo, C.; Jaramillo, J.; Gomperts, R.; Stratmann, R. E.; Yazyev, O.; Austin, A. J.; Cammi, R.; Pomelli, C.; Ochterski, J. W.; Ayala, P. Y.; Morokuma, K.; G. A. Voth, P. S., J. J. Dannenberg,; Zakrzewski, V. G.; Dapprich, S.; Daniels, A. D.; Strain, M. C.; Farkas, O.; Malick, D. K.; Rabuck, A. D.; Raghavachari, K.; Foresman, J. B.; Ortiz, J. V.; Cui, Q.; Baboul, A. G.; Clifford, S.; Cioslowski, J.; Stefanov, B. B.; Liu, G.; Liashenko, A.; Piskorz, P.; Komaromi, I.; Martin, R. L.; Fox, D. J.; Keith, T.; Al-Laham, M. A.; Peng, C. Y.;

Nanayakkara, A.; Challacombe, M.; Gill, P. M. W.; Johnson, B.; Chen, W.; Wong, M. W.; Gonzalez, C.; Pople, J. A. *Gaussian 03, Revision D.02*; Gaussian Inc.: Wallingford, CT, 2004.

Part I

Theoretical Studies of the Reaction

Involving Transition Metal Complex

Chapter 1

Oxygen Atom Transfer Reactions of Iridium and Osmium Complexes: Theoretical Study of Characteristic Features and Significantly Large Differences Between These Two Complexes

Abstract

Oxygen atom transfer reaction between ML_3=O and ML_3 (L=2,4,6-trimethylphenyl (Mes) for M=Ir and L= 2,6-diisopropylphenylimide (NAr) for M=Os) was theoretically investigated by DFT method. The optimized geometry of $(Mes)_3$Ir-O-Ir$(Mes)_3$ agrees well with the experimental one, though those of $(CH_3)_3$Ir-O-Ir$(CH_3)_3$ and Ph_3-Ir-O-IrPh_3 are much different from the experimental one. These results indicate that the bulky ligand plays important roles to determine geometry of the μ-oxo dinuclear Ir complex. Theoretical study of the real systems presents clear pictures of these oxygen atom transfer reactions, as follows: In the Ir reaction system, (i) the μ-oxo bridged dinuclear complex is more stable than the infinite separation system in potential energy surface, indicating this is incomplete oxygen atom transfer reaction which does not occur at very low temperature, (ii) unsymmetrical transition state is newly found, in which one Ir-O distance is longer than the other one, (iii) unsymmetrical local minimum is also newly found between the transition state and the infinite separation system, and (iv) activation barrier (E_a) is very small. In the Os reaction system, (v) the transition state is symmetrical, while no intermediate is observed unlike the Ir reaction system, and (vi) E_a is very large. These results are consistent with the experimental results that the reaction rapidly occurs in the Ir system but very slowly in the Os system, and that the μ-oxo bridged dinuclear intermediate is detected in the Ir system but not in the Os system. To elucidate the reasons of these differences between Ir and Os systems, the E_a value is decomposed into the nuclear and electronic factors. The former is the energy necessary to distort ML_3 and ML_3=O moieties from their equilibrium geometries to those in the transition state. The latter depends on donor-acceptor interaction between ML_3=O and ML_3. The nuclear factor is much larger in the Os system than in the Ir system and it contributes to about 70% of the difference in E_a. The energy gap between the donor orbital of ML_3 and the acceptor orbital of ML_3=O is much larger in the Os system than in the Ir system, which also contribute to the lower E_a value of the Ir system than that of the Os system.

1.1 Introduction

Oxygen atom transfer reactions mediated by transition metal complexes (eq.1) are of considerable interest in synthetic and biomimetic chemistries.[1-3]

$$M{-}O + R \rightarrow M + O{-}R \qquad (1)$$

Because oxygen atom is removed from metal center and added to substrate as shown in eq. 1, this reaction deeply relates to catalytic oxygenation processes such as olefin epoxidation[4-6] and hydroxylation.[7-10] This process is also important in biological systems; actually a number of important metalloenzymes mediate atom transfer reaction as key step.[11, 12] One of the typical examples is cytochrome P-450 class of enzymes.[13-16] Also, oxygen atom transfer reactions between non-heme iron-oxo and iron complexes are reported.[17-20] Another important example is activation of dioxygen molecule,[4-6] in which the O-O bond cleavage occurs and one of the two oxygen atoms is utilized for oxidation reaction via oxygen-atom transfer reaction.

To utilize effectively the oxygen atom transfer reaction in catalytic, biomimetic, and biological chemistries, correct knowledge of this reaction such as transition state geometry, its electronic structure, and determining factor of reactivity is indispensable. In this regard, several experimental and theoretical studies have been carried out to present such knowledge and clarify the determining factors so far.[17-24]

Recently, the oxygen atom transfer reactions between late transition metal complexes and their oxo-complexes (Scheme 1 (A) to (D)) were investigated experimentally and theoretically by Fortner *et. al.* and several interesting results were reported,[25] as follows; the oxygen atom transfer between trimesityliridium(III) complex **Ir(Mes)$_3$** (Mes = 2,4,6-trimethylphenyl) and its oxo-complex **Ir(Mes)$_3$=O** very rapidly occurs, while that between similar tris(2,6-diisopropylphenyl)imide osmium(V) complex **Os(NAr)$_3$** (Ar = 2,6-diisopropylphenyl) and its oxo-complex **Os(NAr)$_3$=O** very slowly occurs; the rate constant is 5×10^{7} M^{-1} s^{-1} at 20 °C for the former reaction but 1.8×10^{-5} M^{-1} s^{-1} for the latter

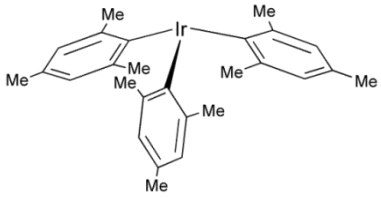

(A) Trimesityliridium (**Ir(Mes)$_3$**)

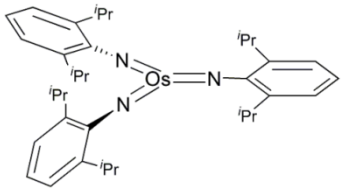

(B) Oxotrimesityliridium (**Ir(Mes)$_3$=O**)

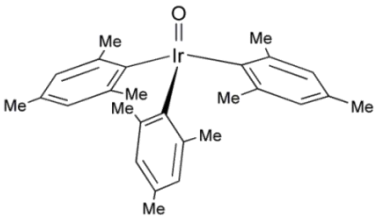

(C) Tris(2,6-diisopropylphenylimide)osmium (**Os(NAr)$_3$**)

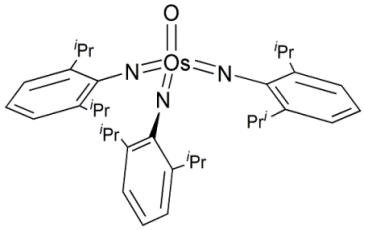

(D)Oxo-tris(2,6-diisopropylphenylimide)osmium (**Os(NAr)$_3$=O**)

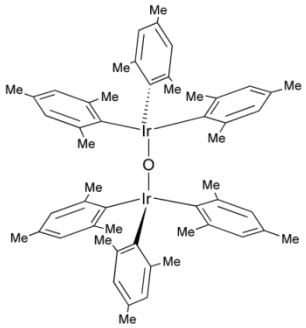

(E) μ-oxohexamesityldiiririum (**IM$_{IrMes}$**) :(Mes)$_3$Ir-O-Ir(Mes)$_3$

Scheme 1. Molecular structures of Iridium and Osmium complexes.

reaction. This significantly large difference cannot be understood from thermodynamic point of view, since the Ir=O bond energy is little different from the Os=O bond energy by only 0.86 kcal/mol.[26] Also, another interesting result was reported about the reaction behavior, as follows; Because the oxygen atom is transferred from one metal complex to the other one, it is likely that the transition state takes μ-oxo bridged dinuclear geometry. Interestingly, such μ-oxo bridged dinuclear complex **(Mes)$_3$Ir-O-Ir(Mes)$_3$** (**IM$_{IrMes}$**; see Scheme 1) was isolated in the reaction of the iridium system and analyzed by the X-ray crystallography.[25] The linear μ-oxo bridged dinuclear complex was also spectroscopically observed in the reaction of the iridium system below -80 °C.[25] Because of the formation of the μ-oxo bridged dinuclear

complex, this reaction is experimentally understood to be “incomplete” oxygen atom transfer reaction.[1] This incomplete oxygen atom transfer reaction changes to a “complete” oxygen atom transfer reaction at higher temperature. On the other hand, such μ-oxo dinuclear intermediate has been neither isolated nor detected in the osmium reaction system. It is of considerable interest to characterize reaction features of these iridium and osmium complexes including the transition state and the intermediate, and to elucidate the reasons why the oxygen atom transfer reaction rapidly occurs in the iridium system but very slowly in the osmium system[25] despite of their similar geometries and M=O bond energies.[26] Forter *et.al.* also theoretically investigated these reactions and presented fundamental explanation on differences in reorganization energy and frontier orbitals based on DFT computational results of model systems.

In this paper, we wish to report theoretical study of above-described oxygen atom transfer reaction between **Ir(Mes)$_3$** and **Ir(Mes)$_3$=O** and that between **Os(NAr)$_3$** and **Os(NAr)$_3$=O**. Our purposes here are to elucidate the reaction features, to make clear comparison between the reactions of iridium and osmium complexes, and to provide the clear understanding for the reasons of the significantly large differences between these two reaction systems. We wish to emphasize that unsymmetrical transition state and intermediate are newly found in the iridium reaction system. We believe that these theoretical results are valuable for designing efficient atom transfer reaction and making further development of this type of reaction.

1.2 Computational Methods

All these **Ir(Mes)$_3$**, **Ir(Mes)$_3$=O**, **Os(NAr)$_3$**, and **Os(NAr)$_3$=O** are experimentally reported to be neutral.[37,39] For all compounds, the singlet state was calculated to be the most stable; see Table A2 in Appendix.

We employed real complexes and their small models in calculations. In model

complexes, the mesityl groups of the iridium complexes and the 2, 6-diisopropylphenyl groups of the osmium complexes were replaced by methyl groups. These trimethyl iridium and osmium complexes and their oxo complexes are represented by **$Ir(CH_3)_3$**, **$Os(NCH_3)_3$**, **$Ir(CH_3)_3=O$** and **$Os(NCH_3)_3=O$**, respectively. All these model complexes are neutral and their ground states are singlet, too.

In both model and real systems, we optimized geometries and evaluated energy changes with the density functional theory (DFT) using B3LYP functional.[27, 28] In model systems, two basis set systems (BS-I and BS-II) were employed for calculation. In BS-I, Stuttgart-Dresden-Bonn effective core potentials (ECPs) were used to replace core electrons of iridium and osmium atoms, and (311111/22111/411) basis sets were used for their valence electrons.[29] Usual 6-31G (d) basis sets[30] were used for carbon, oxygen, nitrogen, and hydrogen atoms. In BS-II, Dunning cc-pVDZ basis sets[31] were used for carbon, nitrogen, oxygen, and hydrogen atoms, while the same basis sets and ECPs as those of BS-I were employed for the metal atoms. BS-I was used for geometry optimization and calculation of vibrational frequency and BS-II was used for evaluation of energy changes.

In the real systems, moderately smaller basis set systems (BS-III and BS-IV) were employed: In BS-III, Los Alamos ECPs and (341/321/21) basis sets were used for core and valence electrons of metal atoms,[32] respectively. Usual 6-31G(d) basis sets were used for oxygen and nitrogen atoms of imide group, and 6-31G for carbon and hydrogen atoms of phenyl ring. STO-3G basis sets were used for methyl group of mesityl ligand and isopropyl group of imide ligand. The BS-III was used for geometry optimization and evaluation of vibrational frequency. BS-IV was almost the same as BS-I, while d polarization function was deleted from carbon atom of methyl and isopropyl groups to save CPU time. Zero-point energy was evaluated with the DFT/BS-III method under assumption of harmonic oscillator.

Solvation effects of dichloromethane and benzene were evaluated with PCM method,[33] where the geometries were re-optimized in solution with the PCM method at the DFT/BS-III

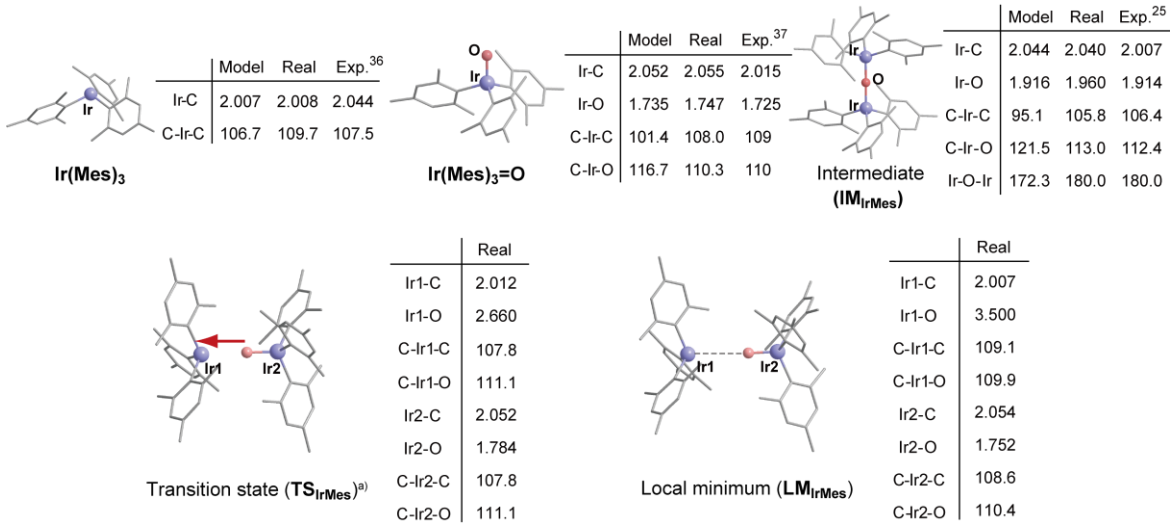

Figure 1. Selected bond lengths (in Å) and angles (in degree) of the iridium reaction system where hydrogen atoms are omitted. a) The displacement vector corresponding to imaginary frequency is shown by arrow.

level. All the computations were performed by Gaussian 03 program package.[34]

In this oxygen atom transfer reaction, the transition state and intermediate are formed as adduct of ML_3 and ML_3=O (M=Ir or Os; L=Mes or NAr). Because the entropy of reactants considerably decreases in this process, we must present discussion based on the Gibbs free energy change, ΔG^0. Though the ΔG^0 value is evaluated in gas phase by Gaussian 03 program, the ΔG^0 value in solution is much different from that in gas phase, because translation movement is considerably suppressed in solution and hence the translation entropy is much smaller than that in gas phase. Here, we evaluated the translational entropy in solution by considering free space available for the translation movement, according to the method proposed by Whitesides *et.al.*[35] The molecular volume of solvent is estimated by DFT/BS-I-calculated electronic density; see Appendix page A4 for the details.

1.3 Results

1.3.1 Preliminary Investigation with Model Systems, $Ir(CH_3)_3$, $Ir(CH_3)_3$=O, $Os(NCH_3)_3$, and $Os(NCH_3)_3$=O

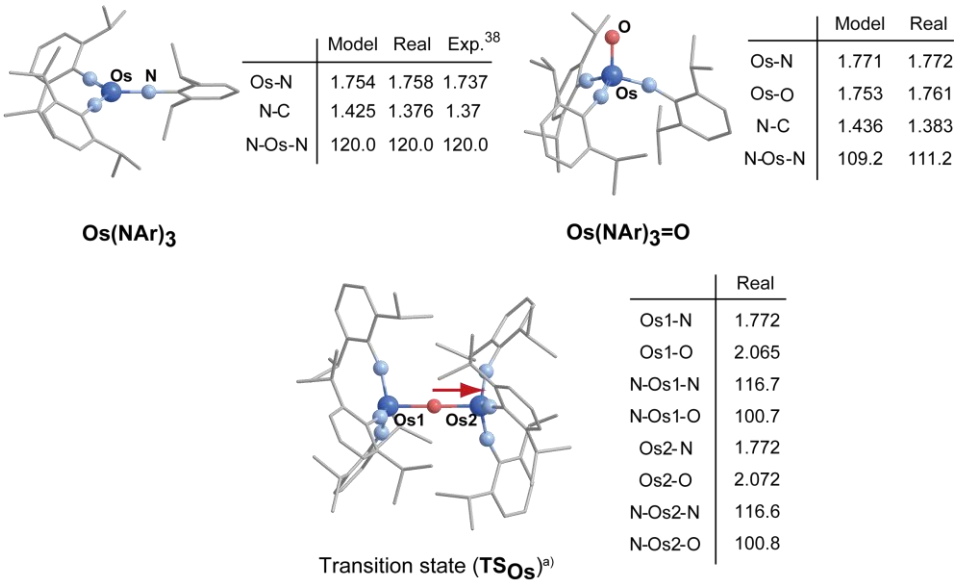

Figure 2. Selected bond lengths (in Å) and angles (in degree) of the osmium reaction system where hydrogen atoms are omitted. a) The displacement vector corresponding to imaginary frequency is shown by arrow.

Both **Ir(CH$_3$)$_3$** and **Ir(CH$_3$)$_3$=O** have tetrahedral-like structures with C_{3v} symmetry, which agree well with their experimental structures of the real complexes, as shown in .[36, 37] On the other hand, **Os(NCH$_3$)$_3$** has trigonal planar structure with D_{3h} symmetry unlike **Ir(CH$_3$)$_3$**, while **Os(NCH$_3$)$_3$=O** has tetrahedral-like structure with C_{3v} symmetry like **Ir(CH$_3$)$_3$=O**. These geometries also agree well with the experimental structures of the real complexes except for the Os-N-Me angle (Figure 2);[38] the optimized Os-N-Me angle is 157°, whereas it is linear in the experimental structure. The bending geometry was reported in previous computational study of similar small model.[39] In further smaller model, Os(NH)$_3$, the optimized Os-N-H angle (134°) becomes much smaller. From these results, it is concluded that the Os-N-R bending geometry is favorable from the viewpoint of electronic structure but bulky substituent leads to the formation of the linear geometry. In the latter half of this work, we employed real substituent.

In the iridium system, we optimized the μ-oxo bridged dinuclear complex, (CH$_3$)$_3$-Ir-O-Ir-(CH$_3$)$_3$, **IM$_{IrMe}$**. The optimized geometry of **IM$_{IrMe}$** agrees well with the experimental geometry except for too small C-Ir-O and C-Ir-C angles, as shown in Figure 1.

These small angles are easily interpreted in terms of much smaller methyl group than mesityl group. This result again indicates that the electronic factor favors this bending geometry and the bulky substituent is necessary for the linear geometry. **IM_{IrMe}** is calculated to be more stable than the infinite separation system by 18.2 kcal/mol with the DFT/BS-II method. This computational result of the iridium model system suggests that the oxygen atom transfer reaction of the iridium system is "incomplete".

In the osmium system, the transition state could not be optimized. Instead of the transition state, the μ-oxo dinuclear complex $(CH_3N)_3Os\text{-}O\text{-}Os(NCH_3)_3$ was optimized unexpectedly, in which the Os-O-Os moiety is bent like **IM_{IrMe}**. This geometry possesses no imaginary frequency. We optimized the linear μ-oxo dinuclear osmium complex under constraint of the linear Os-O-Os moiety. However, it exhibits imaginary frequency of about 49.8i cm^{-1}, which mainly involves the Os-O-Os bending motion. Moreover, the linear structure is much less stable than the bent structure by 44.4 kcal/mol. These results lead to conclusions that this linear μ-oxo dinuclear osmium complex is not the proper transition state for the oxygen atom transfer reaction, and that the transition state cannot be successfully optimized with the model system.

It is likely that the above problems observed in both iridium and osmium model systems arise from the oversimplification of the ligand. The importance of the bulky ligand for the oxygen atom transfer reaction was also experimentally suggested.[40] Thus, the real system should be employed for theoretical study to present the correct understanding of the oxygen atom transfer reaction.

1.3.2 Geometries of Reactant, Intermediate, and Transition States of Real Systems

Optimized geometries of **$Ir(Mes)_3$**, **$Ir(Mes)_3{=}O$**, and intermediate **IM_{IrMes}** agree well with their experimental ones,[25, 36, 37] as shown in Figure 1. **IM_{IrMes}** possesses no imaginary

Table 1. Relative values of calculated thermodynamic parameters (kcal/mol) for Ir and Os real systems in gas phase.

		Ir system				Os system	
	Temperature / K	**IM_{IrMes}**	**TS_{IrMes}**	**LM_{IrMes}**	**$Ir(Mes)_3$ + $Ir(Mes)_3$=O**	**TS_{Os}**	**$Os(NAr)_3$ + $Os(NAr)_3$=O**
Electronic Energy (E_0)	-	-4.2	-2.1	-3.2	0.0	33.6	0.0
E_0 + Zero Point Energy	-	-3.9	-1.9	-4.1	0.0	33.3	0.0
E_0 + Zero Point Energy + Thermal Energy	50	-4.0	-2.0	-3.8	0.0	33.2	0.0
	100	-3.9	-1.9	-3.6	0.0	33.2	0.0
	298.15	-2.9	-1.2	-2.8	0.0	34.5	0.0
Thermal Enthalpy	50	-4.1	-2.1	-3.9	0.0	33.2	0.0
	100	-4.1	-2.1	-3.8	0.0	33.0	0.0
	298.15	-3.5	-1.8	-3.4	0.0	33.9	0.0
Gibbs Free Energy	50	-1.2	0.7	-2.3	0.0	33.3	0.0
	100	1.5	3.2	-0.3	0.0	39.8	0.0
	298.15	12.4	13.6	8.0	0.0	52.6	0.0

frequency, indicating that this is equilibrium structure. It is noted that the Ir-O-Ir moiety is linear in **IM_{IrMes}** unlike that of **IM_{IrMe}**. We carried out geometry optimization of other model systems, **$Ir(Ph)_3$** and **$Ir(Ph)_3$=O**, in which mesityl groups were substituted for phenyl groups. In this model, the μ-oxo bridged Ir-O-Ir moiety is bending unlike the real system, although the potential energy surface is flat; see supporting information Figures A1 and A2. Thus, it should be concluded that the mesityl groups play important roles to determine the geometry of the intermediate; in other words, the geometry of the μ-oxo bridged dinuclear iridium intermediate is determined by delicate balance between electronic and steric factors. The transition state (**TS_{IrMes}**) was newly optimized in this work. It has unsymmetrical μ-oxo bridged dinuclear geometry in which one Ir-O distance is 1.784 Å and the other one is 2.660 Å, as shown in Figure 1. This transition state exhibits only one imaginary frequency, in which the oxygen atom is moving from one iridium center toward the other center. Besides this transition state and the symmetrical μ-oxo bridged dinuclear intermediate, we found the unsymmetrical local energy minimum (**LM_{IrMes}**) in which one Ir-O distance is 1.752 Å and

the other one is 3.500 Å, as shown in Figure 1.

In the osmium real system, the optimized geometry of **Os(NAr)$_3$** also agrees well with its experimental structure,[25] as shown in Figure 2. Optimized transition state (**TS$_{Os}$**) is symmetrical. It possesses one imaginary frequency, in which the oxygen atom is moving from one osmium center toward the other osmium center, too.

It is noted that the serious disagreements between the optimized geometries of small models and the experimental ones disappear in the optimized geometries of real systems; for instance, the Os-N-C moiety is bending in **Os(NCH$_3$)$_3$** but becomes almost linear in **Os(NAr)$_3$**, and the Ir-O-Ir moiety is bending **IM$_{IrMe}$** but becomes almost linear in **IM$_{IrMes}$**.

1.3.3 Potential Energy Curves (PECs) of the Oxygen Atom Transfer Reaction

The PEC of the real system is evaluated against one M-O distance, where the other moiety was optimized without any constraint. Potential and Gibbs free energies were calculated for important molecular structures such as intermediate and transition state are shown in Table 1. It is noted that the μ-oxo dinuclear intermediate (**IM$_{IrMes}$**) is more stable than both the local minimum (**LM$_{IrMes}$**) and the infinite separation system. The activation barrier of this reaction is quite small (3.9 kcal/mol).[41] Thus, the presence of the stable **IM$_{IrMes}$** indicates that the oxygen atom transfer reaction does not occur at low temperature.

Entropy effect should be considered to discuss the reaction. In gas phase, the Gibbs free energy change (ΔG^0) of **IM$_{IrMes}$** is much larger (12.4 kcal/mol) than that of the infinite separation system at 298.15 K, but it decreases to 1.5 kcal/mol at 100 K and -1.2 kcal/mol at 50 K. The $\Delta G^{0\ddagger}$ value is 0.7 kcal/mol at 50 K and 13.6 kcal/mol at 298.15 K.[41]

In solvent, we need to correct ΔG^0 value because translation movement is considerably suppressed in solution and the translation entropy is much smaller than that in gas phase. We employed here the method proposed by Whitesides *et.al.*[35] to evaluate entropy in solution.

Table 2. Relative values of calculated thermodynamic parameters (kcal/mol) for Ir and Os real systems in solution [a], where the translational entropy was corrected by Whitesides' method [35]

		Ir system (in dichloromethane)				Os system (in benzene)	
	Temperature / K	**IM_{IrMes}**	**TS_{IrMes}**	**LM_{IrMes}**	**$Ir(Mes)_3$ + $Ir(Mes)_3$=O**	**TS_{Os}**	**$Os(NAr)_3$ + $Os(NAr)_3$=O**
Electronic Energy (E_0)	-	-3.9	0.5	-0.2	0.0	31.2	0.0
E_0 + Zero Point Energy	-	-3.0	1.0	-0.7	0.0	30.3	0.0
E_0 + Zero Point Energy + Thermal Energy	50	-3.1	1.0	-0.6	0.0	30.3	0.0
	100	-3.0	1.1	-0.3	0.0	30.3	0.0
	298.15	-2.1	1.7	0.5	0.0	31.3	0.0
Thermal Enthalpy	50	-3.2	0.9	-0.7	0.0	30.1	0.0
	100	-3.2	0.9	-0.5	0.0	30.1	0.0
	298.15	-2.7	1.1	-0.1	0.0	30.7	0.0
Gibbs Free Energy	50	-0.5	3.4	1.4	0.0	33.2	0.0
	100	2.2	5.9	3.4	0.0	36.3	0.0
	298.15	12.6	15.9	10.9	0.0	48.3	0.0
Corrected Gibbs Free Energy	50	-1.0	2.9	0.9	0.0	32.6	0.0
	100	1.4	5.2	2.7	0.0	35.0	0.0
	298.15	8.8	12.1	7.1	0.0	43.8	0.0

a) Geometry optimization and energy evaluation were carried out by the PCM method at B3LYP/BS-III and BS3LYP/BS-IV levels, respectively.

Evaluated ΔG^0 value of **IM_{IrMes}** is -1.0 kcal/mol at 50 K, 1.4 kcal/mol at 100 K, and 8.8 kcal/mol at 298.15 K. The $\Delta G^{0‡}$ value is 2.9 kcal/mol at 50 K, 5.2 kcal/mol at 100 K, and 12.1 kcal/mol at 298.15 K, as shown in Table 2. These computational results are consistent with the experimental fact that **IM_{IrMes}** is isolated at 100 K but the oxygen atom transfer reaction occurs at higher temperature.

On the other hand, no intermediate is observed in the osmium system, in which only transition state (**TS_{Os}**) was optimized, as shown in Figure 2. It is noted that the activation barrier is very large. The $\Delta G^{0‡}$ value was evaluated to be 35.0 kcal/mol at 100 K and 43.8 kcal/mol at 298.15 K as shown in Table 2. These computational results reproduce well that the reaction behavior is completely different between iridium and osmium reaction systems.

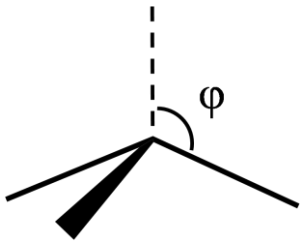

Scheme 2. Definition of the pendant angle

1.4 Discussions

Apparently, the oxygen atom transfer reaction occurs with very small activation barrier (E_a) in the iridium reaction system but with very large E_a value in the osmium reaction system, as shown in Tables 1 and 2. These results are consistent with the experimental results that the reaction rapidly occurs in the iridium system but very slowly in the osmium system.

It is worth elucidating the reasons why the significantly large difference is observed between the iridium and osmium systems in spite of their similar geometries and similar M=O bond energies.[25, 26] Here, we make analyses by decomposing the E_a value into nuclear and electronic parts, like the discussion presented by Fortner and his coworkers.[25] To exchange an oxygen atom, ML_3 and ML_3=O complexes have to change their geometries into those of TS. The destabilization energy induced by the geometry change corresponds to the re-organization energy in atom transfer event, which is considered as the nuclear factor. The electronic factor basically relates to the interaction between electron donor orbital of ML_3 and electron acceptor orbital of ML_3=O. Decrease of the re-organization energy and increase of the interaction lead to decrease of the activation barrier of the reaction.

1.4.1 Nuclear Factor

In various geometry changes, the largest change is observed at the pendent angle, definition of which is given in Scheme 2. This means that the pendant angle can be taken as

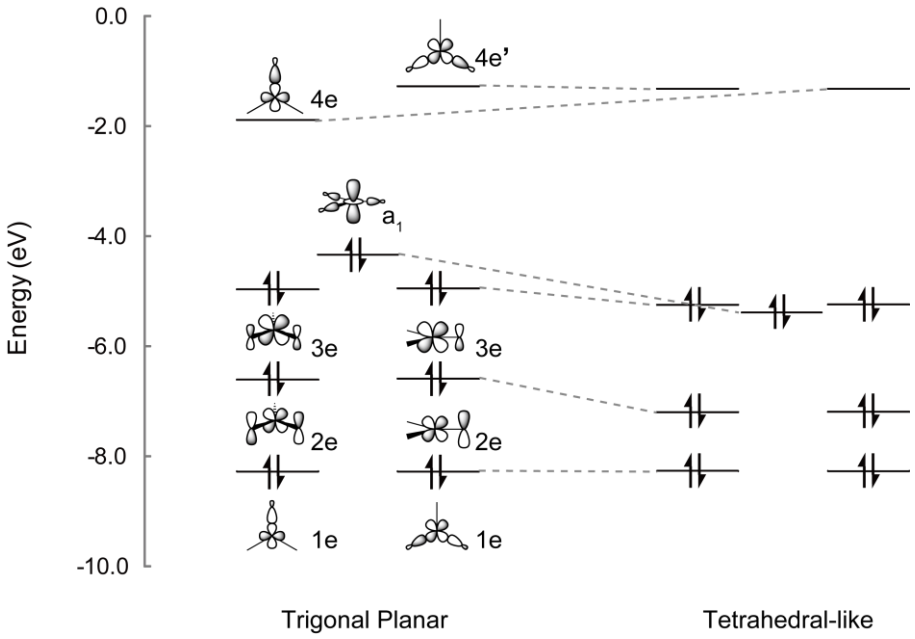

Selected molecular orbitals of $Ir(Mes)_3$ at tetrahedral and trigonal planar geometries[a)]

a) The 4e and 4e' orbitals are degenerate in model complex (**$Ir(CH_3)_3$**). Splitting of these orbitals in **$Ir(Mes)_3$** is induced the symmetry deviation of mesityl ligand.

Scheme 3

reaction coordinate. We evaluated the re-organization energy as the energy difference of the reactant between the fully optimized geometry and the partially optimized one in which only the pendant angle was fixed to be the same as that of the transition state.

The re-organization energy of the osmium system is much larger than that of the iridium system, as shown in Table 3; in particular, the re-organization energy of **$Os(NAr)_3$** is very large. This difference is easily interpreted in terms of the geometries of the reactant, transition state, and product. In the iridium system, **$Ir(Mes)_3$**, **$Ir(Mes)_3$=O**, and **TS_{IrMes}** all

Table 3. Pendant angles (θ)[a)] of ML_n, ML_n=O, and transition-state (M=Ir or Os; L=2,4,6-trimethylphenyl for Ir and tris(2,6-diisopropylphenyl)imide for Os) and re-organization energies ($E_{re\text{-}org}$) (in kcal/mol)

	θ			$E_{re\text{-}org}$	
	ML_n	ML_n=O	TS	ML_n	ML_n=O
Ir	109.2	110.3	113.0	1.32	0.86
Os	90.9	108.0	100.8	10.2	3.42

a) See Scheme 2 for the pendant angle.

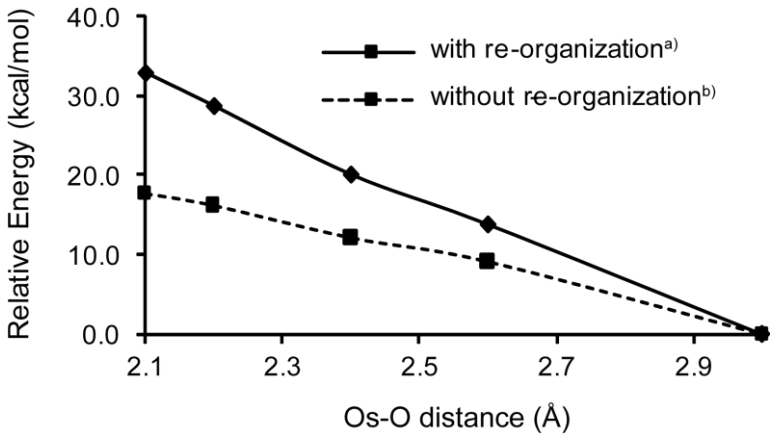

Figure 3. Potential energy curves against the Os-O distance in the Os system with and without re-organization energy. a) The geometry was fully optimized except for the reaction coordinate, the Os-O distance. b) Geometries of **Os(NAr)$_3$** and **Os(NAr)$_3$=O** were taken to be the same as those in the transition state.

have tetrahedral-like structures around the Ir center, as shown in Figure 1, in which the pendant angle is similar to each other. As a result, the geometry change does not necessarily occur so much upon going from **Ir(Mes)$_3$** and **Ir(Mes)$_3$=O** to **TS$_{IrMes}$**, leading to the small re-organization energy. In the osmium system, on the other hand, **Os(NAr)$_3$** is trigonal planar, as shown in Figure 2, but **TS$_{Os}$** and **Os(NAr)$_3$=O** have tetrahedral-like structure around the Os center. Thus, the structure of **Os(NAr)$_3$** considerably changes upon going to **TS$_{Os}$** from **Os(NAr)$_3$**. This is the reason why the re-organization energy of **Os(NAr)$_3$** is considerably large.

To investigate how much the nuclear factor contributes to the activation barrier, the PEC without the re-organization energy was calculated in the osmium system, as shown in Figure 3, where one of the Os-O distances was taken as the reaction coordinate and the pendent angle was fixed to that of **TS$_{Os}$**. This PEC still represents the activation barrier of about 10 kcal/mol, which is about 30 % of the total activation barrier. Hence, it is concluded that the nuclear factor contributes to 70 % of the activation barrier of the osmium reaction system and the electronic factor still contributes to 30 % of the activation barrier.

1.4.2 The Reasons Why the Geometry of $Os(NAr)_3$ is Trigonal-planar but That of $Ir(Mes)_3$ is Tetrahedral-like

Because the large re-organization energy of **$Os(NAr)_3$** arises from its trigonal planar geometry and the small re-organization energy of **$Ir(Mes)_3$** arises from its tetrahedral-like geometry, as discussed above, it is worth investigating the reason why the geometry of **$Ir(Mes)_3$** is tetrahedral-like but that of **$Os(NAr)_3$** is trigonal planar. The frontier orbital energies of **$Ir(Mes)_3$** and **$Os(NAr)_3$** are shown in Schemes 3 and 4, respectively. Metal d orbitals play important role to construct these frontier orbitals, as follows: the HOMO (a_1) of **$Ir(Mes)_3$** mainly consists of the Ir d_z^2 orbital. Because of the presence of the π orbitals of the mesityl ligand, π-type bonding and anti-bonding molecular orbitals (MOs) are formed in the HOMO-2 (2e) and the HOMO-1 (3e), respectively; indeed, the HOMO-1 largely consists of Ir d_π orbital into which the π orbital of the mesityl ligand mixes in an anti-bonding way. The HOMO-2 (2e) largely consists of the occupied π orbitals of the mesityl group into which the Ir d_π orbital mixes in a bonding way. Because the Ir(III) center has six d electrons, these d_π-p_π bonding and anti-bonding orbitals are doubly occupied. The bonding orbital (HOMO-2) is stabilized by the geometry change to the tetrahedral-like structure from the planar one, because the overlap between the Ir d_π and the mesityl π orbitals increases by this geometry change, as shown in Scheme 3. Usually, the d_π-p_π anti-bonding orbital energy rises when the d_π-p_π bonding orbital energy becomes lower. However, the HOMO-1 energy becomes moderately lower by this geometry change, unexpectedly. This energy stabilization can be understood in terms of the mixing of the π^* orbital of the mesityl into the d_π-π anti-bonding orbital; for detailed discussion see Appendix A3. The HOMO energy also decreases by this geometry change (Scheme 3). The reason is interpreted as follows: The HOMO involves anti-bonding interaction between the Ir d_z^2 orbital and the mesityl sp^2 orbital. Because this anti-bonding interaction becomes weaker in the tetrahedral-like structure, the HOMO energy becomes lower by this geometry change. This is also important factor to stabilize the

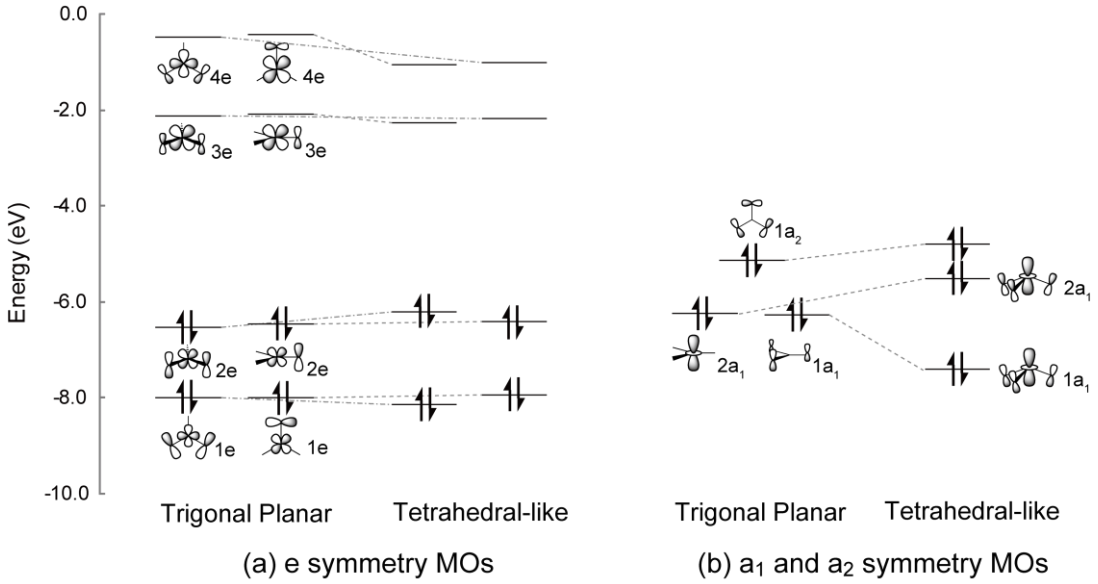

(A) Selected molecular orbitals of $Os(NAr)_3$ at tetrahedral-like and trigonal planar geometries

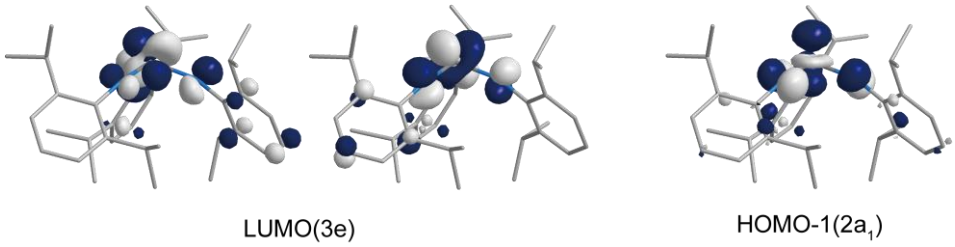

(B) Important molecular orbitals of the tetrahedral-like geometry

Scheme 4

tetrahedral-like structure relative to the trigonal planar structure.

Though the MOs of **Os(NAr)$_3$** are similar to those of **Ir(Mes)$_3$**, interesting differences in MO energy are observed between **Ir(Mes)$_3$** and **Os(NAr)$_3$**, as shown in Schemes 3 and 4(A). Because the imide ligand has two doubly occupied π orbitals but no unoccupied π-type orbital, the imide forms strong π donating interaction with the empty d_π orbitals of osmium, to raise the d_π-p_π anti-bonding orbital energy; see the 3e MO in Scheme 4(A). As a result, the 3e MO energy becomes higher than the osmium d_z^2 orbital energy. This is completely different from the d_π-p_π anti-bonding orbital of the Ir complex, which is not destabilized very much because the mesityl group is not strongly π-donating. Also, the π^* orbital of the mesityl group

participates in the π-type interaction to stabilize the iridium d_π orbital but the imide group does not have such π-type unoccupied orbital. Because the Os(VI) center has d^2 electron configuration, only the d_z^2 orbital ($2a_1$) is doubly occupied and the π anti-bonding orbitals (3e) are unoccupied. This means that the d_π-p_π anti-bonding orbital does not contribute at all to the energy stabilization of the tetrahedral-like structure unlike it in **Ir(Mes)$_3$**. It is noted that the HOMO-1 (d_z^2) energy rises by the geometry change to the tetrahedral-like structure, as shown in Scheme 4(A). This result is interpreted, as follows: Though the anti-bonding interaction between the osmium d_z^2 orbital and the imide σ-orbital becomes weak by the geometry change, the anti-bonding interaction between the osmium d_z^2 orbital and the imide π orbital is newly formed, as show in Scheme 4(B). In other words, four-electron repulsion newly occurs between doubly occupied d_z^2 and imide π orbitals in the $2a_1$ MO of the tetrahedral-like structure. This four-electron repulsion is large because the imide is strongly π-electron donating. As a result, the net energy stabilization is not produced by the geometry change to the tetrahedral-like structure. Thus, the trigonal planar structure is more stable than the tetrahedral-like structure in **Os(NAr)$_3$**.

In conclusion, **Os(NAr)$_3$** has the trigonal planar structure because of the presence of the doubly occupied π orbitals of imide and the d^2 electron configuration of Os(VI). This leads to the large re-organization energy of the osmium reaction system.

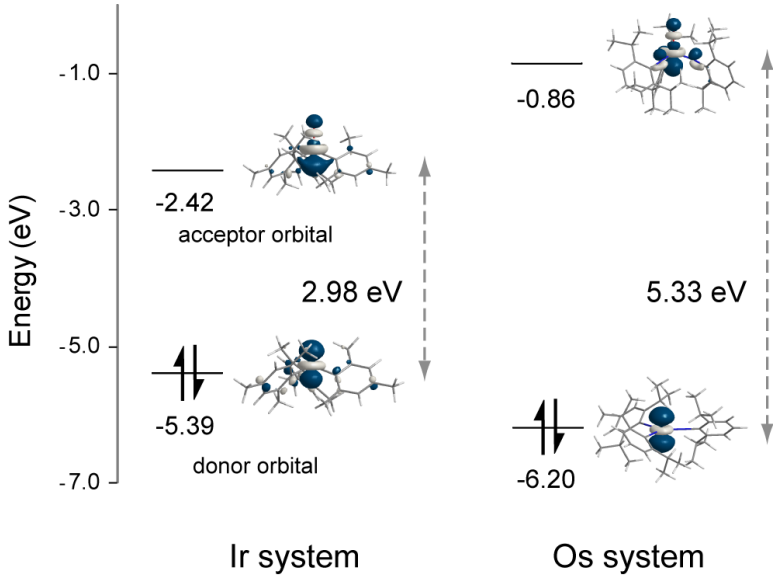

Figure 4. Electron donor orbitals of **Ir(Mes)$_3$** and **Os(NAr)$_3$** and acceptor orbitals of **Ir(Mes)$_3$=O** and **Os(NAr)$_3$=O**

1.4.3 Electronic Factor

The electronic factor deeply relates to the interaction between wave functions of ML_3 and ML_3=O. Because the electron-deficient ML_n=O interacts with the electron-rich ML_n, the charge transfer (CT) occurs from ML_n to ML_n=O. Actually, the iridium and oxygen atomic populations of **Ir(Mes)$_3$=O** increase by 0.25 e and 0.19 e, respectively, upon going to **TS$_{IrMes}$**, but the iridium atomic population of **Ir(Mes)$_3$** decreases by 0.23 e, where Mulliken population analysis was employed. The osmium and oxygen atomic populations of **Os(NAr)$_3$=O** increase by 0.13 e and 0.08 e, respectively, while the osmium atomic population of **Os(NAr)$_3$** decreases by 0.34 e upon going to **TS$_{Os}$**. In this CT interaction, the σ-type acceptor orbital of ML_3=O and the σ-type donor orbital of ML_3 play important role, because the M-O-M is almost linear in the transition state. The iridium and osmium complexes possess the similar σ-type occupied and unoccupied orbitals along z-axis, as shown in Figure 4. This means that the donor orbital overlaps with the acceptor orbital in a similar extent between iridium and osmium systems. However, the energy gap between the donor and the acceptor orbitals is much smaller in the iridium complex than in the osmium complex (Figure 4). Because of this

small energy gap in the iridium system, strong CT interaction is formed between **Ir(Mes)$_3$=O** and **Ir(Mes)$_3$**, which leads to the large electronic factor. In the osmium system, on the other hand, the CT interaction between **Os(NAr)$_3$=O** and **Os(NAr)$_3$** is considerably weak because of the large energy gap, which leads to the small electronic factor.

We calculated ionization potentials (IPs) of **Ir(CH$_3$)$_3$** and **Os(NCH$_3$)$_3$** and the electron affinities (EAs) of **Ir(CH$_3$)$_3$=O** and **Os(NCH$_3$)$_3$=O**. The IP of **Os(NCH$_3$)$_3$** is larger than that of **Ir(CH$_3$)$_3$** by 0.27 eV, and the EA of **Os(NCH$_3$)$_3$=O** is smaller than that of **Ir(CH$_3$)$_3$=O** by 0.24 eV. These results also suggest that the CT interaction occurs much easier in the iridium system than in the osmium system.[42]

The next issue to be discussed is the reason why the energy gap is large in the osmium system. This large energy gap of the osmium reaction system arises from the fact that the accepter orbital of **Os(NAr)$_3$=O** exists at higher energy and the donor orbital of **Os(NAr)$_3$** exists at lower energy than that of **Ir(Mes)$_3$=O** and **Ir(Mes)$_3$**, respectively; see Figure 4. The acceptor orbital of **Os(NAr)$_3$=O** involves the quasi d_z^2-p anti-bonding overlap between the osmium d_z^2 and nitrogen p orbitals (Figure 4), as proposed in a previous study.[25] As discussed above, this anti-bonding interaction arises from the presence of the doubly occupied p_π orbitals of the imide group; in other words, the doubly occupied p_π orbitals of the imide group raises the σ-type acceptor orbital energy of **Os(NAr)$_3$=O** through the d_z^2-p anti-bonding overlap to decrease the electronic factor. In **Ir(Mes)$_3$=O**, such anti-bonding interaction is not involved in the σ-type acceptor orbital because the mesityl group does not possess strong π-donating orbital, as discussed above. As a result, the acceptor orbital of **Ir(Mes)$_3$=O** is not destabilized very much.

The donor orbital of **Ir(Mes)$_3$** mainly consists of Ir d_z^2 orbital into which the sp^2 orbital of Mes ligand moderately mixes in anti-bonding way. On the other hand, the donor orbital of **Os(NAr)$_3$** consists of the Os d_z^2 orbital without any orbital mixing of ligand. Moreover, the osmium center takes +6 oxidation state, while the iridium center takes +3 oxidation state. As a

result, the donor orbital of **Os(NAr)$_3$** is at lower energy than that of **Ir(Mes)$_3$**.

1.5 Conclusions

The oxygen atom transfer reactions of iridium and osmium complexes were theoretically investigated with the DFT method. In small model systems in which bulky substituents were replaced with methyl groups, the μ-oxo dinuclear iridium and osmium complexes were optimized as stable species, indicating that the oxygen atom transfer reaction does not occur in model systems. In real systems, on the other hand, the transition states of both iridium and osmium reactions were successfully optimized. It is noted here that the transition state is unsymmetrical in the iridium system but symmetrical in the osmium system. Interestingly, symmetrical μ-oxo bridged dinuclear intermediate was optimized in the iridium system, geometry of which agrees well with experimental one. Besides the transition states and the symmetrical intermediate, unsymmetrical intermediate was newly optimized in the iridium system, while no intermediate was optimized in the osmium system.

The activation barrier in gas phase is calculated to be 3.9 and 33.3 kcal/mol for the iridium and osmium reaction systems, respectively, in the potential energy surface.[40] The $\Delta G^{0\ddagger}$ value is evaluated to be 8.8 and 43.8 kcal/mol for the iridium and osmium reaction systems, respectively, in solution at 298.15 K. These results are consistent with experimental results that the oxygen atom transfer reaction rapidly occurs in the iridium system but very slowly in the osmium system.[25]

The origin of the large difference in the activation barrier is discussed in terms of nuclear and electronic factors. The nuclear factor arises from re-organization energy which is defined as the destabilization energy necessary to distort the reactant from the equilibrium structure into the transition state structure. The nuclear factor is much larger in the osmium system than in the iridium system. In the osmium reaction system, the activation barrier without re-organization energy is about 70 % of the total activation barrier, indicating that the

nuclear factor largely contributes to the difference in the reactivity between the iridium and osmium complexes but the electronic factor also contributes to the difference. The larger nuclear factor of osmium system arises from the fact that substantially large structural changes must occur upon going from trigonal planar **Os(NAr)$_3$** to the tetrahedral-like transition state. The small re-organization energy of the iridium system arises from the fact that structural change little occurs upon going from **IM$_{IrMes}$** to **TS$_{IrMes}$** because **Ir(Mes)$_3$**, **Ir(Mes)$_3$=O**, **TS$_{IrMes}$**, and **IM$_{IrMes}$** all take tetrahedral-like structure around the iridium center. The electronic factor was discussed in terms of the interaction between the donor orbital of ML_3 and the acceptor orbital of ML_3=O. Since the donor and acceptor orbitals are similar between the iridium and osmium complexes, it is likely that the extent of orbital overlap is similar between these two systems. However, the energy gap between the donor and acceptor orbitals is much larger in the osmium reaction system than in the iridium reaction system, which leads to the smaller electronic factor in the osmium system than in the iridium system. The large energy gap in the osmium system arises from both the electron donor and electron acceptor orbitals; the electron donor orbital of **Os(NAr)$_3$** is at much lower energy than that of **Ir(Mes)$_3$** since osmium center takes +6 oxidation state while iridium center takes +3 oxidation state. Similarly, the electron acceptor orbital of **Os(NAr)$_3$=O** is at much high energy than that of **Ir(Mes)$_3$=O** due to the quasi-d_z^2-p anti-bonding overlap between the osmium d_z^2 and nitrogen p orbitals.

Acknowledgements

This work was financially supported by Grand-in-Aids on basis research (No. 1530012), Priority Areas for “Molecular Theory for Real Systems” (No. 461), and NAREGI Project from the Ministry of Education, Science, Sports, and Culture. Some of theoretical calculations were performed with SGI workstations of Institute for Molecular Science (Okazaki, Japan), and some of them were carried out with PC cluster computers in our laboratory.

References

(1) Holm, R. H. *Chem. Rev.* **1987**, 87, 1401.

(2) Woo, L. K. *Chem. Rev*. **1993**, 93, 1125.

(3) Shilov, A. E.; Shteinman, A. A. *Acc. Chem. Res.* **1999**, 32, 763.

(4) Hess, J. S.; Leelasubcharoen, S.; Rheingold, A. L.; Doren, D. J.; Theopold, K. H. *J. Am. Chem. Soc*. **2002**, 124, 2454.

(5) Merkx, M.; Kopp, D. A.; Sazinsky, M. H.; Blazyk, J. L.; Muller, J.; Lippard, S. J. *Angew. Chem., Int. Ed*. **2001**, 40, 2782.

(6) Dobler, C.; Mehltretter, G.; Beller, M. *Angew. Chem., Int. Ed.* **1999**, 38, 3026.

(7) Kolb, H. C.; VanNieuwenhze, M. S.; Sharpless, K. B. *Chem. Rev.* **1994**, 94, 2483.

(8) Andersson, M. A.; Epple, R.; Fokin, V. V.; Sharpless, K. B. Angew. *Chem., Int. Ed.* **2002**, 41, 472.

(9) Chen, K.; Costas, M.; Kim, J.; Tipton, A. K.; Que, L., Jr. *J. Am. Chem. Soc*. **2002**, 124, 3026.

(10) Ryu, J. Y.; Kim, J.; Costas, M.; Chen, K.; Nam, W.; Que, L., Jr. *Chem. Commun*. **2002**, 1288.

(11) Holm, R. H.; Kennepohl, P.; Solomon, E. I. *Chem. Rev*. **1996**, 96, 2239.

(12) Ostovic, D.; Bruice, T. C. *Acc. Chem. Res.* **1992**, 25, 314.

(13) de Visser, S. P.; Ogliaro, F.; Sharma, P. K.; Shaik, S. *Angew. Chem., Int. Ed*. **2002**, 41, 1947.

(14) de Visser, S. P.; Ogliaro, F.; Harris, N.; Shaik, S. *J. Am. Chem. Soc.* **2001**, 123, 3037.

(15) de Visser, S. P.; Ogliaro, F.; Sharma, P. K.; Shaik, S. *J. Am. Chem. Soc.* **2002**, 124, 11809.

(16) Ogliaro, F.; Harris, N.; Cohen, S.; Filatov, M.; de Visser, S. P.; Shaik, S. *J. Am. Chem. Soc*. **2000**, 122, 8977.

(17) Brown, S. N.; Mayer, J. M. *Inorg. Chem.* **1992**, 31, 4091.

(18) Gangopadhyay, J.; Sengupta, S.; Bhattacharyya, S.; Chakraborty, I.; Chakravorty, A. *Inorg. Chem.* **2002**, 41, 2616.

(19) Sastri, C. V.; Oh, K.; Lee, Y. J.; Seo, M. S.; Shin, W.; Nam, W.; *Angew. Chem. Int. Ed.* **2006**, 45, 3992.

(20) de Visser, S. P.; Lee, Y.-M.; Nam, W.; Eur. J. *Inorg. Chem*. **2008**, 1027.

(21) Matsuda, T.; Tanaka, K.; Tanaka, T. *Inorg. Chem*. **1979**, 18, 454.

(22) Seymore, S. B.; Brown, S. N. *Inorg. Chem*. **2000**, 39, 325.

(23) Veige, A. S.; Slaughter, L. M.; Lobkovsky, E. B.; Wolczanski, P. T.; Matsunaga, N.; Decker, S. A.; Cundari, T. R. *Inorg. Chem*. **2003**, 42, 6204.

(24) Pietsch, M. A.; Hall, M. B. *Inorg. Chem*. **1996**, 35, 1273.

(25) Fortner, K. C.; Laitar, D. S.; Muldoon, J.; Pu, L. H.; Braun-Sand, S. B.; Wiest, O.; Brown, S. N. *J. Am. Chem. Soc*. **2007**, 129, 588.

(26) We theoretically evaluated Ir=O bond energy of **$Ir(CH_3)_3$=O** and Os=O bond energy of **$Os(NCH_3)_3$=O** with various methods; see supporting information, Table A3. Theoretically evaluated difference between the Ir=O and Os=O bond energies does not agree with experimental difference (0.84 kcal/mol). Further investigation is necessary for this issue.

(27) Becke, A. D. *J. Chem. Phys.* **1993**, 98, 5648.

(28) (a) Lee, C.; Yang, W.; Parr, R. G. *Phys. Rev. B* **1988**, 37, 785.; (b) Miehlich, B.; Savin, A.; Stoll, H.; Preuss, H. *Chem. Phys. Lett.***1989**, 157, 200.

(29) D. Andrae, U. Haussermann, M. Dolg, H. Stoll, and H. Preuss, *Theor. Chem. Acta.* **1990**, 77, 123.

(30) R. Ditchfield, W. J. Hehre, and J. A. Pople, *J. Chem. Phys.* **1971**, 54, 724.

(31) Dunning, T. H., Jr. *J. Chem. Phys*. **1989**, 90, 1007.

(32) Hay, P. J.; Wadt, W. R. *J. Chem. Phys.* **1985**, 82, 299.

(33) Miertus, S; Scrocco, E.; Tomasi, J.; *Chem. Phys.***1981**, 55, 117.

(34) Pople, J. A.; et al. *Gaussian 03, revision D.02*; Gaussian, Inc., Wallingford CT, 2004.

(35) Mammen, M.; Shakhnovich, E. I.; Deutch, J. M.; Whitesides, G. M.; *J. Org. Chem.* **1998**, 63, 3821.

(36) Hay-Motherwell, R. S.; Wilkinson, G; Hussain-Bates, B.; Hursthouse, M. B. *J. Chem. Soc., Dalton Trans.* **1992**, 3477.

(37) Hay-Motherwell, R. S.; Wilkinson, G; Hussain-Bates, B.; Hursthouse, M. B. *Polyhedron*, **1993**, 12, 2009.

(38) Anhaus, J. T.; Kee, T. P.; Schofield, M. H.; Schrock, R. R. *J. Am. Chem. Soc.* **1990**, 112, 1642.

(39) Schofield, M. H.; Kee, T. P.; Anhaus, J. T.; Schrock, R. R.; Johnson, K. H.; Davis, W. M. *Inorg. Chem.* **1991**, 30, 3595.

(40) William, D. S.; Schrock, R. R.; *Organometallics*, **1963**, 12, 1148

(41) In iridium system, the activation barrier in the potential energy surface is defined as the zero-point corrected energy difference between the infinite separation system and the intermediate (**IM_{IrMes}**), because the transition state is more stable than the infinite separation system. On the other hand, the activation barrier in the free energy surface ($\Delta G^{0\ddagger}$) is defined as the energy difference between the transition state and the infinite separation system, because the intermediate is less stable that the infinite separation system in the free energy surface.

(42) In **$IrMe_3$** and **$Os(NMe)_3$**, the σ-type donor orbitals are HOMO, and in **$IrMe_3$=O** and **$Os(NMe)_3$=O**, the σ^*-type acceptor orbitals are LUMO. We evaluated the IPs of the former HOMOs and the EAs of the latter LUMOs with the DFT/BS-II and CCSD(T)/BS-II; see Appendix Table A4. We also tried to evaluate the IPs of the σ-type donor orbitals of **$Ir(Mes)_3$** and **$Os(NAr)_3$**, but failed it; though we started the SCF calculation with the singly-occupied σ-type donor orbital, the π-orbital became singly-occupied and the σ-type donor orbital became doubly-occupied during the SCF calculation. This is because the HOMOs of **$Ir(Mes)_3$** and **$Os(NAr)_3$** are the π orbital of the ligand. Also, we tried to evaluate the EAs of the σ-type

acceptor orbitals of **Ir(Mes)$_3$=O** and **Os(NAr)$_3$=O**, but failed it: The π^* orbital of the ligand became the singly-occupied and the σ^*-type acceptor orbital became unoccupied during the SCF calculation, even though we started the SCF calculation with the singly-occupied σ^*-type acceptor orbital. Thus, we presented discussion based on the IPs and EAs of model systems.

1.6 Appendix

Complete Representation of Ref. 32

Frisch, M. J.; Trucks, G. W.; Schlegel, H. B.; Scuseria, G. E.; Robb, M. A.; Cheeseman, J. R.; Montgomery, J. A., Jr.; Vreven, T.; Kudin, K. N.; Burant, J. C.; Millam, J. M.; Iyengar, S. S.; Tomasi, J.; Barone, V.; Mennucci, B.; Cossi, M.; Scalmani, G.; Rega, N.; Petersson, G. A.; Nakatsuji, H.; Hada, M.; Ehara, M.; Toyota, K.; Fukuda, R.; Hasegawa, J.; Ishida, M.; Nakajima, T.; Honda, Y.; Kitao, O.; Nakai, H.; Klene, M.; Li, X.; Knox, J. E.; Hratchian, H. P.; Cross, J. B.; Bakken, V.; Adamo, C.; Jaramillo, J.; Gomperts, R.; Stratmann, R. E.; Yazyev, O.; Austin, A. J.; Cammi, R.; Pomelli, C.; Ochterski, J. W.; Ayala, P. Y.; Morokuma, K.; Voth, G. A.; Salvador, P.; Dannenberg, J. J.; Zakrzewski, V. G.; Dapprich, S.; Daniels, A. D.; Strain, M. C.; Farkas, O.; Malick, D. K.; Rabuck, A. D.; Raghavachari, K.; Foresman, J. B.; Ortiz, J. V.; Cui, Q.; Baboul, A. G.; Clifford, S.; Cioslowski, J.; Stefanov, B. B.; Liu, G.; Liashenko, A.; Piskorz, P.; Komaromi, I.; Martin, R. L.; Fox, D. J.; Keith, T.; Al-Laham, M. A.; Peng, C. Y.; Nanayakkara, A.; Challacombe, M.; Gill, P. M. W.; Johnson, B.; Chen, W.; Wong, M. W.; Gonzalez, C.; Pople, J. A. *Gaussian 03, Revision D.02*, Gaussian, Inc., Wallingford CT, 2004.

Why both d_π-π bonding and anti-bonding MO energy becomes lower by the geometry change from the tetrahedral structure to the trigonal planar one of $Ir(Mes)_3$?

In this section, we discuss about the MO energy changes (Scheme 3) of **$Ir(Mes)_3$** upon going from tetrahedral geometry and trigonal planar geometry.

Frontier orbitals of **$Ir(Mes)_3$** are mainly consist of Ir 5d orbital and mesityl π orbitals. The d_π-π bonding orbital is found as HOMO-2 in Scheme 3. This orbital is stabilized by the geometry change from the trigonal planar to the tetrahedral-like structure, because the overlap between the Ir d_π and the mesityl π orbitals increases by this geometry change.

Usually, the d_π-p_π anti-bonding orbital energy rises when the d_π-π bonding orbital energy becomes lower. However, the HOMO-1 energy becomes moderately lower by this geometry change, unexpectedly. Actually, the shape of the HOMO-1 (see Scheme A3) cannot be understood in terms of simple overlap between the Ir d_π and the mesityl π orbital. The shape of HOMO-1 can be explained by the mixing of the mesityl π^* orbital into the d_π-p_π orbital, as follows: If the π^* of mesityl does not mix into the iridium d_π orbital, the contribution of C1 p_π is the same as that of C4 p_π and the contribution of C1 p_π is larger than that of C2 p_π. However, the contribution of C1 p_π is smaller than that of C4 p_π in the HOMO-1. Also, the contribution of C1 p_π is similar to that of C2 p_π in the HOMO-1, as shown in Scheme A3. These results indicate that the π^* of mesityl mixes into the d_π orbital.

As a result, the d_π-p_π anti-bonding orbital energy becomes moderately lower by this geometry change from the tetrahedral-like structure to the trigonal-planar one.

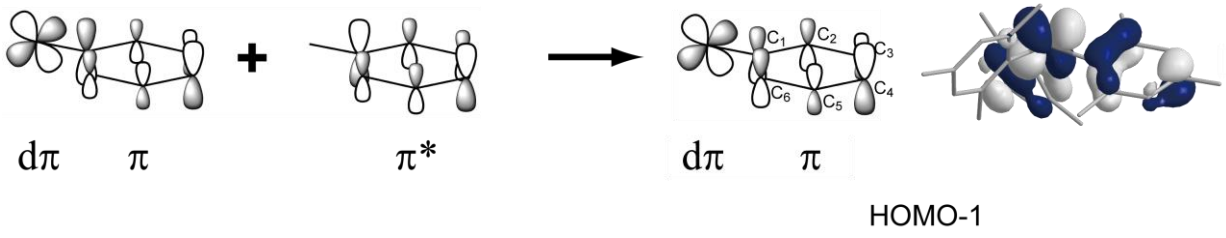

Scheme A3. Orbital mixing in the HOMO-1 of the tetrahedral-like structure

Brief summary for the Whitesides' method for the correction of the translational entropy in solvent phase

The Gibbs free energy is calculated for ideal gas as follows;

$$G = H + TS = E + RT + TS \quad (1)$$

where E is the sum of electronic and thermal energies, S is the total entropy, T is temperature (K), and R is the gas constant ($J \cdot K^{-1} \cdot mol^{-1}$). S is partitioned into translational, rotational, vibrational components (eq 2).

$$S = S_{trans} + S_{vib} + S_{rot} \quad (2)$$

As a matter of fact, each component takes different values in gas and condensed phase. Especially, the translational entropy (S_{trans}) is significantly different between them since translation movement is considerably suppressed in solution. On the contrary, the vibrational and rotational entropies (S_{vib} and S_{rot}) are moderately different between them. Thus, we must evaluate S_{trans} in solution when we need to discuss free energy change in solution.

In gas phase, S_{trans} is given by the Sackur-Tetrode equation;[1]

$$S_{trans} = R\ln\left[\left(\frac{10^{-15/2}}{N_A{}^4[X]}\right)\left(\frac{2\pi MRTe^{5/3}}{h^2}\right)^{3/2}\right] \quad (3)$$

where N_A is Avogadro's number, h is Plank's constant, M is the molecular mass (g/mol) and [X] is the concentration (mol/L) of the particles. [X] = 4.46×10^{-2} (mol/L) for the standard state in gas phase since 1 mol at 1 atom occupies 22.4 L. Equation 3 successfully predicts the entropy of monatomic gases, but considerably overestimate S_{trans} in the liquid and solution phase. Qualitatively, the main reason for the failure of eq 3 to predict S_{trans} in condensed phase is that it ignores molecular volume, V_{molec}. In solution, it becomes the significant component in the total volume unlike in the gas phase. In other words, the volume available to the molecule movement (V_{free}) becomes much smaller in the solution than in the gas.

In Whitesides' model, V_{free} in solvent is corrected as follows: i) The liquid is described by an array of cubes (cube **A**). ii) The size (d) of cube **A** is defined by

$$d = \sqrt[3]{\left(\frac{10^{27}}{[X]N_A}\right)} \quad (4)$$

where [X] is the concentration (mol/L) of solvent molecule in the liquid. iii) Molecule is also defined as the smaller cube (cube **B**) or sphere. Its volume was evaluated with van der Waals volume in ref 35. iv) In the solvent system, one solvent molecule can move in the free space surrounded by solvent molecules. This corresponds to the movement of cube **B** in cube **A**. V_{free} is defined as follows;

$$V_{free} = C_{free}\left\{\sqrt[3]{\left(\frac{10^{27}}{[X]N_A}\right)} - \sqrt[3]{V_{molec}}\right\}^3 \quad (5)$$

where the constant C_{free} depends on the shape of the model; for cubic molecules, C_{free} = 8 and for spherical molecules, C_{free} = 6.3. For the solution, they assume that the solute molecule and solvent molecule have the same V_{free}. This is valid only for infinitely dilute solution. Although further improvement of their model is necessary for the general cases, this is one of reasonable ways to evaluate S_{trans} in solution.

The oxygen atom transfer reaction of iridium and osmium complexes is carried out in dichloromethane and benzene solutions, respectively. We employed the cube model for solvent molecules in eq (5) thus C_{free} = 8. Concentration ($g \cdot cm^{-3}$) of solvents are taken from experimental value at 20 ˚C ([X] = 1.3266 for dichloromethane and 0.8765 for benzene).[2] Molecular volume of solvents (V_{molec}, in $Å^3$) are taken as 8.19 for dichloromethane and 10.93 for benzene molecules. These are calculated according to the electronic density envelope of 0.001 ($e/Bohr^3$) at B3LYP/BS-I level. For the Gibbs free energy with and without corrections, see Table 3 in the article.

(1) Gurney, R. W.; *Introduction to Statistical Mechanics*, 1st ed.; McGraw-Hill Book Company; New York, **1949**.

(2) Lide, D. R. (ed.); *CRC Handbook of Chemistry and Physics*, 84th ed.; CRC Press; Boca Raton, **2003**.

Table A1a. Cartesian coordinates of **Ir(Mes)$_3$** optimized by B3LYP/BS-I method.

Atomic Symbol	Coordinates (Å)		
	X	Y	Z
Ir	0.0006	0.0001	-0.6706
C	1.8533	-0.3986	-0.0147
C	2.5043	-1.4128	-0.7706
C	3.8460	-1.7275	-0.5144
C	4.5723	-1.0732	0.4888
C	3.9098	-0.0977	1.2464
C	2.5668	0.2532	1.0243
H	4.3279	-2.5004	-1.1096
H	4.4510	0.4083	2.0425
C	-1.2716	-1.4050	-0.0150
C	-2.4732	-1.4651	-0.7742
C	-3.4163	-2.4699	-0.5177
C	-3.2152	-3.4224	0.4893
C	-2.0414	-3.3331	1.2501
C	-1.0660	-2.3456	1.0273
H	-1.8754	-4.0524	2.0487
H	-4.3248	-2.5036	-1.1156
C	-0.5808	1.8039	-0.0144
C	-0.0282	2.8758	-0.7697
C	-0.4282	4.1945	-0.5135
C	-1.3594	4.4952	0.4886
C	-1.8724	3.4330	1.2458
C	-1.5029	2.0949	1.0240
H	-0.0002	4.9989	-1.1083
H	-2.5823	3.6480	2.0412
H	2.4198	-2.5575	-2.6142
C	0.1565	-2.3395	1.9200
C	-2.1132	1.0319	1.9127
H	1.2726	-3.1008	-1.3773
H	0.9518	-1.6282	-2.3015
H	0.0163	-3.0218	2.7649
C	1.0455	2.6253	-1.8167
H	-1.3557	0.3429	2.2967
H	-2.6228	1.4927	2.7653
H	-1.8810	-0.0202	-2.3113
C	1.7493	-2.2156	-1.8181
H	1.0589	-2.6507	1.3828
H	2.0503	2.6572	-1.3758
H	1.7766	2.2503	1.3755
H	-2.8453	0.4188	1.3757
H	-3.4215	-0.8251	-2.6202
H	-3.3155	0.4445	-1.3883
C	-2.7890	-0.4136	-1.8259
H	1.0050	3.3764	-2.6132
H	0.3619	-1.3409	2.3162
H	0.9378	1.6405	-2.3001
H	2.6123	1.5304	2.7604
C	1.9524	1.3127	1.9141
H	0.9825	0.9963	2.3083
C	6.0301	-1.3936	0.7347
H	6.6886	-0.7390	0.1467
H	6.2975	-1.2588	1.7885
H	6.2662	-2.4262	0.4555
C	-1.8129	5.9174	0.7336
H	-2.7041	6.1616	0.1387
H	-2.0721	6.0792	1.7857
H	-1.0345	6.6388	0.4623
C	-4.2211	-4.5251	0.7355
H	-3.9770	-5.4265	0.1561
H	-4.2456	-4.8164	1.7914
H	-5.2318	-4.2174	0.4461

Table A1b. Cartesian coordinates of **Ir(Mes)$_3$=O** optimized by B3LYP/BS-I method.

Atomic Symbol	Coordinates (Å)		
	X	Y	Z
Ir	-0.0036	0.0003	-0.7034
O	-0.0049	0.0026	-2.4500

C	-1.9162	-0.2260	0.0065
C	-2.9178	0.5406	-0.6629
C	-4.2641	0.3728	-0.3088
C	-4.6670	-0.5144	0.6971
C	-3.6711	-1.2323	1.3641
C	-2.3055	-1.1173	1.0418
H	-5.0142	0.9625	-0.8297
H	-3.9550	-1.9089	2.1660
C	0.7653	1.7666	0.0066
C	1.9338	2.2440	-0.6605
C	2.4648	3.4933	-0.3088
C	1.8975	4.2912	0.6927
C	0.7733	3.7943	1.3571
C	0.1863	2.5559	1.0360
H	0.3283	4.3829	2.1552
H	3.3534	3.8433	-0.8279
C	1.1501	-1.5430	0.0076
C	0.9953	-2.7912	-0.6676
C	1.8176	-3.8713	-0.3148
C	2.7812	-3.7774	0.6967
C	2.8949	-2.5589	1.3714
C	2.1104	-1.4357	1.0494
H	1.6888	-4.8139	-0.8404
H	3.6169	-2.4676	2.1788
H	-3.4939	2.1291	-2.0021
C	-1.0228	2.1485	1.8565
C	2.3423	-0.1894	1.8821
H	-1.8178	2.2504	-1.4417
H	-2.2394	1.0579	-2.6612
H	-1.1577	2.8429	2.6918
C	-0.0287	-3.0210	-1.7629
H	1.4127	0.2378	2.2697
H	2.9795	-0.4273	2.7397
H	2.0429	1.3920	-2.6558
C	-2.6011	1.5479	-1.7519
H	-1.9420	2.1564	1.2636
H	-1.0311	-2.6964	-1.4587
H	-0.8861	-2.7514	1.2815
H	2.8359	0.6003	1.3083
H	3.5988	1.9392	-1.9957
H	2.8600	0.4314	-1.4320
C	2.6471	1.4604	-1.7457
H	-0.0822	-4.0847	-2.0145
H	-0.9281	1.1423	2.2760
H	0.2199	-2.4614	-2.6702
H	-1.8769	-2.4120	2.7060
C	-1.3444	-1.9503	1.8685
H	-0.5246	-1.3578	2.2856
C	-6.1285	-0.6916	1.0410
H	-6.6310	-1.3459	0.3155
H	-6.2550	-1.1420	2.0308
H	-6.6612	0.2663	1.0335
C	3.6724	-4.9501	1.0378
H	4.5520	-4.9851	0.3802
H	4.0383	-4.8889	2.0682
H	3.1437	-5.9026	0.9210
C	2.4772	5.6454	1.0330
H	2.1359	6.4131	0.3250
H	2.1775	5.9688	2.0352
H	3.5724	5.6344	0.9931

Table A1c. Cartesian coordinates of **IM_{IrMes}** optimized by B3LYP/BS-III method.

Atomic Symbol	Coordinates (Å)		
	X	Y	Z
O	0.0003	-0.0001	0.0002
Ir	-1.9598	0.0004	-0.0032
Ir	1.9600	-0.0004	0.0033
C	-2.7537	-1.7686	-0.6371
C	-2.1341	-2.9254	-0.0723
C	-2.4638	-4.1955	-0.5660
C	-3.4048	-4.3880	-1.5863
C	-4.0473	-3.2467	-2.0755

C	-3.7596	-1.9425	-1.6263	C	3.4227	-0.8318	-4.5820
H	-1.9764	-5.0617	-0.1231	C	4.0650	0.1609	-3.8360
H	-4.8212	-3.3647	-2.8312	C	3.7714	0.4265	-2.4837
H	0.9071	-3.1839	-2.6260	H	1.9873	-2.4302	-4.4399
H	0.2026	-1.8563	-1.6599	H	4.8434	0.7531	-4.3129
H	5.4910	1.7272	-2.4354	H	0.9111	-0.6639	4.0778
H	4.9745	1.1492	-0.8218	C	4.6046	0.8276	2.2135
H	4.0476	2.4252	-1.6491	C	3.7563	-2.3772	0.8804
C	4.6161	1.4949	-1.8052	H	1.5629	0.5455	2.9331
H	4.0290	-2.6601	-1.2674	H	0.1977	-0.5022	2.4479
C	4.6008	-2.3337	-0.3845	H	5.4753	1.2603	2.7346
C	-2.7594	0.3353	1.8437	C	1.1446	-2.3651	-1.9241
C	-2.1404	1.4006	2.5668	C	3.3986	-3.5594	3.0212
C	-2.4759	1.6077	3.9122	C	2.4587	-2.5775	3.3616
C	-3.4227	0.8225	4.5837	H	0.2017	2.3665	-0.7846
C	-4.0637	-0.1699	3.8363	C	-4.6128	-1.5018	1.8036
C	-3.7699	-0.4330	2.4835	C	1.1431	-0.4745	3.0150
H	-1.9891	2.4228	4.4440	C	-1.1466	2.3628	1.9281
H	-4.8412	-0.7639	4.3123	H	4.0341	0.2258	2.9382
C	2.1345	2.9255	0.0653	C	-1.1453	-2.8494	1.0843
C	2.7539	1.7701	0.6331	H	1.5620	-2.8142	-1.0037
C	3.7598	1.9463	1.6219	C	-4.6047	-0.8225	-2.2152
C	4.0476	3.2516	2.0678	H	1.9706	-2.6239	4.3331
C	3.4053	4.3917	1.5757	C	-4.5993	2.3335	0.3916
C	2.4643	4.1968	0.5558	C	4.0417	-3.4166	1.7880
H	4.8215	3.3715	2.8231	C	-1.1455	0.4800	-3.0148
H	1.9772	5.0620	0.1106	H	0.9115	3.8624	-1.4556
C	-2.1334	1.5209	-2.5030	H	1.5668	2.2691	-1.9354
C	-2.7526	1.4332	-1.2187	H	-4.9716	-1.1555	0.8206
C	-3.7561	2.3793	-0.8740	H	-4.0429	-2.4310	1.6466
C	-4.0421	3.4205	-1.7794	H	-5.4876	-1.7363	2.4334
C	-3.4004	3.5655	-3.0130	C	1.1459	2.8467	-1.0913
C	-2.4610	2.5839	-3.3563	H	-0.2045	1.8552	1.6620
H	-4.8142	4.1359	-1.5037	H	-1.5650	2.8137	1.0090
H	-1.9739	2.6321	-4.3282	H	-0.9092	3.1801	2.6317
C	2.7598	-0.3394	-1.8428	C	2.7524	-1.4306	1.2222
C	2.1396	-1.4051	-2.5642	H	4.9697	0.1496	1.4247
C	2.4750	-1.6148	-3.9093	H	-0.2018	-2.3670	0.7789

H	-1.5666	-2.2751	1.9304
H	-0.9095	-3.8660	1.4450
C	2.1317	-1.5161	2.5060
H	-4.9697	-0.1464	-1.4247
H	-4.0343	-0.2190	-2.9385
H	-5.4753	-1.2540	-2.7372
H	5.4697	-3.0034	-0.2698
H	4.8143	-4.1323	1.5145
H	-4.9678	1.3127	0.5844
H	-4.0264	2.6575	1.2747
H	-5.4679	3.0040	0.2793
H	4.9688	-1.3131	-0.5793
H	-0.2005	0.5048	-2.4468
H	-1.5665	-0.5397	-2.9369
H	-0.9124	0.6729	-4.0768
C	3.7108	-4.7158	3.9528
H	2.9951	-5.5413	3.8001
H	4.7254	-5.1028	3.7649
H	3.6446	-4.3970	5.0057
C	-3.7133	4.7237	-3.9422
H	-4.7259	5.1135	-3.7493
H	-2.9944	5.5468	-3.7919
H	-3.6528	4.4056	-4.9957
C	3.7438	-1.0598	-6.0475
H	3.0311	-0.5155	-6.6900
H	4.7594	-0.7022	-6.2826
H	3.6803	-2.1311	-6.2985
C	-3.7189	-5.7713	-2.1253
H	-4.7336	-5.7997	-2.5543
H	-3.0036	-6.0507	-2.9173
H	-3.6534	-6.5258	-1.3246
C	-3.7438	1.0477	6.0496
H	-4.7589	0.6885	6.2843
H	-3.0303	0.5033	6.6911
H	-3.6816	2.1187	6.3023
C	3.7196	5.7764	2.1111
H	3.0060	6.0568	2.9043
H	4.7353	5.8065	2.5377
H	3.6516	6.5292	1.3090

Table A1d. Cartesian coordinates of **Os(NAr)$_3$** optimized by B3LYP/BS-III method.

Atomic Symbol	Coordinates (Å)		
	X	Y	Z
Os	-0.0006	-0.0015	0.0055
N	-1.3805	-1.0932	0.0045
C	-2.4624	-1.9434	0.0006
C	-2.3815	-3.1853	-0.7057
C	-3.5024	-4.0227	-0.7004
C	-4.6651	-3.6742	-0.0076
C	-4.7318	-2.4647	0.6894
C	-3.6530	-1.5739	0.7030
H	-3.4675	-4.9640	-1.2372
H	-5.5187	-4.3450	-0.0108
H	-5.6405	-2.2101	1.2232
N	1.6351	-0.6499	0.0021
C	2.9132	-1.1595	-0.0022
C	3.9462	-0.4681	-0.7111
C	5.2330	-1.0179	-0.7064
C	5.5156	-2.1968	-0.0112
C	4.5036	-2.8594	0.6889
C	3.1917	-2.3732	0.7029
H	6.0289	-0.5169	-1.2458
H	6.5239	-2.5990	-0.0149
H	4.7401	-3.7717	1.2247
N	-0.2570	1.7392	0.0047
C	-0.4525	3.1014	0.0009
C	-1.5660	3.6528	-0.7087
C	-1.7305	5.0423	-0.7037
C	-0.8497	5.8745	-0.0076
C	0.2288	5.3271	0.6926
C	0.4610	3.9474	0.7062
H	-2.5611	5.4828	-1.2437

H	-1.0036	6.9492	-0.0109
H	0.9020	5.9863	1.2290
C	-3.7099	-0.2723	1.4962
C	-3.1827	-0.4887	2.9379
C	-5.1103	0.3735	1.5224
H	-3.0294	0.4340	1.0077
H	-2.1598	-0.8784	2.9285
H	-3.1829	0.4584	3.4910
H	-3.8183	-1.2011	3.4785
H	-5.0520	1.3638	1.9886
H	-5.8249	-0.2182	2.1073
H	-5.5158	0.4954	0.5118
C	-1.1265	-3.5461	-1.4943
C	-0.8336	-5.0600	-1.5271
C	-1.2035	-2.9740	-2.9329
H	-0.2809	-3.0567	-0.9983
H	-0.8159	-5.4877	-0.5184
H	-1.5764	-5.6100	-2.1174
H	0.1439	-5.2375	-1.9904
H	-2.0446	-3.4172	-3.4805
H	-0.2812	-3.1972	-3.4830
H	-1.3370	-1.8875	-2.9173
C	3.6289	0.7971	-1.5017
C	4.7854	1.8175	-1.5206
C	3.1898	0.4424	-2.9454
H	2.7730	1.2769	-1.0142
H	5.1341	2.0482	-0.5078
H	4.4479	2.7507	-1.9863
H	5.6425	1.4570	-2.1021
H	2.9199	1.3511	-3.4971
H	4.0038	-0.0569	-3.4854
H	2.3213	-0.2242	-2.9395
C	2.0959	-3.0736	1.5000
C	2.2392	-4.6091	1.5264
C	2.0237	-2.5071	2.9411
H	1.1421	-2.8393	1.0143
H	2.3318	-5.0214	0.5154
H	1.3556	-5.0551	1.9973
H	3.1125	-4.9306	2.1068
H	1.8475	-1.4266	2.9302
H	2.9605	-2.6984	3.4790
H	1.2063	-2.9812	3.4979
C	1.6145	3.3459	1.5028
C	1.1598	2.9984	2.9434
C	2.8740	4.2357	1.5314
H	1.8872	2.4032	1.0153
H	0.3103	2.3078	2.9321
H	1.9783	2.5246	3.4988
H	0.8598	3.9053	3.4829
H	3.7012	3.6903	2.0003
H	2.7176	5.1511	2.1149
H	3.1850	4.5247	0.5213
C	-2.5034	2.7471	-1.5012
C	-3.9630	3.2448	-1.5296
C	-1.9706	2.5378	-2.9418
H	-2.4977	1.7674	-1.0106
H	-4.3418	3.4368	-0.5195
H	-4.0721	4.1657	-2.1151
H	-4.6030	2.4869	-1.9961
H	-1.9397	3.4910	-3.4842
H	-2.6227	1.8505	-3.4944
H	-0.9607	2.1155	-2.9306

Table A1e. Cartesian coordinates of **Os(NAr)$_3$=O** optimized by B3LYP/BS-III method.

Atomic Symbol	Coordinates (Å)		
	X	Y	Z
O	-0.0544	0.0405	-2.7875
Os	0.0154	0.0264	-1.0296
N	-1.5997	-0.3511	-0.4097
N	1.1862	-1.2211	-0.5559
N	0.5346	1.6334	-0.4884
C	-2.6013	-1.0789	0.2033

C	-3.0182	-0.7461	1.5276	C	-3.4130	-1.3832	-2.9359
C	-4.0492	-1.5000	2.1016	H	-3.0668	-1.5699	-3.9587
C	-4.6555	-2.5485	1.4064	H	-4.5087	-1.4379	-2.9247
C	-4.2452	-2.8584	0.1062	H	-3.1118	-0.3689	-2.6584
C	-3.2268	-2.1386	-0.5280	C	-3.1504	-3.8586	-2.4367
H	-4.3834	-1.2654	3.1061	H	-2.7084	-4.0354	-3.4234
H	-5.4511	-3.1203	1.8734	H	-2.7598	-4.6168	-1.7485
H	-4.7278	-3.6730	-0.4206	H	-4.2328	-4.0082	-2.5337
C	0.4017	2.8051	0.2360	C	1.7351	1.7401	2.1481
C	0.9316	2.8965	1.5603	H	1.2819	0.8063	1.7898
C	0.7474	4.0955	2.2574	C	3.1918	1.7718	1.6170
C	0.0786	5.1793	1.6785	H	3.2138	1.7613	0.5228
C	-0.3987	5.0889	0.3692	H	3.7508	0.9010	1.9780
C	-0.2388	3.9192	-0.3838	H	3.7026	2.6793	1.9615
H	1.1329	4.1893	3.2661	C	1.7294	1.6910	3.6883
H	-0.0549	6.0967	2.2430	H	2.2144	0.7693	4.0293
H	-0.8979	5.9426	-0.0767	H	0.7107	1.7095	4.0914
C	2.3050	-1.7248	0.0808	H	2.2846	2.5301	4.1246
C	2.1540	-2.4506	1.3009	C	-0.7520	3.8249	-1.8193
C	3.3061	-2.9642	1.9075	H	-0.2486	2.9736	-2.2920
C	4.5681	-2.7832	1.3354	C	-2.2733	3.5386	-1.8528
C	4.7001	-2.0853	0.1314	H	-2.6221	3.4498	-2.8885
C	3.5876	-1.5457	-0.5245	H	-2.5108	2.6040	-1.3335
H	3.2192	-3.5139	2.8377	H	-2.8341	4.3492	-1.3710
H	5.4476	-3.1912	1.8235	C	-0.4128	5.0782	-2.6554
H	5.6857	-1.9577	-0.3003	H	-0.6987	4.9156	-3.7010
C	-2.4014	0.4387	2.2647	H	-0.9521	5.9653	-2.3020
H	-1.3940	0.5910	1.8591	H	0.6600	5.2981	-2.6248
C	-3.2059	1.7332	1.9841	C	0.7621	-2.6973	1.8754
H	-3.2817	1.9269	0.9095	H	0.1521	-1.8131	1.6485
H	-2.7183	2.5962	2.4522	C	0.0909	-3.9047	1.1713
H	-4.2225	1.6492	2.3876	H	0.0559	-3.7582	0.0871
C	-2.2583	0.2109	3.7838	H	-0.9356	-4.0372	1.5323
H	-1.7177	-0.7165	4.0029	H	0.6511	-4.8255	1.3751
H	-1.7054	1.0437	4.2333	C	0.7431	-2.8875	3.4047
H	-3.2330	0.1629	4.2837	H	-0.2933	-2.9318	3.7584
C	-2.8084	-2.4315	-1.9668	H	1.2459	-2.0618	3.9212
H	-1.7171	-2.3262	-2.0240	H	1.2281	-3.8239	3.7058

C	3.7098	-0.8202	-1.8630
H	3.0318	0.0433	-1.8327
C	3.2346	-1.7293	-3.0255
H	3.2856	-1.1862	-3.9762
H	2.2000	-2.0522	-2.8769
H	3.8714	-2.6195	-3.1009
C	5.1225	-0.2759	-2.1494
H	5.1030	0.3353	-3.0584
H	5.8447	-1.0845	-2.3165
H	5.4913	0.3488	-1.3279

Table A1f. Cartesian coordinates of **TS_{Os}** optimized by B3LYP/BS-III method.

Atomic Symbol	Coordinates (Å)		
	X	Y	Z
O	-0.0104	0.0590	-0.0081
Os	-2.0751	0.0141	0.0011
N	-2.4482	1.7432	-0.0377
N	-2.3598	-0.8281	1.5367
N	-2.4007	-0.8956	-1.4857
Os	2.0607	-0.0053	-0.0057
N	2.3772	-0.4072	1.6911
N	2.4728	1.6413	-0.5016
N	2.3287	-1.2834	-1.2086
C	-2.9447	-1.4278	2.6301
C	-3.8580	-0.6993	3.4623
C	-4.4354	-1.3698	4.5470
C	-4.1201	-2.6983	4.8412
C	-3.1996	-3.3852	4.0479
C	-2.5938	-2.7842	2.9381
H	-5.1336	-0.8376	5.1826
H	-4.5809	-3.1913	5.6924
H	-2.9457	-4.4103	4.2936
C	-3.0582	2.9796	-0.0836
C	-2.5864	4.0067	0.7990
C	-3.2033	5.2620	0.7401
C	-4.2558	5.5233	-0.1394
C	-4.7016	4.5167	-0.9979
C	-4.1209	3.2423	-1.0071
H	-2.8491	6.0486	1.3986
H	-4.7204	6.5047	-0.1600
H	-5.5152	4.7226	-1.6863
C	-2.9650	-1.5843	-2.5376
C	-3.8749	-2.6666	-2.3037
C	-4.3884	-3.3457	-3.4149
C	-4.0263	-2.9986	-4.7180
C	-3.1352	-1.9452	-4.9342
C	-2.5902	-1.2149	-3.8720
H	-5.0785	-4.1662	-3.2555
H	-4.4358	-3.5471	-5.5614
H	-2.8605	-1.6814	-5.9489
C	3.1062	2.8159	-0.8465
C	4.1180	3.3815	-0.0099
C	4.7098	4.5853	-0.4159
C	4.3233	5.2345	-1.5879
C	3.3263	4.6759	-2.3941
C	2.7034	3.4691	-2.0601
H	5.4856	5.0197	0.2067
H	4.7947	6.1698	-1.8753
H	3.0331	5.1844	-3.3050
C	2.9651	-0.7122	2.8995
C	3.8901	-1.7999	3.0118
C	4.4433	-2.0639	4.2707
C	4.1007	-1.3086	5.3938
C	3.1866	-0.2587	5.2748
C	2.6029	0.0697	4.0460
H	5.1477	-2.8815	4.3735
H	4.5413	-1.5389	6.3596
H	2.9252	0.3199	6.1530
C	2.9458	-2.1794	-2.0544
C	3.8578	-1.7242	-3.0618
C	4.4727	-2.6842	-3.8745
C	4.1929	-4.0457	-3.7406
C	3.2703	-4.4744	-2.7831

C	2.6289	-3.5725	-1.9265	H	-2.8418	0.9447	-5.6161
H	5.1725	-2.3567	-4.6353	H	-1.1471	1.5118	-5.5420
H	4.6820	-4.7685	-4.3873	H	-1.5260	-0.0336	-6.3386
H	3.0446	-5.5313	-2.6982	H	0.0752	-1.0165	-3.0013
C	-4.2121	0.7554	3.1603	H	0.0344	-1.4736	-4.7356
C	-4.5580	1.5760	4.4454	H	0.5944	0.1568	-4.2509
C	-5.3922	0.8377	2.1366	C	-4.6314	2.1945	-1.9942
H	-3.3235	1.2163	2.6846	C	-4.4000	2.6656	-3.4684
H	-3.7554	1.4986	5.1936	C	-6.1410	1.8640	-1.7509
H	-4.6908	2.6356	4.1721	H	-4.0500	1.2658	-1.8388
H	-5.5021	1.2311	4.8988	H	-3.3342	2.8820	-3.6412
H	-5.1293	0.2967	1.2138	H	-4.7230	1.8737	-4.1631
H	-6.3040	0.3908	2.5624	H	-4.9792	3.5774	-3.6849
H	-5.5887	1.8928	1.8871	H	-6.3007	1.5222	-0.7161
C	-1.5331	-3.5344	2.1343	H	-6.7726	2.7499	-1.9252
C	-1.8582	-5.0551	1.9737	H	-6.4590	1.0687	-2.4443
C	-0.1259	-3.3431	2.7969	C	-1.4174	3.7825	1.7582
H	-1.4933	-3.0774	1.1262	C	-1.8110	4.1327	3.2309
H	-2.8734	-5.2034	1.5778	C	-0.1663	4.6149	1.3178
H	-1.1364	-5.5078	1.2749	H	-1.1455	2.7099	1.7114
H	-1.7721	-5.5883	2.9350	H	-2.6838	3.5454	3.5525
H	0.1410	-2.2751	2.8225	H	-0.9658	3.9088	3.9010
H	-0.1248	-3.7340	3.8259	H	-2.0544	5.2026	3.3329
H	0.6343	-3.8856	2.2113	H	0.1335	4.3520	0.2925
C	-4.3207	-3.0266	-0.8893	H	-0.3815	5.6949	1.3551
C	-4.6578	-4.5427	-0.7155	H	0.6745	4.4026	1.9989
C	-5.5474	-2.1461	-0.4780	C	1.5653	-4.0497	-0.9390
H	-3.4855	-2.7806	-0.2047	C	1.8493	-5.4811	-0.3794
H	-3.8185	-5.1742	-1.0422	C	0.1501	-3.9911	-1.6101
H	-4.8646	-4.7446	0.3483	H	1.5588	-3.3395	-0.0887
H	-5.5578	-4.8232	-1.2877	H	2.8657	-5.5492	0.0355
H	-5.3000	-1.0780	-0.5954	H	1.1258	-5.7063	0.4209
H	-6.4175	-2.3771	-1.1116	H	1.7324	-6.2498	-1.1612
H	-5.8059	-2.3403	0.5754	H	-0.0877	-2.9563	-1.9024
C	-1.5818	-0.0955	-4.1236	H	0.1162	-4.6311	-2.5049
C	-1.7971	0.6228	-5.4951	H	-0.6118	-4.3416	-0.8948
C	-0.1199	-0.6506	-4.0216	C	4.1747	-0.2404	-3.2300
H	-1.7124	0.6523	-3.3162	C	4.3617	0.1715	-4.7268

C	5.4318	0.1585	-2.3890
H	3.3128	0.3239	-2.8276
H	3.4982	-0.1430	-5.3315
H	4.4618	1.2674	-4.7893
H	5.2749	-0.2731	-5.1559
H	5.2682	-0.0897	-1.3276
H	6.3240	-0.3797	-2.7446
H	5.6051	1.2430	-2.4780
C	1.5943	2.8780	-2.9310
C	1.6805	3.3300	-4.4241
C	0.1844	3.2129	-2.3346
H	1.7064	1.7764	-2.8996
H	2.6846	3.1499	-4.8365
H	0.9498	2.7552	-5.0161
H	1.4340	4.3989	-4.5357
H	0.0779	2.7523	-1.3395
H	0.0423	4.3012	-2.2521
H	-0.5969	2.8029	-2.9960
C	4.5767	2.7189	1.2872
C	4.3437	3.6645	2.5119
C	6.0776	2.2857	1.1999
H	3.9684	1.8072	1.4395
H	3.2831	3.9516	2.5820
H	4.6370	3.1452	3.4383
H	4.9470	4.5822	2.4220
H	6.2349	1.6098	0.3441
H	6.7338	3.1617	1.0748
H	6.3643	1.7630	2.1267
C	1.5680	1.1885	3.9321
C	1.7188	2.2779	5.0423
C	0.1200	0.5883	3.9471
H	1.7164	1.6754	2.9468
H	2.7496	2.6587	5.0897
H	1.0440	3.1191	4.8146
H	1.4372	1.8829	6.0324
H	-0.0243	-0.0681	3.0749
H	-0.0520	0.0105	4.8679
H	-0.6162	1.4071	3.8984
C	4.3031	-2.6079	1.7849
C	4.6433	-4.0972	2.1144
C	5.5099	-1.9168	1.0675
H	3.4478	-2.5999	1.0819
H	3.8179	-4.5793	2.6588
H	4.8167	-4.6428	1.1724
H	5.5622	-4.1762	2.7187
H	5.2557	-0.8706	0.8284
H	6.4003	-1.9236	1.7150
H	5.7389	-2.4515	0.1317

Table A2. Electronic energies (E_h) of Ir and Os model and real systems in singlet (S_0) and triplet (T_1) states.[a), b)]

	Ir system				Os system			
	Model system		Real system		Model system		Real system	
	$Ir(CH_3)_3$	**$Ir(CH_3)_3$=O**	**$Ir(Mes)_3$**	**$Ir(Mes)_3$=O**	**$Os(NCH_3)_3$**	**$Os(NCH_3)_3$=O**	**$Os(NAr)_3$**	**$Os(NAr)_3$=O**
S_0	-224.0968	-299.3150	-1153.0753	-1228.2755	-374.7009	-449.8937	-1657.4194	-1732.6131
T_1	-224.0452	-299.2838	-1153.0353	-1228.2383	-374.7007	-449.8530	-1657.3649	-1732.5806
$\Delta E[T_1-S_0]$ (kcal/mol)	32.38	19.58	25.10	23.34	0.13	25.54	34.20	20.39

a) geometries are optimized in each spin state. model systems

b) computational method and basis sets; B3LYP/BS-II//B3LYP/BS-I for model systems, and B3LYP/BS-IV//B3LYP-BS-III for real systems.

Table A3. Calculated Ir=O and Os=O bond energies (kcal/mol) in **$Ir(CH_3)_3$=O** and **$Os(NCH_3)_3$=O** complexes[a)].

		Ir=O	Os=O	Δ[(Ir=O)-(Os=O)]
Theoretical	B3LYP	93.20	78.31	14.89
	MP2	113.48	101.78	11.70
	MP3	70.02	40.84	29.18
	MP4(SDQ)	94.67	66.83	27.84
	CCSD	80.98	55.10	25.88
	CCSD(T)	91.17	70.98	20.19
	B3LYP [2]	-	-	17.7
Experimental	Ref. 1[b)]	99.1±10.1	-	
	Ref. 2	-	-	-0.86

a) geometries of **$Ir(CH_3)_3$**, **$Ir(CH_3)_3$=O**, **$Os(NCH_3)_3$**, and **$Os(NCH_3)_3$=O** are optimized at B3LYP/BS-I, and bond energies are calculated by BS-II.

b) dissociation energy for gaseous iridium monoxide

(1) Pedley, J. B.; Marshell, E. M.; *J. Phys. Chem. Ref. Data*, **1984**, 12, 967.

(2) Fortner, K. C.; Laitar, D. S.; Muldoon, J.; Pu, L. H.; Braun-Sand, S. B.; Wiest, O.; Brown, S. N. *J. Am. Chem. Soc*. **2007**, 129, 588.

Table A4 Calculated vertical and adiabatic ionization energy and electron affinity for iridium and osmium model systems.[a)]

	Ionization energy (eV)		Electron affinity (eV)	
	Vertical	Adiabatic	Vertical	Adiabatic
$Ir(CH_3)_3$	7.43	7.37	-	-
$Ir(CH_3)_3$=O	-	-	0.32	1.03
$Os(NCH_3)_3$	7.70	7.67	-	-
$Os(NCH_3)_3$=O	-	-	0.08	1.02

a) geometries of neutral, cation, anion species are all optimized at B3LYP/BS-I level, and ionization energy and electron affinity are calculated by CCSD(T)/BS-II level.

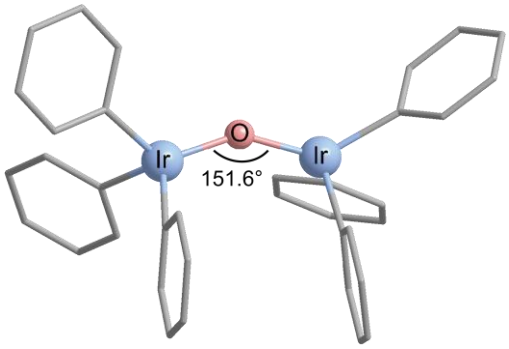

Figure A1. Optimized geometry for the μ-oxo dinuclear complex of the oxygen atom transfer reaction of **$Ir(Ph)_3$** and **$Ir(Ph)_3$=O** (B3LYP/BS-I, hydrogen atoms are omitted)

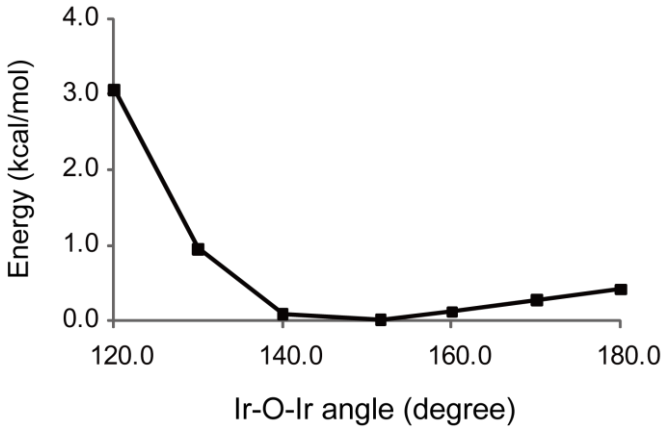

Figure A2. Potential energy curves against the Ir-O-Ir angle in **$Ir(Ph)_3$-O-$Ir(Ph)_3$** calculated by B3LYP/BS-I method.

Chapter 2

Pd(II)-promoted Direct Cross-Coupling Reaction of Arenes via Highly Regioselective Aromatic C-H Activation: A Theoretical Study

Abstract

The direct cross-coupling reaction of arenes promoted by $Pd(OAc)_2$ is synthetically very useful because the preparation of haloarene as substrate is not necessary. This reaction occurs only in the presence of benzoquinone (BQ), interestingly. DFT, MP2 to MP4(SDQ), and CCSD(T) computations elucidated the whole mechanism of this cross-coupling reaction and the key roles of BQ. The first step is the heterolytic C-H activation of benzo[*h*]quinoline (HBzq) by $Pd(OAc)_2$ to afford Pd(Bzq)(OAc). The Pd center is more electron-rich in Pd(Bzq)(OAc) than in $Pd(OAc)_2$. Hence, BQ easily coordinates to Pd(Bzq)(OAc) with low activation barrier to afford a distorted square planar complex Pd(Bzq)(OAc)(BQ) which is as stable as Pd(Bzq)(OAc). Then, the second C-H activation of benzene occurs with moderate activation barrier and small endothermicity. The final step is the reductive elimination which occurs with little barrier. The rate-determining step of the overall reaction is the second C-H activation whose activation barrier is considerably higher than that of the first C-H activation. BQ plays key roles to accelerate this reaction, as follows: (i) The phenyl group must change its position very much to reach the transition state in the reductive elimination from the square planar intermediate Pd(Ph)(Bzq)(OAc) but moderately in the reaction from the trigonal bipyramidal intermediate Pd(Ph)(Bzq)(OAc)(BQ). This is because BQ suppresses the phenyl group to take a position distant from the Bzq. And, (ii) BQ stabilizes the transition state and the product complex by the back-donation interaction. In the absence of BQ, the reductive elimination step needs much higher activation barrier. Though it was expected that the BQ coordination accelerates the second C-H activation of benzene by decreasing the electron density of Pd in Pd(Bzq)(OAc), the activation barrier of this second C-H activation is little influenced by BQ.

2.1 Introduction

In organometallic chemistry, the C-C bond formation reaction catalyzed by transition metal complex is one of the most important research subjects.[1-12] The metal-catalyzed cross-coupling reaction is widely employed for the C-C bond formation such as the Stille coupling reaction[13] and the Suzuki-Miyaura coupling reaction.[14] High selectivity,[15] functional group tolerance, and use of the mild reaction conditions make these processes sensible choice for the C-C bond formation even in the complicated synthesis of natural product.[16]

However, the preparation of organic bromide or organic iodide as coupling partners is necessary in many metal-catalyzed cross-coupling reactions. This requires the preparation step of such organic halides from hydrocarbons. Moreover, the use of organic halide often leads to the formation of side products that are toxic and also difficult to remove from the main product. These are undesirable from both points of view of efficiency and environmentally-friendly reaction. Thus, the direct cross-coupling with non-halogenated substrate is highly desirable, as reported in recent pioneering works.[17-20] However, such cross-coupling reaction needs the C-H σ-bond activation which is difficult process unlike the C-X (X = Br or I) bond activation because the C-H σ-bond is much stronger than the C-X bond.

It is expected that the above-mentioned difficulty in the direct cross-coupling reaction can be overcome by using appropriate transition metal catalyst and additives. Actually, recent experimental works reported that Pd(II) complexes catalyze various homo-coupling of arenes under mild conditions.[21-23] However, reports of cross-coupling (hetero-coupling) of arenes have been rather limited,[24-27] though such cross-coupling is synthetically very useful. Another key point of the direct cross-coupling reaction is regioselectivity, because the *ortho*-, *meta*-, and *para*-substituted arenes are often formed as side-product which is difficult to separate from each other. The key point for the high regioselectivity is to activate regioselectively the

C-H bond of arene which is also difficult process. For this purpose, the widely used strategy is to employ the ligand-directed C-H activation.[28] This is achieved by the coordination of heteroatom such as nitrogen or oxygen to the metal center. Several theoretical studies of the detailed mechanism have been reported.[29]

Recently, Sanford *et. al.* reported the novel cross-coupling reaction of arenes catalyzed by Pd(II) salt (eq. 1a and 1b).[30]

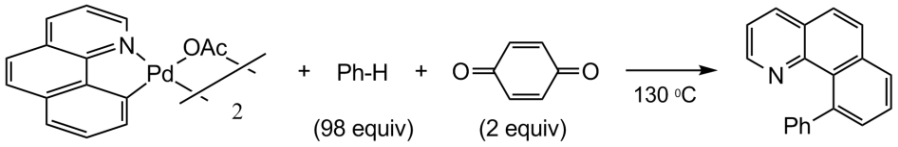

(1a)

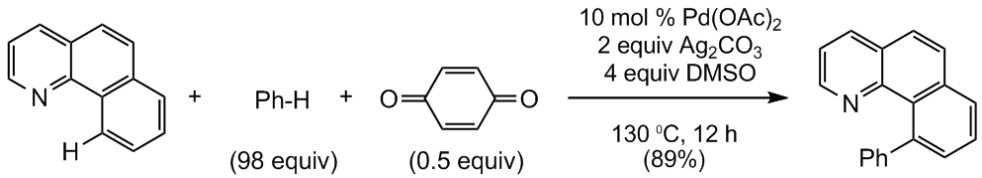

(1b)

The reaction (1a) is stoichiometric in Pd, but it becomes catalytic reaction (1b) by the addition of Ag(I) salt. In both reactions, two separate C-H activations occur with high regioselectivity. The cross-coupling product is 10-phenylbenzo[*h*]quinoline. Interestingly, this compound is produced only when 2 equivalents of benzoquinone (BQ) are added to the reaction system. These results indicate that BQ plays important roles in the arene cross-coupling reaction. Sanford and coworkers proposed that BQ binds with an initially formed palladium intermediate and promotes the C-H activation of arenes.[31, 32] This proposal is further supported by experimental results that the use of the methyl-substituted BQ dramatically suppresses the cross-coupling at the *ortho*-position of anisole but increases the cross-coupling at the *meta*- and *para*-positions. These results suggest that BQ coordinates with the Pd center during the arene C-H activation to play important roles not only for reactivity but also for regioselectivity.[30]

It is of considerable importance to clarify the roles of BQ because such knowledge provides the idea how to achieve the regiocontrol of C-H activation through steric and

electronic modifications of an ancillary ligand. To reach the goal of regioselective cross-coupling reaction of arenes, the correct knowledge on the reaction mechanism is also indispensable. However, there are many unclear issues on the reaction mechanism of this arene cross-coupling reaction. For example, though the coordination of BQ with the Pd center is suggested, neither experimental nor theoretical evidence has been presented. Also, it is still unclear how and why the coordination of BQ leads to highly regioselective C-H activation of arene.

Because of the importance of the C-H activation reaction, many theoretical works on this reaction have been carried out.[33-53] For instance, Sakaki *et. al.*[52] successfully disclosed that the C-H activation of benzene by $Pd(O_2CH)_2$ occurs through "heterolytic type C-H activation" (eq 2) unlike "C-H activation by oxidative addition" (eq 3).[52]

$$MXL_n + R\text{-}H \rightarrow MRL_n + HX \qquad (R = \text{alkyl or aryl; } X = \text{an anionic ligand}) \qquad (2)$$

$$ML_n + R\text{-}H \rightarrow M(R)(H)L_n \qquad (3)$$

This heterolytic C-H activation mechanism is also studied experimentally and understood as "proton abstraction mechanism".[54, 55]

In this work, we wish to report the theoretical investigation of the stoichiometric arene cross-coupling reaction between HBzq and benzene promoted by $Pd(OAc)_2$ (eq. (1a)). Our purposes here are (i) to clarify the characteristic feature of the transition states and the important intermediates such as the Pd(II)-BQ complex, (ii) to present the energy changes of the entire catalytic process, and (iii) to elucidate the reason why this cross-coupling reaction regioselectively occurs in the presence of BQ but does not in the absence of BQ.

2.2 Computational Details

Geometry optimization was carried out with the DFT method using B3PW91 functional.[56-58] Frequency analysis was made with the same method. Möller-Plesset perturbation theory (MP2 to MP4(SDQ)) was used for evaluation of energy changes. Energy changes were also evaluated with the ONIOM method in which the CCSD(T) method was employed for the higher level calculation of the important moiety and the MP2 method was employed for the lower level calculation.

Two basis set systems (BS-I and BS-II) were employed for calculations; In BS-I, Los Alamos effective core potentials (ECPs) were used to replace core electrons of Pd and (341/321/31) basis set was used to represent its valence electrons.[59] Usual 6-31G(d) basis sets[60] were used for carbon, nitrogen, oxygen, and hydrogen atoms. In BS-II, Stuttgart-Dresden-Bonn ECPs were used to replace the core electrons of Pd and (8881/7771/661/1) basis set was used for the valence electrons.[61] Dunning cc-pVDZ basis sets[62] were used for carbon, nitrogen, oxygen, and hydrogen atoms. The BS-I was used for geometry optimization and frequency calculation, and the BS-II was used for evaluation of energy changes. Zero-point energy was evaluated with the DFT/BS-I method under assumption of harmonic oscillator. Solvation effects of benzene were evaluated with PCM method,[63] where the geometries were re-optimized in solution with the PCM method at the DFT/BS-I level. Free energies are evaluated at 25 °C according to the method of Whiteside.[64] Natural population analysis (NPA) is performed with the B3PW91/BS-II method.
All calculations were performed with Gaussian 03 program package.[65] NBO analysis is performed with NBO program 3.1.[66]

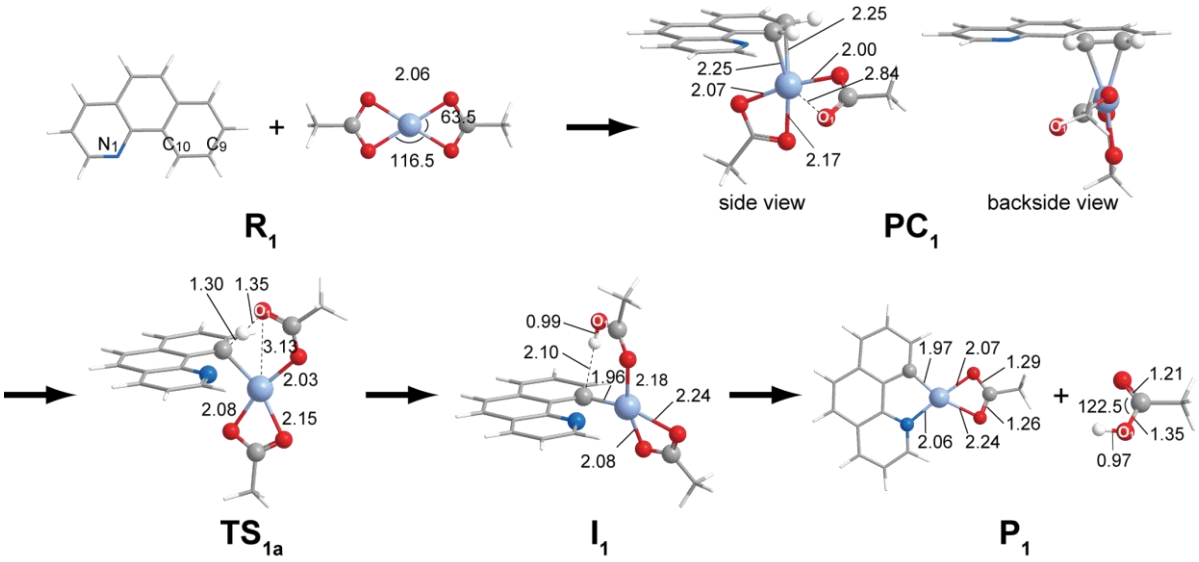

Fig. 1. Geometry changes in the C-H activation of HBzq by $Pd(OAc)_2$. Bond lengths are in Å and bond angle are in degrees

2.3 Results and Discussions

2.3.1 The C-H activation of HBzq

The cross-coupling reaction of HBzq and benzene occurs through two separate C-H activation processes; one is the C-H activation of HBzq and the other is that of benzene. For brevity, the OAc ligand that changes to acetic acid (HOAc) in the first C-H activation is named OAc^1, and the other one is OAc^2.

The C-H activation of HBzq by $Pd(\eta^2\text{-}OAc)_2$ occurs through precursor complex (**PC_1**), transition state (**TS_1**) to afford intermediate $Pd(Bzq)(\eta^2\text{-}OAc)(HOAc)$ (**I_1**), as shown in Fig. 1. Geometrical features of these species are summarized, as follows: First, HBzq approaches the Pd complex to form **PC_1**. In **PC_1**, the C^9-C^{10} double bond of HBzq coordinates to the Pd center in η^2-coordination way. The optimized Pd-C^9 and Pd-C^{10} distances (2.25 Å) agree well with the experimental Pd-C distance of palladium-arene complexes (2.22 - 2.61 Å).[67] Another important geometrical change induced by the HBzq coordination is significantly large elongation of the Pd-OAc^1 bond (2.84 Å), indicating that the OAc^1 ligand changes to

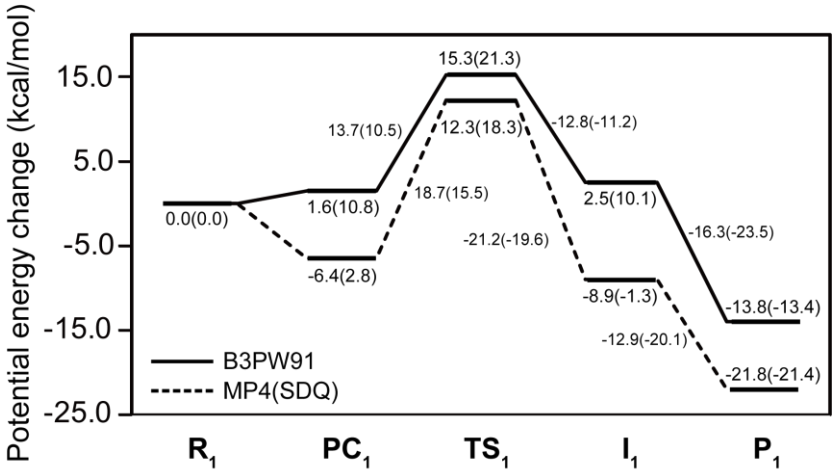

Fig. 2. Potential energy changes for the C-H activation of HBzq by $Pd(OAc)_2$ in benzene. Energies [a)] are given in kcal/mol unit. [a)] In parentheses are Gibbs free energy changes.

η^1-coordination form from an η^2-coordination one; see Fig. 1. On the other hand, two Pd-O distances of OAc^2 little change. In other words, **PC_1** is represented as $Pd(\eta^1\text{-}OAc^1)(\eta^2\text{-}OAc^2)$(HBzq). This is because the η^2-OAc ligand must change to the η^1-OAc ligand to supply one coordination site to HBzq. When going to **TS_1** from **PC_1**, the C-H bond of HBzq starts to be elongated. In **TS_1**, one imaginary frequency (913.4i cm^{-1}) is observed, in which the H atom bound with the C^{10} atom is moving toward the O atom of OAc^1. This transition state is essentially the same as that of the C-H activation of benzene by $Pd(\eta^2\text{-}O_2CH)_2$.[52] After this transition state, the Pd-Ph bond and acetic acid ($H\text{-}OAc^1$) are formed in **I_1** as a result of heterolytic C-H activation by the Pd-OAc moiety. This acetic acid still interacts with the Pd center, as shown by the Pd-O bond distance (2.18Å) which is normal coordination bond distance. Essentially the same coordination of formic acid was reported in the C-H activation of benzene by $Pd(\eta^2\text{-}O_2CH)_2$.[52] After that, the acetic acid dissociates from the Pd center to afford the product **P_1**. **P_1** takes square planar geometry coordinated by Bzq and OAc^2.

Potential and Gibbs energy changes are evaluated by the DFT/BS-II and MP4(SDQ)/BS-II methods; see Fig. 2 for their values in benzene and see Fig. A1 for their

values in gas phase. In this C-H activation step, the activation barrier (E_a) and the activation Gibbs energy change ($\Delta G^{0‡}$) are defined as the energy difference between **PC$_1$** and **TS$_1$**. The E_a value of this step in benzene is calculated to be 13.7 and 18.7 kcal/mol by the DFT and MP4(SDQ) methods, respectively, where the solvation effects of benzene are evaluated with the PCM method hereafter. The $\Delta G^{0‡}$ value in benzene is evaluated to be 10.5 and 15.5 kcal/mol by the DFT and MP4(SDQ) methods, respectively. The DFT method somewhat underestimates the E_a and $\Delta G^{0‡}$ values. These DFT- and MP4(SDQ)-calculated E_a values are similar to those of the C-H activation of benzene by Pd(η^2-$O_2CH)_2$ which are calculated to be 9.9 and 15.7 kcal/mol by the DFT(B3LYP) and MP4(SDQ) methods, respectively.[52] The MP4(SDQ)-calculated ΔE and ΔG^0 values are considerably negative, as shown in Fig. 2, where ΔE and ΔG^0 are defined as energy difference between the reactant (**R$_1$**) and the product (**P$_1$**) of this step. From these ΔE, E_a, ΔG^0, and $\Delta G^{0‡}$ values, it is concluded that the C-H activation of HBzq easily occurs at experimental temperature (130 ˚C).

Because the CCSD(T) method could not be applied to our system due to the large size, we employed the ONIOM method here.[68] In the ONIOM calculation, the whole system is divided into the important moiety and the remaining moiety, which are calculated with CCSD(T) and MP2 methods, respectively; see Scheme A1. We found that ONIOM-calculated E_a value is essentially the same as the MP4(SDQ)-calculated value; see Fig. A5 and Table A1. From these results, we will present our discussion based on the MP4(SDQ)/BS-II computational results. The previous theoretical study by Sakaki and coworkers reported the similar results that the activation barrier converges when going from MP2 to MP4(SDQ) and the MP4(SDQ)-calculated E_a value is almost the same as the CCSD(T)-calculated value.[52]

To understand this C-H activation process in more details, changes in electron distribution were investigated by natural population analysis (NPA). As shown in Fig. 3, the electron population of HBzq moderately decreases as a result of the HBzq coordination with Pd(η^2-$OAc)_2$, when going to **PC$_1$** from **R$_1$**. However, the Pd atomic population decreases,

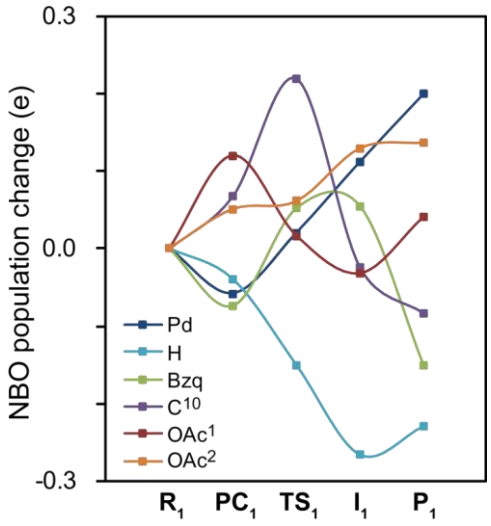

Fig. 3. Population changes [a] for the C-H activation of HBzq by $Pd(OAc)_2$. A positive value represents increase in population relative to $\mathbf{R_1}$, and vice versa. [a] DFT/BS-II level was employed

unexpectedly. On the other hand, the electron population of the OAc^1 ligand increases. These results indicate that the CT (charge transfer) from the OAc^1 ligand to the Pd center becomes weaker when going to $\mathbf{PC_1}$ from $\mathbf{R_1}$. This is because one of the O atoms of OAc^1 dissociates from the Pd center by the HBzq coordination; see above. In $\mathbf{TS_1}$, the H atomic population considerably decreases but that of the C^{10} atom in the Bzq moiety considerably increases. These features suggest that the polarization of the C^{10}-H bond occurs when going to $\mathbf{TS_1}$ from $\mathbf{PC_1}$; in other words, the H atom becomes positively charged but the C^{10} becomes negatively charged in $\mathbf{TS_1}$. In $\mathbf{I_1}$, the C^{10} atomic population considerably decreases, while the Pd atomic population increases. This clearly shows that the CT from the C^{10} atom to the Pd center considerably occurs to form a new Pd-C^{10} bond.

The polarization changes by the oxidative addition, which were reported in the C-H activations of methane and benzene by $Pt(PH)_3$,[35, 52, 53] are completely different from the above-discussed population changes. These results indicate that the C-H activation occurs in a heterolytic manner, which are interpreted in the same way as that of the theoretical study of the C-H activation of alkane by $(Me_3SiO)_2Ti(=NSiMe_3)$[53]: i) The mixing between the C-H σ- and σ*-type MOs (molecular orbitals) induces the polarization of the C-H bond to be broken.

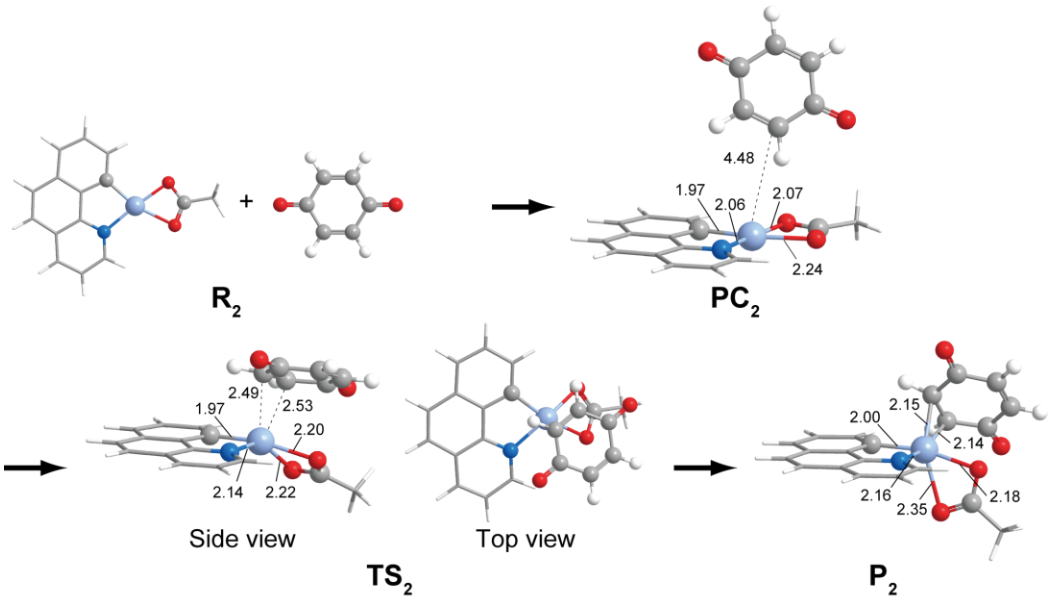

Fig. 4. Geometry changes in the BQ coordination to Pd(Bzq)(OAc). Bond lengths are in Å and bond angle are in degrees.

As a result, the C^{10} atom of the Bzq group becomes negatively charged and the H atom becomes positively charged. ii) The CT from the negatively charged C^{10} atom to the Pd center stabilizes **TS_1** and contributes to the formation of the new Pd-C^{10} bond. Also, the electrostatic stabilization between the negatively charged C^{10} atom and the positively charged Pd center contributes to the stabilization of TS.

2.3.2 Benzoquinone coordination

As discussed above, the C-H activation of HBzq easily occurs from both kinetically and thermodynamically. Because the product Pd(Bzq)(η^2-OAc) **P_1** of the first C-H activation still has one OAc ligand, another C-H activation is possible.

According to the experimental findings,[14] the arene cross-coupling occurs when BQ is added to the reaction system. Although it is proposed that BQ accelerates the RE (reductive elimination) step,[69, 70] the role of BQ in the C-H activation process is unclear. Here, we investigated if BQ coordinates with Pd(Bzq)(η^2-OAc) as experimentally proposed.[14]

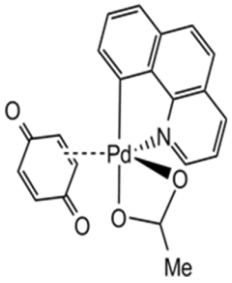

Scheme 1

We carried out geometry optimization of Pd(Bzq)(η^2-OAc)(BQ) (**P_2**), as shown in Fig. 4. Frequency analysis showed that **P_2** exists as stable species in energy minimum. This coordination of BQ occurs via precursor complex (**PC_2**) and transition state (**TS_2**); see Fig. 4. In **P_2**, one Pd-O bond (2.35 Å) is somewhat longer than the other one (2.18 Å). But, even the longer Pd-O distance is close to the usual Pd-O coordinate bond distance. This suggests that the two Pd-O coordinate bonds are kept and the OAc forms distorted η^2-coordinate bond unlike **PC_1** which contains the η^1-OAc. Because of the presence of BQ, the geometry of **P_2** is trigonal bipyramidal in which the Pd-C[10] and the shorter Pd-O bonds are in the axial position, as shown in Scheme 1 and Fig. 4.

Potential and Gibbs energy changes in toluene were evaluated by the DFT and MP4(SDQ) methods, as shown in Fig. 5; for their values in gas phase, see Fig. A2. In the BQ coordination step, the ΔE and ΔG^0 values are defined as the energy difference between **R_2** and **P_2**, and the E_a and $\Delta G^{0\ddagger}$ values are defined as the energy difference between **PC_2** and **TS_2**. The E_a and ΔE values in toluene are calculated to be 6.7 and -13.2 kcal/mol, respectively, with the MP4(SDQ) method. The $\Delta G^{0\ddagger}$ and ΔG^0 values are calculated to be 8.7 and -1.7 kcal/mol, respectively, with the MP4(SDQ) method. These results indicate that BQ easily coordinates with the Pd complex. However, the DFT method considerably overestimates the $\Delta G^{0\ddagger}$ and ΔG^0 values. This is because the DFT method considerably underestimates the stabilization energy by the BQ coordination. We found the similar result that the DFT method

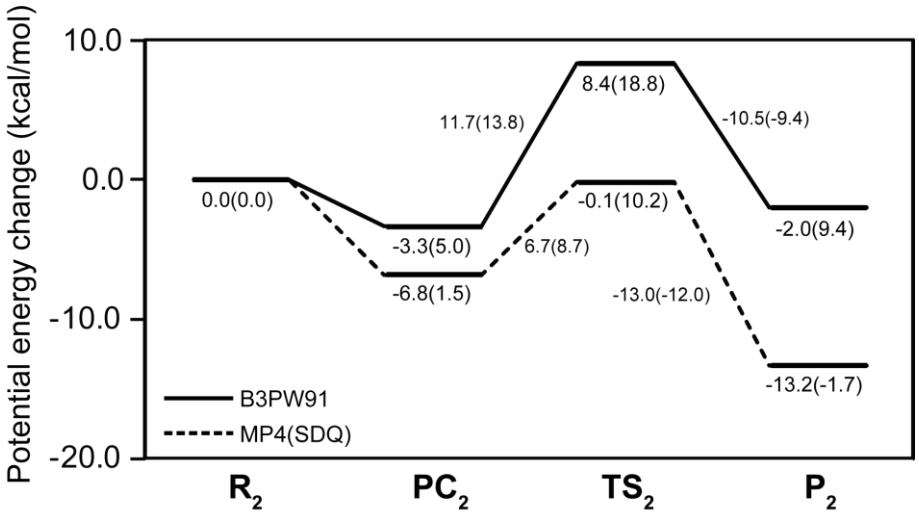

Fig. 5. Potential energy changes for the BQ coordination to Pd(Bzq)(OAc) in benzene. Energies [a)] are given in kcal/mol unit. [a)] In parentheses are Gibbs free energy changes

underestimates the binding energy of π-conjugate molecules with Pt and Pd complexes.[71]

The electron distribution changes by the BQ coordination are shown in Fig. 6. Since BQ is electron-deficient, the Pd atomic population decreases and the electron population of the BQ increases by the BQ coordination. However, the electron populations of the Bzq and the OAc change less than those of the BQ and the Pd. These results indicate that the BQ

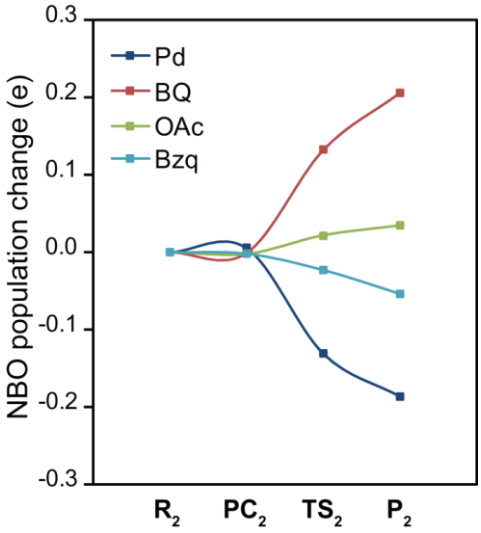

Fig. 6. Population changes [a)] for the BQ coordination to Pd(Bzq)(OAc). A positive value represents increase in population relative to **R_2**, and vice versa. [a)] DFT/BS-II level was employed

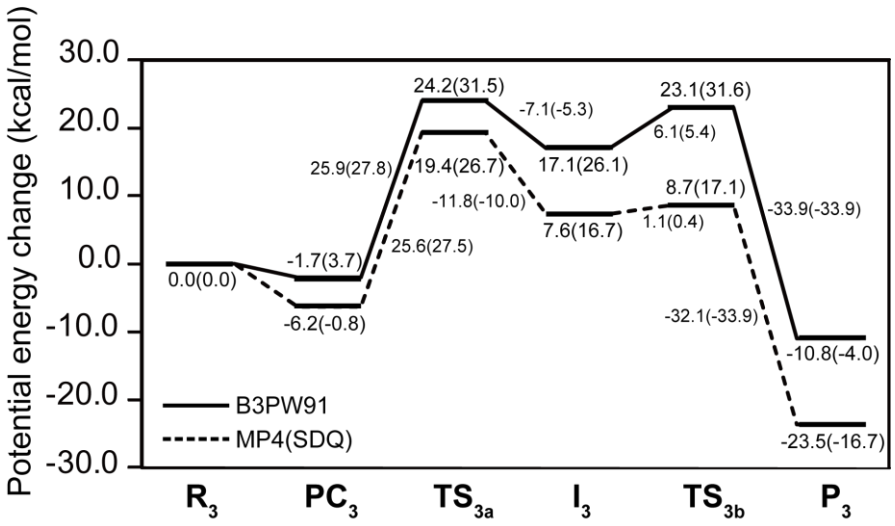

Fig. 8. Potential energy changes for the C-H activation of benzene by Pd(Bzq)(OAc)(BQ) in benzene. Energies [a)] are given in kcal/mol unit. [a)] In parentheses are Gibbs free energy changes.

coordination mainly induces electron re-distribution between the BQ and the Pd. In Pd(Bzq)(η^2-OAc) **P_1** which is the product of the first C-H activation, the CT from the Bzq to the Pd occurs. As a result, the Pd atomic population increases by 0.20 e when going to **P_1** from Pd(η^2-OAc)$_2$. This increase in the Pd atomic population would be unfavorable for the second C-H activation, because the metal center should be electophilic for this type of C-H activation. Thus, it is expected that the BQ coordination is necessary for the second C-H activation process because the Pd atomic population decreases by the BQ coordination. This expectation will be investigated below in detail.

2.3.3 Second C-H activation and RE (Reductive Elimination) step

In this section, we investigated the reaction between benzene and Pd(Bzq)(OAc)(BQ) **P_2** which is the product of the first C-H activation.

As shown in Fig. 7, benzene approaches **P_2** at the opposite side of the BQ moiety to form precursor complex Pd(Bzq)(OAc)(BQ)(C_6H_6) **PC_3**. In **PC_3**, the Pd-benzene interaction is weaker than the Pd-HBzq interaction of **PC_1** formed in the first C-H activation step, as

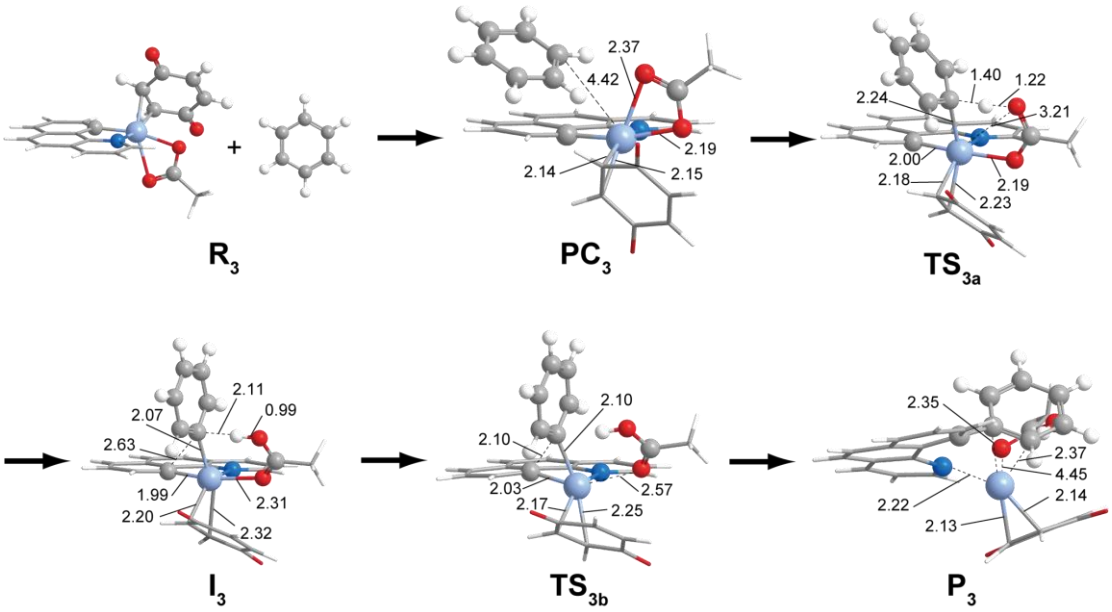

Fig. 7. Geometry changes in the C-H activation of benzene by Pd(Bzq)(OAc)(BQ) and the successive reductive elimination of Bzq-Ph. Bond lengths are in Å and bond angle are in degrees.

indicated by the much longer Pd-C distance (4.42 Å); remember the Pd-C distance (2.25 Å) in **PC$_1$**. The C-H activation occurs through transition state **TS$_{3a}$** to afford intermediate Pd(Ph)(Bzq)(HOAc)(BQ) **I$_3$**. In **TS$_{3a}$**, the C-H bond of benzene is considerably elongated to 1.40 Å. Simultaneously, one Pd-O bond is considerably elongated to 3.21 Å, indicating that the η^2-OAc forms turns into the η^1-OAc form. In **I$_3$**, acetic acid is formed like the first C-H activation of HBzq, as shown in the optimized geometry of **I$_3$**. The Pd-O distance of 2.31 Å indicates that the acetic acid coordinates to the Pd center. The Pd-Ph bond is formed at the axial position, the bond distance (2.07 Å) of which is moderately longer than the Pd-Bzq bond (1.99 Å).

Starting from Pd(Bzq)(Ph)(HOAc)(BQ) **I$_3$**, the RE occurs through transition state **TS$_{3b}$** to afford product Pd(Bzq-Ph)(BQ)(HOAc) **P$_3$** (Bzq-Ph = 10-phenylbenzo[h]quinoline). In **TS$_{3b}$**, the C-C bond distance (2.10 Å) between Bzq and Ph becomes considerably shorter than that of **I$_3$** (2.63 Å). Another change to be noted is that the distance between the Pd atom and the O atom of OAc becomes considerably longer when going to **TS$_{3b}$** (2.57 Å) from **I$_3$** (2.31

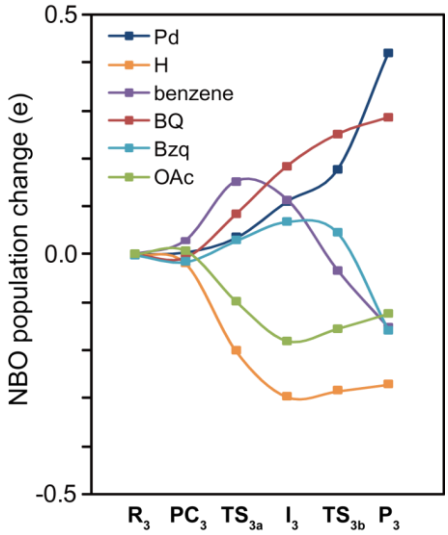

Fig. 9. Population changes [a)] for the C-H activation of benzene by Pd(Bzq)(OAc)(BQ). A positive value represents increase in population relative to **R$_3$**, and vice versa. [a)] DFT/BS-II level was employed.

Å). This indicates that the CT from the OAc ligand to the Pd center becomes weaker in **TS$_{3b}$**, because Pd(II) changes to Pd(0) in the RE step. In **P$_3$**, three important interactions are observed; i) Bzq-Ph coordinates with the Pd center through the phenyl moiety, ii) BQ coordinates with the Pd center in an η^2-coordination way, and iii) HOAc weekly interacts with the Pd center through one O atom. Interestingly, the Pd-BQ interaction becomes stronger as indicated by the shorter Pd-C distances in **P$_3$** than in **TS$_{3b}$**. This is because the Pd center becomes more electron-rich after the RE; remember that BQ tends to form back-donation interaction with the Pd center because BQ is electron-deficient.

Potential and Gibbs energies are shown in Fig. 8; see Fig. A3 for these values in gas phase. The E_a and $\Delta G^{0‡}$ values of the second C-H activation are calculated to be 25.6 and 27.5 kcal/mol with the MP4(SDQ) method, where these values are defined as the energy difference between **PC$_3$** and **TS$_{3a}$**. Though these E_a and $\Delta G^{0‡}$ values are considerably larger than those of the first C-H activation of HBzq, these values are still moderate, indicating that the second C-H activation thermally occurs. If we concentrate on the RE after **I$_3$**, the E_a and $\Delta G^{0‡}$ values are calculated to be 1.1 and 0.4 kcal/mol, respectively, with the MP4(SDQ) method. These

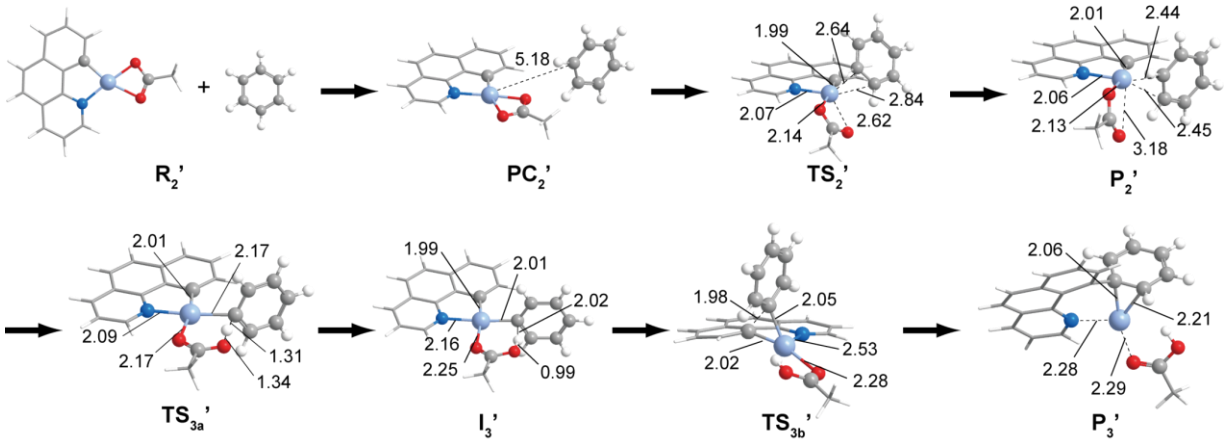

Fig. 10. Geometry changes in the C-H activation of benzene by Pd(Bzq)(OAc) in the absence of BQ. Bond lengths are in Å and bond angle are in degrees.

values clearly indicate that the RE easily occurs with little barrier.

Compared to the MP4(SDQ) method, the DFT method tends to overestimate the E_a value. However, the difference is moderate. On the other hand, the ΔE value is much different between these two methods, where the ΔE is defined as the potential energy difference between $\mathbf{R_3}$ and $\mathbf{P_3}$; the ΔE is calculated to be -10.8 kcal/mol by the DFT method and -23.5 kcal/mol by the MP4(SDQ) method; see Fig. 8. This is because the DFT method underestimates the stabilization energy by the BQ coordination compared with the MP4(SDQ) method, as discussed in the previous section and ref. 70.

When going to $\mathbf{P_3}$ from $\mathbf{R_3}$, the Pd atomic population considerably increases and the H atomic population considerably decreases, as shown in Fig. 9. Also, the electron population of the phenyl group considerably increases. These results are basically the same as those of the first C-H activation. Thus, the second C-H activation is understood to be heterolytic like the first C-H activation. In the RE, the Pd atomic population considerably increases expectedly, as shown in Fig. 9. Another important feature is that the electron population of the BQ increases when going to $\mathbf{P_3}$ from $\mathbf{I_3}$. This is because the Pd center changes into the Pd(0) in the RE and the BQ receives d electrons of Pd though the back-donation from the Pd to the BQ to stabilize

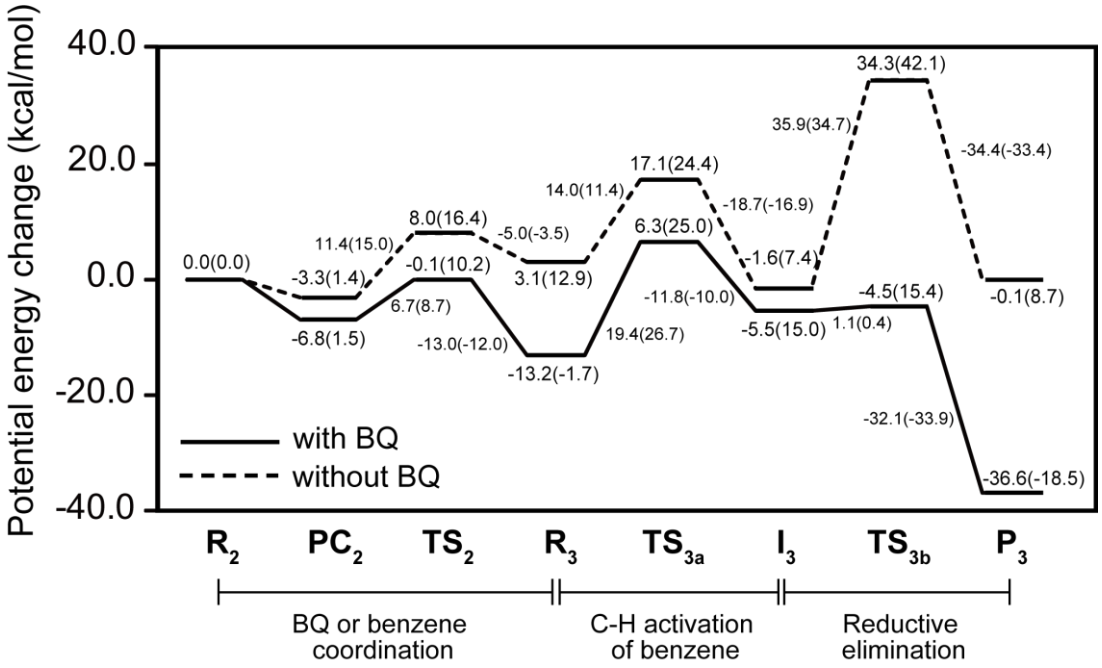

Fig. 11. Potential energy changes for the BQ or benzene coordination, the C-H activation of benzene, and the reductive elimination of Bzq-Ph, in the presence and absence of BQ in benzene. Energies [a)] are given in kcal/mol unit. [a)] In parentheses are Gibbs free energy changes.

TS_{3b} and **P_3**. This reflects in the shortening of the Pd-BQ distance when going to **P_3** from **I_3**.

2.3.4 What role does benzoquinone (BQ) play in this cross-coupling reaction?

As discussed above, the $\Delta G^{0\ddagger}$ for the BQ coordination is small and the ΔG^0 value is negative, indicating that BQ easily coordinates with Pd(η^2-OAc)(Bzq). In this BQ coordination step, the η^2-OAc ligand changes into the η^1-OAc form to produce a new coordination site for BQ. The η^1-OAc form is also favorable for the second C-H activation because η^1-OAc has a free O atom which easily abstracts the H atom of benzene. In addition to this geometrical feature, it is expected that the BQ coordination facilitates the second C-H activation from the viewpoint of electronic structure, as mentioned above.

To understand the roles of BQ, the second C-H activation and the RE steps are

investigated here without BQ. First, the coordination of benzene with the product, Pd(Bzq)(η^2-OAc) **R_2**, of the first C-H activation is examined. Like the BQ coordination with **P_2**, the coordination of benzene occurs through precursor complex (**PC_2'**) and transition state (**TS_2'**) to afford benzene complex Pd(Bzq)(η^2-OAc)(C_6H_6) **P_2'**; see Fig. 10 for their optimized geometries. **P_2'** is square planar four-coordinate complex, as shown in Fig. 10. The largest difference between **P_2** and **P_2'** is found in the geometry; **P_2** is pseudo-trigonal bipyramidal, in which the N-Pd-O is the pseudo C_3 axis and BQ takes the equatorial position. On the other hand, benzene first approaches the Pd center from the axial direction but finally coordinates to the Pd center at the in-plane position of the square planar **P_2'**; see Figs. 7 and 10.

Starting from **P_2'**, the C-H activation of benzene occurs through transition state (**TS_{3a}'**) to afford intermediate Pd(Bzq)(Ph)(HOAc) **I_3'**; see Fig. 10 for their optimized geometries. In **TS_{3a}'**, the C-H bond of benzene is considerably elongated (1.31 Å) compared to that of **P_2'** (1.09 Å). The structure of **I_3'** is significantly different from that of **I_3** which is formed in the presence of BQ; For instance, **I_3'** is square planar but **I_3** is trigonal bipyramidal, through the Pd(II) center takes d^8 electron configuration in both. This difference arises from the presence of BQ in **I_3**; Because BQ tends to form π-back donation interaction, it tends to stabilize the trigonal bipyramidal structure by taking an equatorial position.[71] As a result, **I_3** is trigonal bipyramidal because of the presence of BQ, but **I_3'** is square planar because of the absence of BQ.

Potential and Gibbs energy changes in the presence and absence of BQ are shown in Fig. 11; see Fig. A4 for their values in gas phase. The E_a and $\Delta G^{0‡}$ values for the C-H activation of benzene are calculated to be 17.1 and 24.4 kcal/mol, respectively, by the MP4(SDQ) method, where the E_a and $\Delta G^{0‡}$ values are defined as the energy difference between **TS_{3a}'** and **R_2** because **R_3** is less stable than **R_2**. This $\Delta G^{0‡}$ value is almost the same as that (26.7 kcal/mol) of the second C-H activation process in the presence of BQ. The ΔG^0 value of **I_3'** relative to **R_2** is moderate (7.4 kcal/mol). These computational results suggest that

the C-H activation of benzene can occur even in the absence of BQ and that the BQ coordination little accelerates the second C-H activation against our expectation.

After the formation of **I_3'**, the RE occurs to complete the catalytic reaction. The non-planar transition state (**TS_{3b}'**) is optimized, as shown in Fig. 10. The $\Delta G^{0‡}$ value is calculated to be 34.7 kcal/mol by the MP4(SDQ)/BS-II method, which is much larger than that of the second C-H activation step. This is in contrast to the RE in the presence of BQ which occurs with little barrier. We also investigated another planar transition state in which the Ph and the Bzq are on the Pd-N-O plane. However, the transition state could not be optimized; during the geometry optimization, the phenyl group deviated from the Pd-N-O plane and finally the same transition state as **TS_{3b}'** was presented. The non-planar transition state of the RE is not surprising; it was reported and the reason was discussed previously.[73]

It should be noticed that the $\Delta G^{0‡}$ and ΔG^0 values are 0.4 and -18.5 kcal/mol in the presence of BQ but 34.7 and 8.7 kcal/mol in the absence of BQ, where $\Delta G^{0‡}$ and ΔG^0 are defined as the Gibbs energy difference between **I_3** (or **I_3'**) and **TS_{3b}** (or **TS_{3b}'**) and that between **I_3** (or **I_3'**) and the product complex **P_3** (or **P_3'**), respectively, because we concentrate here on the RE. These results clearly indicate that BQ stabilizes the transition state and the product of the RE. One reason for this result is clear from the structures of **I_3'** and **TS_{3b}'**; because the phenyl group is on the Pd-Bzq-OAc plane in **I_3'**, the phenyl group must considerably move from the Pd-Bzq-OAc plane toward Bzq in **TS_{3b}'**, as shown in Fig. 10. As a result, **TS_{3b}'** is energetically unfavorable compared with **I_3'**, leading to the large $\Delta G^{0‡}$ value. On the other hand, the phenyl group does not need to move very much when going to **TS_{3b}** from **I_3** in the presence of BQ, as shown in Fig. 7. This is because the phenyl group takes the equatorial position in **I_3** and the geometry of **I_3** resembles well that of **TS_{3b}**; note that the C atom of Bzq, the Pd atom, and the O atom of the HOAc exist on the pseudo C_3 axis. In other words, the BQ coordination leads to the formation of five-coordinated trigonal bipyramidal intermediate in which the phenyl group takes the favorable position for the RE.

Another reason is the CT from the Pd to the BQ. In the presence of BQ, the Pd atomic population is +0.69 e in **TS_{3b}** and +0.45 e in **P_3**, while it is +0.36 e in **TS_{3b}'** and +0.32 e in **P_3'** in the absence of BQ. Consistent with these differences in the Pd atomic population, the population of BQ increases by 0.10 e during the RE step when going to **P_3** from **I_3**; see Fig. 9. These population changes indicate that the CT from the Pd to the BQ becomes stronger when going from **I_3** to **P_3**. Not only population changes but also the geometry of **P_3** supports this CT; in **P_3**, the C=C bond of the BQ moiety is moderately elongated (1.42 Å) compared with that of **I_3** (1.40 Å). Here it is noted that **P_3** is not a Pd(II) complex but a Pd(0) complex, indicating that the oxidation of Pd(0) to Pd(II) does not occurs in the presence of BQ. This result is consistent with the experimental fact that the direct cross-coupling reaction of arenes is stoichiometric in the presence of only BQ.

From these computational results, it should be clearly concluded that the BQ coordination with the Pd center leads to the smaller $\Delta G^{0\ddagger}$ and the more negative ΔG^0 of the RE than those in the absence of BQ; in other words, the arene-arene cross-coupling reaction easily occurs in the presence of BQ because the RE step is accelerated by BQ.

2.4 Conclusions

The synthetically useful arene cross-coupling reaction promoted by $Pd(OAc)_2$ was theoretically studied with the DFT, MP2 to MP4(SDQ), and CCSD(T) methods. BQ is experimentally reported to be necessary for this cross-coupling reaction. Our computational study elucidated the whole mechanism of this arene cross-coupling reaction and the role of BQ.

In this reaction, two C-H activations occur independently. The first is the C-H activation of HBzq, which leads to the formation of Pd(Bzq)(η^2-OAc). This process is understood in terms of heterolytic type C-H activation.[26] BQ easily coordinates to

Pd(Bzq)(η^2-OAc) to afford the trigonal bipyramidal Pd(II) complex Pd(Bzq)(η^2-OAc)(BQ). The coordinate bond is formed by the CT from the Pd to the BQ. This complex Pd(Bzq)(η^2-OAc)(BQ) is as stable as the square planar Pd(Bzq)(η^2-OAc). Both E_a and $\Delta G^{0‡}$ are small for the BQ coordination step, indicating that this step easily occurs. Then, the C-H activation of benzene occurs with $\Delta G^{0‡}$ value of 27.5 kcal/mol to afford the intermediate (**I_3**). Finally, the RE readily occurs with nearly no barrier; the $\Delta G^{0‡}$ value for this step is quite small (0.4 kcal/mol). These computational results suggest that the rate-determining step is the C-H activation of benzene by Pd(Bzq)(η^2-OAc)(BQ).

To clarify the role of BQ, we investigated the cross-coupling reaction of HBzq and benzene in the absence of BQ. The first step is the C-H activation of HBzq which is the same as that in the presence of BQ. After that, benzene coordinates to the Pd center to form Pd(Bzq)(η^2-OAc)(C_6H_6) (**P_2'**). The $\Delta G^{0‡}$ for this step is moderate (15.0 kcal/mol), indicating that the coordination of benzene easily occurs. Starting from **P_2'**, the C-H activation of benzene occurs via transition state **TS_{3a}'** to afford intermediate **I_3'**. Then, the RE of Bzq-Ph occurs via non-planar transition state **TS_{3b}'** to afford the product complex Pd(Bzq-Ph)(HOAc) **P_3'** (Bzq-Ph = 10-phenylbenzo[*h*]quinoline). The greatest difference from the reaction in the presence of BQ is observed in the structure of **I_3'**; in the absence of BQ, the phenyl group is on the Pd-Bzq-HOAc plane in **I_3'** in contrast to **I_3** in which the phenyl group takes the equatorial position of the trigonal bipyramidal structure. As a result, the RE step in the absence of BQ occurs with quite large geometry changes, but the RE occurs with moderate geometry changes in the presence of BQ. In addition to the smaller geometry changes, BQ stabilizes **TS_{3b}** and **P_3** by the back-donation from Pd(0) to BQ. Actually, the considerably large difference is observed in $\Delta G^{0‡}$ and ΔG^0 of the RE step; in the presence of BQ, the $\Delta G^{0‡}$ and ΔG^0 are 0.4 and -18.5 kcal/mol, respectively, while in the absence of BQ, the $\Delta G^{0‡}$ and ΔG^0 are 34.7 and 8.7 kcal/mol, respectively.

Our theoretical study clearly shows that BQ plays very important role in the RE step to

accelerate the arene-arene cross-coupling reaction. The next step for the understanding of this type of arene cross-coupling reaction is to clarify the mechanistic details of the catalytic reaction in the presence of Ag(I) salt (eq. 1b). The reaction conditions are somewhat different from those of reaction 1a; especially, the presence of Ag(I) salt may trigger another mechanistic pathways. Recently, the inner-sphere oxidation of Pd(II) by Ag(I) salt and the reaction mechanism involving Pd(III) species are proposed.[74,75] Its theoretical study is of considerable interest, which is in progress now.

Acknowledgements

This work was financially supported by Grand-in-Aids on basis research (No. 1530012), Priority Areas for "Molecular Theory for Real Systems" (No. 461), and NAREGI Project from the Ministry of Education, Science, Sports, and Culture. Some of theoretical calculations were performed with SGI workstations of Institute for Molecular Science (Okazaki, Japan), and some of them were carried out with PC cluster computers in our laboratory.

References

(1) Diederich, F.; in *Metal Catalyzed Cross-Coupling Reactions*, ed. de Mejiere, A.; John Wiley & Sons, New York, **2004**.

(2) Shilov, A. E.; in *Activation of Saturated Hydrocarbons by Transition Metal Complexes*, D. Reidel, Boston, MA, **1984**.

(3) Crabtree, R. H.; *Chem. Rev*. **1985**, 85, 245.

(4) Ryabov, A. D.; *Chem. Rev*. **1990**, 90, 403.

(5) Shilov, A. E.; Shulpin, B. G.; *Chem. Rev*. **1997**, 97, 2879.

(6) Dick, A. R.; Sanford, M. S.; *Tetrahedron* **2006**, 62, 2439.

(7) Labinger, J. A.; Bercaw, J. E.; *Nature* **2002**, 417, 507.

(8) Li, B.-J.; Yang, S.-D.; Shi, Z.-J.; *Synlett* **2008**, 7, 949.

(9) Lewis, J. C.; Bergman, R. G.; Ellman, J. A.; *Acc. Chem. Res.* **2008**, 41, 1013.

(10) Catellani, M.; Motti, E.; Ca', N. D.; Ferraccioli, R.; *Eur. J. Org. Chem.* **2007**, 4153.

(11) Carderas, D. J.; *Angew. Chem., Int. Ed.* **2003**, 42, 384.

(12) Li, R.; Jiang, L.; Lu, W.; *Organometallics* **2006**, 25, 5973.

(13) (a) Stille, J. K.; *Angew. Chem., Int. Ed.* **1986**, 25, 508. (b) Epsinet, P.; Echavarren, A. M.; *Angew. Chem., Int . Ed.* **2004**, 43, 4704.

(14) (a) Suzuki, A.; *Pure Appl. Chem.* **1994**, 66, 213. (b) Miyaura, N.; Suzuki, A.; *Chem. Rev.* **1995**, 95, 2457. (c) Indolese, A. F.; *Tetrahedron Lett.* **1997**, 38, 3513. (d) Kotha, S.; Lahiri, K.; Kashinath, D.; *Tetrahedron* **2002**, 58, 9633. (e) Miyaura, N.; *Top. Curr. Chem*. **2002**, 219, 11.

(15) (a) Mas-Balleste, R.; Que Jr., L.; *Science*, **2006**, 312, 1885. (b) Chen, M. S.; White, M. C.; *Science*, **2007**, 318, 783.

(16) (a) Beck, E. M.; Hatley, R.; Gaunt, M. J.; *Angew. Chem., Int. Ed.* **2008**, 47, 3004. (b) Bedford, R. G.; Betham, M.; *J. Org. Chem.* **2006**, 71, 9403. (c) Chen, K.; Richter, J. M.; Baran, P. S.; *J. Am. Chem. Soc.* **2008**, 130, 7247. (d) Christmann, M.; *Angew. Chem., Int. Ed.*

2008, 47, 2740. (e) Dai, X.; Wan, Z. L.; Kerr, R. G.; Davies, H. M. L.; *J. Org. Chem.* **2007**, 72, 1895. (f) Davies, H. M. L.; Dai, X.; *Tetrahedron* **2006**, 62, 10477. (g) Davies, H. M. L.; Dai, X.; Long, M. S.; *J. Am. Chem. Soc.* **2006**, 128, 2485. (h) Giri, R.; Yu, J. Q.; *J. Am. Chem. Soc*. **2008**, 130, 14082. (i) Kocovsky, P.; Dunn, V.; Gogoll, A.; Langer, V.; *J. Org. Chem.* **1999**, 64, 101. (j) Li, B. J.; Yang, S. D.; Shi, Z. J.; *Synlett* **2008**, 949. (k) Nicolaou, K. C.; Bulger, P. G.; Sarlah, D.; *Angew. Chem., Int. Ed.* **2005**, 44, 4442. (l) Torres, J. C.; Pinto, A. C.; Garden, S. J.; *Tetrahedron* **2004**, 60, 9889. (m) Tsai, A. S.; Bergman, R. G.; Ellman, J. A.; *J. Am. Chem. Soc.* **2008**, 130, 6316. (n) Verrier, C.; Martin, T.; Hoarau, C.; Marsais, F.; *J. Org. Chem.* **2008**, 73, 7383.

(17) Dyker, G.; *Angew. Chem., Int. Ed.* **1999**, 38, 1698.

(18) Ritleng, V.; Sirlin, C.; Pfeffer, M.; *Chem. Rev.* **2002**, 102, 1731.

(19) Kakiuchi, F.; Chatani, N.; *Adv. Shynth. Catal.* **2003**, 345, 1077.

(20) Alberico, D.; Scott, M. E.; Lautens, M.; *Chem. Rev.* **2007**, 107, 174.

(21) Burton, H. A.; Kozhevnikov, I. V.; *J. Mol. Catal. A* **2002**, 185, 285.

(22) Takahashi, M.; Masui, K.; Sekiguchi, H.; Kobayashi, N.; Mori, A.; Funahashi, M.; Tamaoki, N.; *J. Am. Chem. Soc*. **2006**, 128, 10930.

(23) Hull, K. L.; Lanni, E. L.; Sanford, M. S.; *J. Am. Chem. Soc*. **2006**, 128, 14047.

(24) Li, X. L.; Hewgley, J. B.; Mulrooney, C. A.; Yang, J. M. Kozlowski, M. C.; *J. Org. Chem*. **2003**, 68, 5500.

(25) Faccini, F.; Motti, E.; Catellani, M.; *J. Am. Chem. Soc.* **2004**, 126, 78.

(26) Cardenas, D. J.; Martin-Matute, B.; Echavarren, A. M.; *J. Am. Chem. Soc.* **2006**, 128, 5033.

(27) Stuart, D. R.; Fagnou, K.; *Science* **2007**, 316, 1172.

(28) (a) Murai, S.; Kakiuchi, F.; Sekine, S.; Tanaka, Y.; Kamatani, A.; Sonoda, M.; Chatani, N.; *Nature* **1993**, 366, 529. (b) Murai, S.; Kakiuchi, F.; Sekine, S.; Tanaka, Y.; Kamatani, A.; Sonoda, M.; Chatani, N.; *Pure Appl. Chem.* **1994**, 66, 1527. (c) Kakiuchi, F.; Sekine, S.;

Tanaka,Y.; Kamatani, A.; Sonoda, M.; Chatani, N.; Murai, S.; *Bull. Chem. Soc. Jpn.* **1995**, 68, 62. (d) Murai, S.; Chatani, N.; Kakiuchi, F.; *Pure Appl. Chem.* **1997**, 69, 589. (e) Chatani, N.; Morimoto, T.; Fukumoto, Y.; Murai, S.; *J. Am. Chem. Soc.* **1998**, 120, 5335.

(29) Matsubara, T.; Koga, N.; Musaev, D. G.; Morokuma, K.; *J. Am. Chem. Soc.* **1998**, 120, 12692.

(30) Hull, K. K.; Sanford, M. S.; *J. Am. Chem. Soc.* **2007**, 129, 11904.

(31) Chen, X.; Li, J.-J.; Hao, X.-S.; Goodhue, C. E.; Yu, J.-Q.; *J. Am. Chem. Soc.* **2006**, 128, 78.

(32) (a) Albeniz, A. C.; Epsinet, P.; Martin-Ruiz, B.; *Chem. –Eur. J.* **2001**, 7, 2481. (b) Backvall, J.-E.; Bystrom, S. E.; Nordberg, R. E.; *J. Org. Chem.* **1984**, 49, 4619.

(33) Saillard, J.-Y.; Hoffmann, R.; *J. Am. Chem. Soc.* **1984**, 106, 2006.

(34) (a) Obara, S.; Kitaura, K.; Morokuma, K.; *J. Am. Chem. Soc.* **1984**, 106, 7482. (b) Koga, N.; Morokuma, K.; *J. Am. Chem. Soc.* **1990**, 94, 5454. (c) Koga, N.; Morokuma, K.; *J. Am. Chem. Soc.* **1993**, 115, 6883.

(35) (a) Low, J. J.; Goddard, W. A.; *J. Am. Chem. Soc.* **1986**, 108, 6115. (b) Low, J. J.; Goddard, W. A.; *Organometallics* **1986**, 5, 609.

(36) (a) Blomberg, M. R. A.; Siegbahn, P. E. M.; Nagashima, U.; Wennerberg, J.; *J. Am. Chem. Soc.* **1991**, 113, 424. (b) Svensson, M.; Blomberg, M. R. A.; Siegbahn, P. E. M.; *J. Am. Chem. Soc.* **1991**, 113, 7076. (c) Blomberg, M. R. A.; Siegbahn, P. E. M.; Svensson, M.; *J. Am. Chem. Soc.* **1992**, 114, 6095. (d) Siegbahn, P. E. M.; Blomberg, M. R. A.; Svensson, M.; *J. Am. Chem. Soc.* **1993**, 115, 4191. (e) Blomberg, M. R. A.; Siegbahn, P. E. M.; Svensson, M.; *J. Phys. Chem.* **1994**, 98, 2062. (f) Siegbahn, P. E. M.; Blomberg, M. R. A.; *Organometallics* **1994**, 13, 354. (g) Siegbahn, P. E. M.; *Organometallics* **1994**, 13, 2833. (h) Siegbahn, P. E. M.; Svensson, M.; *J. Am. Chem. Soc.* **1994**, 116, 10124. (i) Siegbahn, P. E. M.; *J. Am. Chem. Soc.* **1996**, 118, 1487. (j) Siegbahn, P. E. M.; Carbtree, R. H.; *J. Am. Chem. Soc.* **1996**, 118, 4442.

(37) (a) Song, J.; Hall, M. B.; *Organometallics* **1993**, 12, 3118. (b) Jimenez-Catao, R.; Hall, M. B.; *Organometallics* **1996**, 15, 1889. (c) Niu, S.-Q.; Hall, M. B.; *J. Am. Chem. Soc.* **1998**, 120, 6169.

(38) (a) Sakaki, S.; Ieki, M.; *J. Am. Chem. Soc.* **1993**, 115, 2373. (b) Sakaki, S.; Biswas, B.; Sugimoto, M.; *J. Chem. So*c., *Dalton Trans*. **1997**, 803. (c) Sakaki, S.; Biswas, B.; Sugimoto, M.; *Organometallics* **1998**, 17, 1278.

(39) Hinderling, C.; Feichtinger, D.; Plattner, D. A. Chen, P.; *J. Am. Chem. Soc.* **1997**, 119, 10793.

(40) Su and, M.-D.; Chu, S.-Y.; *J. Am. Chem. Soc.* **1997**, 119, 5373.

(41) Espinosa-Garcia, J.; Corchado, J. C.; Truhlar, D. G.; *J. Am. Chem. Soc.* **1997**, 119, 9891.

(42) (a) Yoshizawa, K.; Ohta, T.; Yamabe, T.; Hoffmann, R.; *J. Am. Chem. Soc.* **1997**, 119, 12311. (b) Yoshizawa, K.; Shiota, Y.; Yamabe, T.; *J. Am. Chem. Soc.* **1998**, 120, 564. (c) Yoshizawa, K.; Shiota, Y.; Yamabe, T.; *J. Am. Chem. Soc.* **1998**, 121, 147.

(43) Mylvaganam, K.; Bacskay, G. B.; Hush, N. S.; *J. Am. Chem. Soc.* **1999**, 121, 4633.

(44) Beletskaya, I. P. ; Bessmertnykh, A. G.; Guilard, R.; *Tetrahedron Lett.* **1999**, 40, 6393.

(45) Gotov, B.; Kaufmann, J.; Schumann, H.; Schmalz, H. G.; *Synlett* **2002**, 361.

(46) Schumann, H.; Kaufmann, J.; Schmalz, H. G.; Bottcher, A.; Gotov, B.; *Synlett* **2003**, 1783.

(47) Ackerman, L. J.; Sadighi, J. P.; Kurtz, D. M.; Labinger, J. A.; Bercaw, J. E.; *Organometallics* **2003**, 22, 3884.

(48) Prim, D.; Andrioletti, B.; Rose-Munch, F.; Rose, E.; Couty, F.; *Tetrahedron* **2004**, 60, 3325.

(49) Christmann, U.; Pantazis, D. A.; Benet-Buchholz, J.; McGrady, J. E.; Maseras, F.; Vilar, R.; *Organometallics* **2006**, 25, 5990.

(50) Cho, S. H.; Hwang, S. J.; Chang, S.; *J. Am. Chem. Soc.* **2008**, 130, 9254.

(51) Fu, Y.; Li, Z.; Liang, S.; Guo, Q. X. Liu, L.; *Organometallics* **2008**, 27, 3736.

(52) Biswas, B.; Sugimoto, M.; Sakaki, S.; *Organometallics*, **2000**, 19, 3895.

(53) Ochi, N.; Nakao, Y.; Sato, H.; Sakaki, S.; *J. Am. Chem. Soc.* **2007**, 129, 8615.

(54) Lafarance, M.; Rowley, C. N.; Woo, T. K.; Fagnou, K.; *J. Am. Chem. Soc.* **2006**, 128, 8754.

(55) Ozdemir, I.; Demir, S.; Cetinkaya, B.; Gourlaouen, G.; Maseras, F.; Bruneau, C.; Dixneuf, P. H.; *J. Am. Chem. Soc.* **2008**, 130, 1156.

(56) Becke, A. D.; *Phys. Rev. A* **1988**, 38, 3098.

(57) Perdew, J. P.; Chevary, J. A.; Vosko, S. H.; Jackson, K. A.; Pederson, M. R.; Singh, D. J.; Fiolhais, C.; *Phys. Rev. B*, **1992**, 46, 6671.

(58) Perdew, J. P. ; Burke, K.; Wang, Y.; *Phys. Rev. B* **1996**, 54, 16533.

(59) Hay, P. J.; Wadt, W. R.; *J. Chem. Phys.* **1985**, 82, 270.

(60) Ditchfield, R.; Hehre, W. J.; Pople, J. A.; *J. Chem. Phys.* **1971**, 54, 724.

(61) Andrae, D.; Haussermann, U.; Dolg, M.; Stoll, H.; Preuss, H.; *Theor. Chem. Acta.* **1990**, 77, 123.

(62) Dunning Jr., T. H.; *J. Chem. Phys*. **1989**, 90, 1007.

(63) Miertus, S.; Scrocco, E.; Tomasi, J.; *Chem. Phys.* **1981**, 55, 117.

(64) Mammen, M.; Shakhnovich, E. I.; Deutch, J. M.; Whitesides, G. M.; *J. Org. Chem.* **1998**, 63, 3821.

(65) Pople, J. A.; *et al. Gaussian 03, ReVision C.02*, Gaussian: Inc.:Wallingford, CT, **2004**.

(66) Carpenter, J. E.; Weinhold, F.; *J. Mol. Struct. (Theochem)*, **1988**, 169, 41.

(67) Catellani, M.; Mealli, C.; Motti, E.; Paoli, P.; Perez-Carreno, E.; Pregosin, P. S.; *J. Am. Chem. Soc.* **2002**, 124, 4336.

(68) (a) Maseras, F.; Morokuma, K.; *J. Comp. Chem.* **1995**, 16, 1170 (b) Humbel, S.; Sieber, S.; Morokuma, K.; *J. Chem. Phys.* **1996**, 105, 1959. (c) Matsubara, T.; Sieber, S.; Morokuma, K.; *Int. J. Quant. Chem.* **1996**, 60, 1101. (d) Svensson, M.; Humbel, S.; Froese, R. D. J.;

Matsubara, T.; Sieber, S.; Morokuma, K.; *J. Phys. Chem.* **1996**, 100, 19357. (e) Svensson, M.; Humbel, S.; Morokuma, K.; *J. Chem. Phys.* **1996**, 105, 3654. (f) Dapprich, S.; Komaromi, I.; Byun, K. S.; Morokuma, K.; Frisch, M. J.; *J. Mol. Struct. (Theochem)*, **1999**, 462, 1. (g) Vreven, T.; Morokuma, K.; *J. Comp. Chem.* **2000**, 21, 1419. (h) Sakaki, S.; Mizoe, N.; Sugimoto, M.; *Organometallics*, **1998**, 17, 2510.

(69) (a) Ozawa, F.; Hikida, T.; Hayashi, T.; *J. Am. Chem. Soc.* **1994**, 116, 2844 (b) Albeniz, A. C.; Epsinet, P.; Matin-Ruiz, B.; *Chem. Eur. J.* **2001**, 7, 2483.

(70) Szabo, K. J.; *Organometallics*, **1998**, 17, 1677.

(71) Rosso, A. R.; Hoffmann, R.; *Inorg. Chem.* **1975**, 14, 365.

(72) (a) Kameno, Y.; Ikeda, A.; Nakao, Y.; Sato, H.; Sakaki, S.; *J. Phys. Chem. A*, **2005**, 109, 8055. (b) Ikeda, A.; Kameno, Y.; Nakao, Y.; Sato, H.; Sakaki, S.; *J. Organomet. Chem.* **2007**, 692, 299. (c) Ikeda, A.; Nakao, Y.; Sato, H.; Sakaki, S.; *J. Phys. Chem. A*, **2007**, 111, 7142.

(73) Sakaki, S.; Mizoe, N.; Musashi, Y.; Biswas, B.; Sugimoto, M.; *J. Phys. Chem. A*, **1998**, 102, 8027.

(74) Lanci, M. P.; Remy, M. S.; Kaminsky, W.; Mayer, J. M.; Sanford, M. S.; *J. Am. Chem. Soc*. **2009**, 131, 15618.

(75) Powers, D. C.; Ritter, T.; *Nature chemistry*, **2009**, 1, 302.

2.5 Appendix

Complete Representation of Ref. 65

Frisch, M. J.; Trucks, G. W.; Schlegel, H. B.; Scuseria, G. E.; Robb, M. A.; Cheeseman, J. R.; Montgomery, J. A., Jr.; Vreven, T.; Kudin, K. N.; Burant, J. C.; Millam, J. M.; Iyengar, S. S.; Tomasi, J.; Barone, V.; Mennucci, B.; Cossi, M.; Scalmani, G.; Rega, N.; Petersson, G. A.; Nakatsuji, H.; Hada, M.; Ehara, M.; Toyota, K.; Fukuda, R.; Hasegawa, J.; Ishida, M.; Nakajima, T.; Honda, Y.; Kitao, O.; Nakai, H.; Klene, M.; Li, X.; Knox, J. E.; Hratchian, H. P.; Cross, J. B.; Bakken, V.; Adamo, C.; Jaramillo, J.; Gomperts, R.; Stratmann, R. E.; Yazyev, O.; Austin, A. J.; Cammi, R.; Pomelli, C.; Ochterski, J. W.; Ayala, P. Y.; Morokuma, K.; Voth, G. A.; Salvador, P.; Dannenberg, J. J.; Zakrzewski, V. G.; Dapprich, S.; Daniels, A. D.; Strain, M. C.; Farkas, O.; Malick, D. K.; Rabuck, A. D.; Raghavachari, K.; Foresman, J. B.; Ortiz, J. V.; Cui, Q.; Baboul, A. G.; Clifford, S.; Cioslowski, J.; Stefanov, B. B.; Liu, G.; Liashenko, A.; Piskorz, P.; Komaromi, I.; Martin, R. L.; Fox, D. J.; Keith, T.; Al-Laham, M. A.; Peng, C. Y.; Nanayakkara, A.; Challacombe, M.; Gill, P. M. W.; Johnson, B.; Chen, W.; Wong, M. W.; Gonzalez, C.; Pople, J. A. *Gaussian 03, Revision D.02*, Gaussian, Inc., Wallingford CT, 2004.

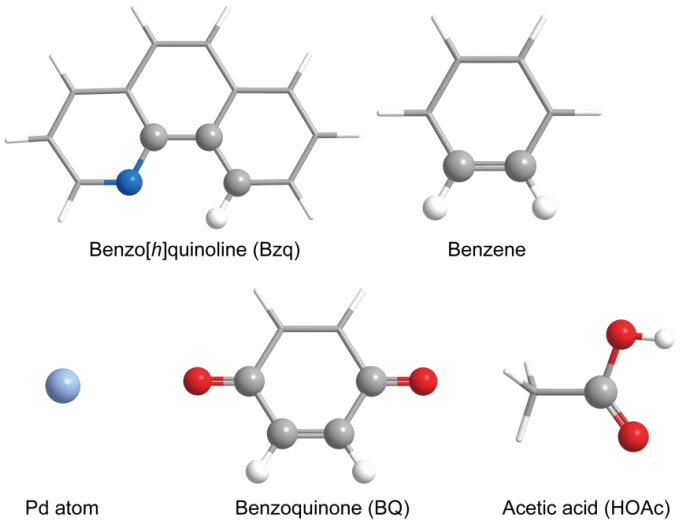

Scheme A1. Large model for ONIOM method. Atoms shown by balls are included in high level region which is calculated with the CCSD(T) while whole system is calculated by the lower level of theory.

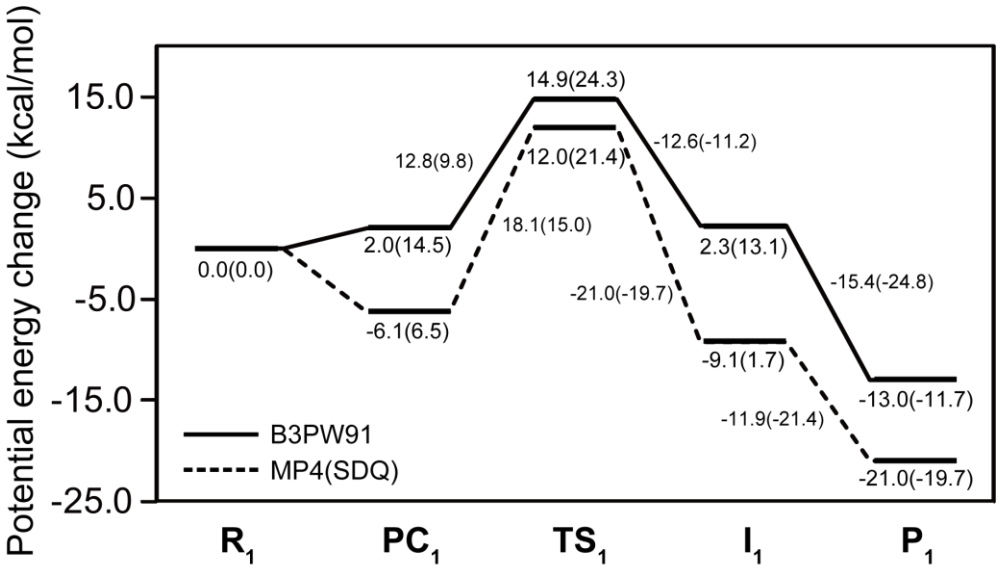

Fig. A1. Potential energy changes by the C-H activation of Bzq by Pd(η^2-OAc)$_2$ in gas phase. Energies [a)] are given in kcal/mol unit. [a)] In parentheses are Gibbs free energy changes.

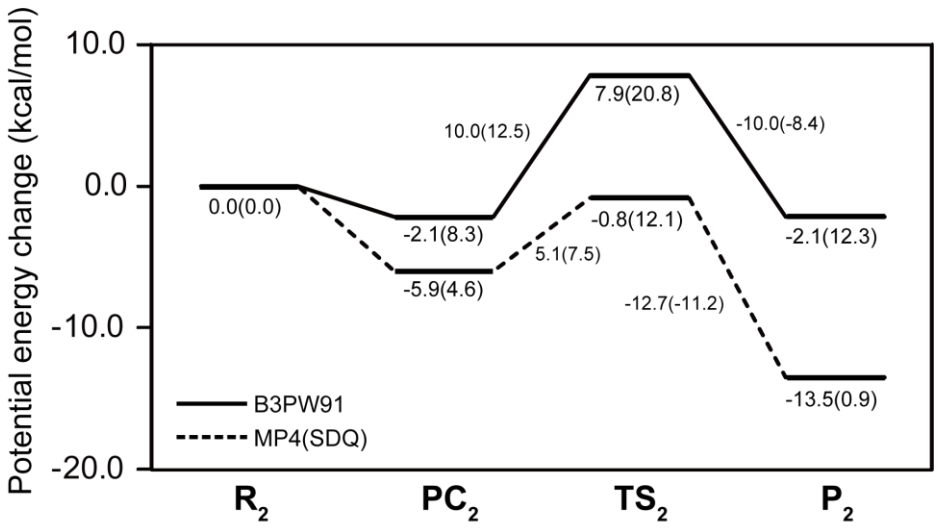

Fig. A2. Potential energy changes by BQ coordination to Pd(Bzq)(OAc) in gas phase. Energies [a)] are given in kcal/mol unit. [a)] In parentheses are Gibbs free energy changes.

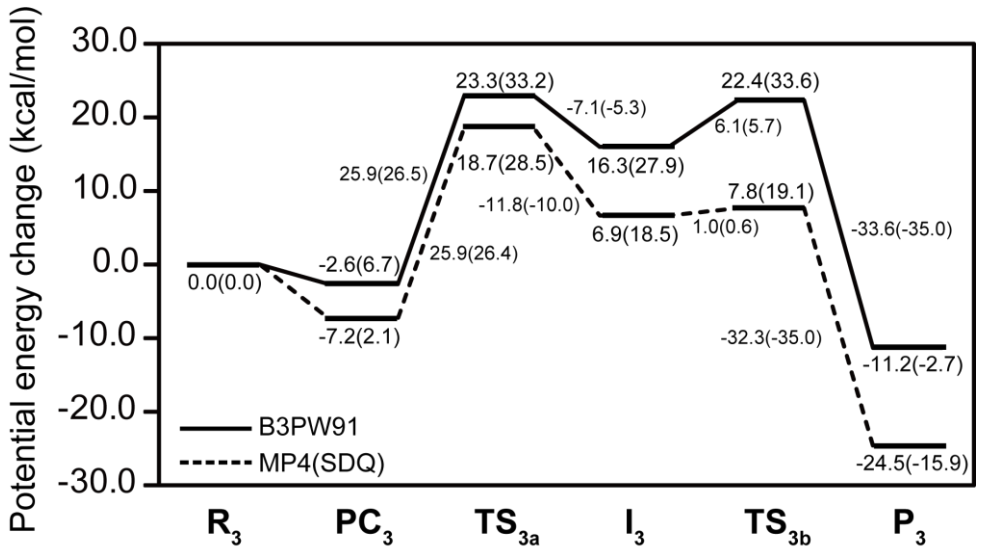

Fig. A3. Potential energy changes for the C-H activation of benzene by Pd(Bzq)(OAc)(BQ) in gas phase. Energies [a)] are given in kcal/mol unit. [a)] In parentheses are Gibbs free energy changes.

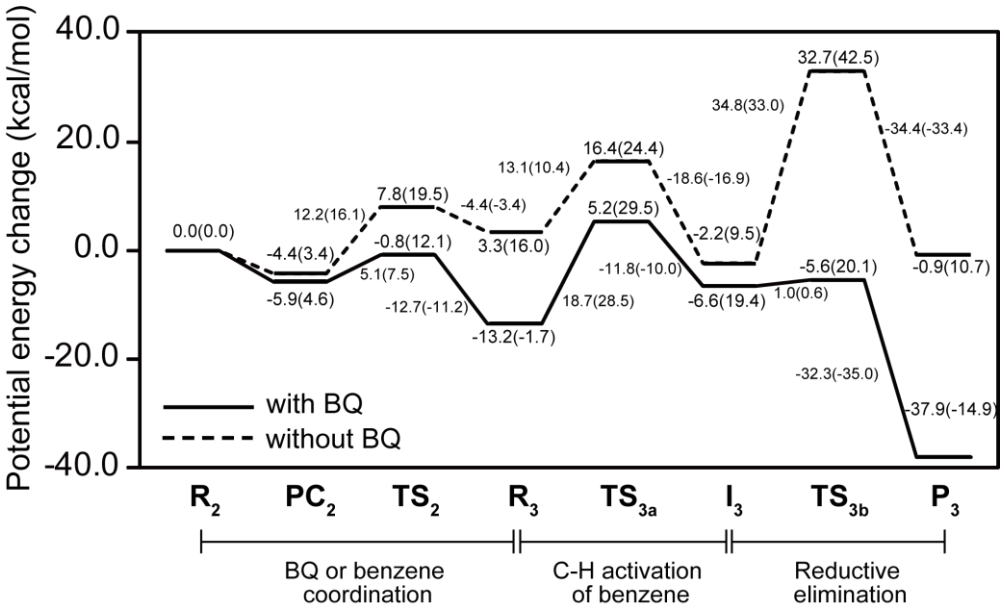

Fig. A4. Potential energy changes for the C-H activation of benzene by Pd(Bzq)(OAc)(BQ) in gas phase. Energies [a)] are given in kcal/mol unit. [a)] In parentheses are Gibbs free energy changes.

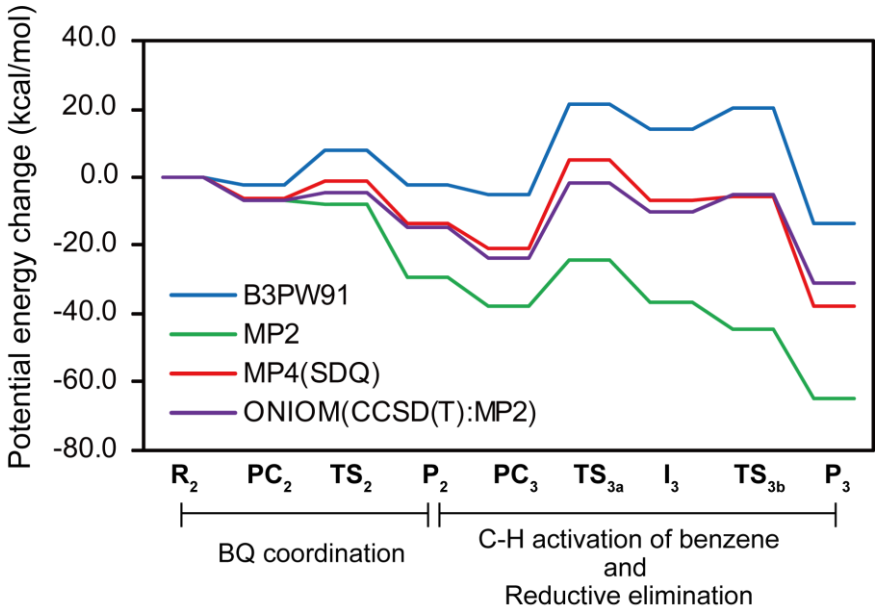

Fig. A5. Potential energy change of the BQ coordination, the C-H activation of benzene, and the reductive elimination in gas phase calculated with DFT, MP2, MP4(SDQ), and ONIOM(CCSD(T):MP2) methods. Energies are given in kcal/mol unit.

Table A1.Relative electronic energies (BS-II) of the C-H activation of HBzq, BQ coordination, and the C-H activation of benzene, calculated by Hartree-Fock, MP2, MP3, MP4(DQ), MP4(SDQ), and DFT(B3PW91) methods.[a)] Energies are given in kcal/mol unit.

		HF	MP2	MP3	MP4(DQ)	MP4(SDQ)	B3PW91
First C-H activation	$\mathbf{R_1}$	0.0	0.0	0.0	0.0	0.0	0.0
	$\mathbf{PC_1}$	12.7	-14.1	-2.5	-4.8	-6.1	2.0
	$\mathbf{TS_{1a}}$	35.2	1.6	14.2	13.4	12.0	14.9
	$\mathbf{I_1}$	12.5	-19.8	-6.7	-9.7	-9.1	2.3
	$\mathbf{P_1}$	-1.7	-32.8	-17.5	-21.9	-21.0	-13.0
BQ coordination	$\mathbf{R_2}$	0.0	0.0	0.0	0.0	0.0	0.0
	$\mathbf{PC_2}$	-2.4	-7.0	-5.5	-5.5	-5.9	-2.1
	$\mathbf{TS_2}$	21.2	-7.7	4.0	2.0	-0.8	7.9
	$\mathbf{P_2}$	25.7	-29.0	-1.0	-9.3	-13.5	-2.1
Second C-H activation and Reductive Elimination	$\mathbf{R_3}$	0.0	0.0	0.0	0.0	0.0	0.0
	$\mathbf{PC_3}$	-3.4	-8.8	-7.0	-7.0	-7.2	-2.6
	$\mathbf{TS_{3a}}$	45.3	5.1	23.3	19.4	18.7	23.3
	$\mathbf{I_3}$	30.0	-7.3	12.5	6.2	6.9	16.3
	$\mathbf{TS_{3b}}$	43.4	-15.4	21.6	6.7	7.8	22.4
	$\mathbf{P_3}$	-14.9	-35.6	-18.2	-27.3	-24.5	-11.2

Chapter 3

Theoretical Study of Photoinduced Epoxidation of Olefins Catalyzed by Ruthenium Porphyrin

Abstract

Epoxidation of olefin by $[Ru(TMP)(CO)(O)]^-$ (TMP = tetramesitylporphine), which is a key step of the photocatalyzed epoxidation of olefin by [Ru(TMP)(CO)], is studied mainly with the DFT method, where [Ru(Por)(CO)] is employed as a model complex (Por = unsubstituted porphyrin). The CASSCF method was also used to investigate the electronic structure of important species in the catalytic cycle. The CASSCF and DFT methods provide essentially the same electronic structure of the active species $[Ru(Por)(CO)(O)]^-$, suggesting that the DFT method can be applied to the epoxidation reaction by $[Ru(Por)(CO)(O)]^-$. Present computational results show characteristic features of this reaction, as follows: (i) The epoxidation reaction occurs via carboradical-type transition state. Neither carbocation-type nor concerted oxene-insertion type character is observed in the transition state. (ii) Electron and spin populations transfer from the olefin moiety to the porphyrin ring in the step of the C-O bond formation. (iii) Electron and spin populations of the olefin and porphyrin moieties considerably change around the transition state. On the other hand, those of the Ru center little change in the reaction, indicating that the Ru center keeps +II oxidation state in whole catalytic cycle. (iv) The stability of the olefin adduct $[Ru(Por)(CO)(O)(olefin)]^-$ considerably depends on the kind of olefin, such as ethylene, *n*-hexene, and styrene. In particular, styrene forms a very stable olefin adduct. (v) Interestingly, however, the difference in the activation barrier among these olefins is small in quantitative level (within 5 kcal/mol), indicating that this catalyst can be applied to various substrates. This result arises from the fact that the stabilities and electronic structures of both of the olefin adduct and the transition state are similarly influenced by the substituent of olefin.

3.1 Introduction

A lot of catalytic reactions with high efficiency are often found in biological systems, as well known.[1] In many of them, metalloenzymes play key roles as catalyst. Especially, metalloporphyrins participate in various catalytic reactions.[2] Their catalyses are interesting not only from the viewpoint of biological chemistry but also from the viewpoint of catalytic chemistry.[3,4] In this regard, a lot of efforts were made to find efficient bio-inspired catalysts. Good examples are metalloporphyrin-catalyzed epoxidation of olefin[5-10] and hydroxylation of alkane,[11,12] which are biomimetic reactions inspired by catalyses of cytochrome P450. Interestingly, olefin epoxidation is catalyzed not only by iron porphyrin but also by other metalloporphyrins such as chromium, manganese, and ruthenium porphyrins.[1-5]

Olefin epoxidation is one of the most important synthetic processes because the epoxide is good starting material for various alcohols and aldehydes. Especially, regio- and stereoselective epoxidation by mild oxidants such as dioxygen molecule is highly desired for pharmaceutical syntheses, because it is in general difficult to perform asymmetric epoxidation of unsaturated steroids under drastic reaction conditions.[13] In biological systems, on the other hand, the regio- and stereoselective epoxidation is efficiently catalyzed by cytochrome P450. This suggests that metalloporphyrins are good candidate for an efficient catalyst which can be applied to the epoxidation reaction with dioxygen molecule. Metalloporphyrins are also interesting from theoretical point of view, because they take various electronic structures with unusual oxidation state of the metal center. For instance, various spin states have been reported in iron porphyrin, which has been extensively studied both experimentally and theoretically.[5-12] Also, it is noted that various iron porphyrins have been synthesized by modifying axial ligands and/or substituents on the porphyrin ring. This means that one can achieve tuning of electronic structure and steric effect of metalloporphyrin catalyst by employing various metal centers, substituents, and axial ligands.

Among metalloporphyrin catalysts for olefin epoxidation, [Ru(TMP)$(O)_2$] (TMP =

(A) The catalytic cycle for olefin epoxidation by [Ru(Por)(CO)]

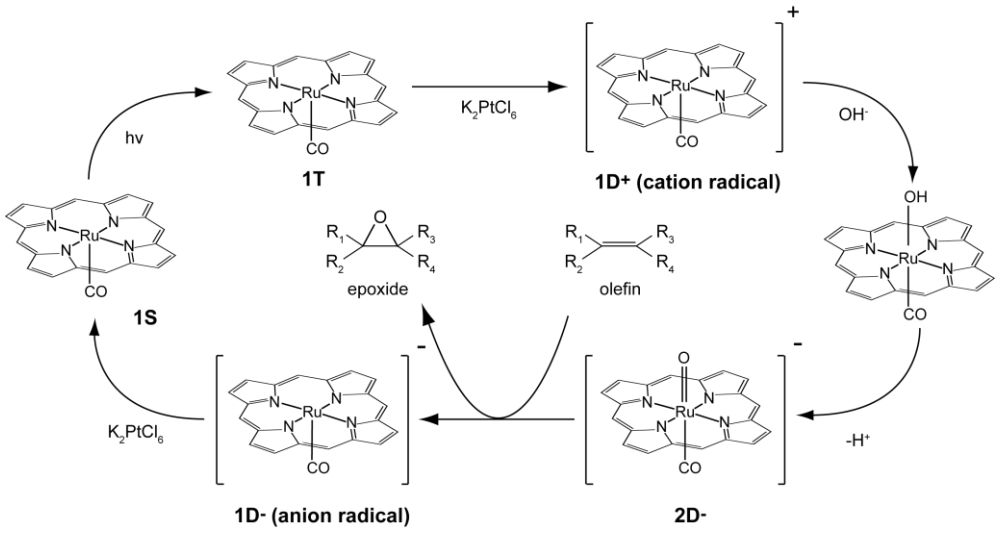

(B) Proposed mechanistic pathways for olefin epoxidation

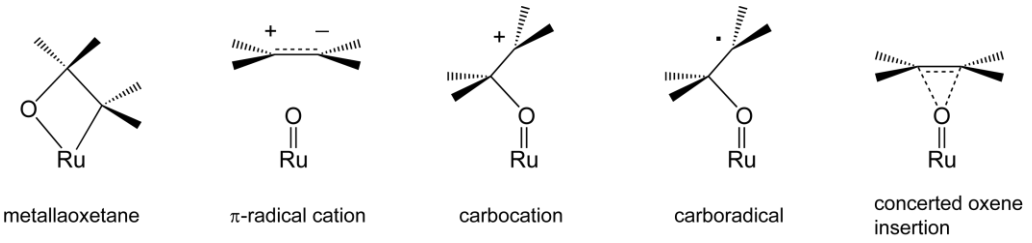

Scheme 1

tetramesitylporphine) draws a lot of interests because this is formed by mild oxidizing agents such as dioxygen molecule.[7, 8,14] However, its application to the olefin epoxidation has been limited so far, because the product yield and the stereoselectivity strongly depend on olefin substrate. To improve the catalytic efficiency, we need the correct knowledge of the reaction mechanism and the active species. For the epoxidation reaction, various mechanistic pathways have been proposed.[10] In the case of [Ru(TMP)$(O)_2$]-catalyzed epoxidation reaction, the carboradical mechanism was proposed as one of the plausible mechanisms, based on the kinetic isotope effect.[15] However, the direct evidence has not been reported yet.

Recently, the similar complex [Ru(TMP)(CO)] was successfully applied to the olefin

epoxidation under UV/Vis light irradiation.[16] Its mechanism is experimentally proposed, as shown in Scheme 1(A). Interestingly, the stereoselectivity of the epoxide product is considerably higher than in the epoxidation catalyzed by [Ru(TMP)$(O)_2$]. The quantum yield of this photo-induced epoxidation reaches 0.60 with high selectivity of 94.4 % for the epoxidation of cyclohexene and 0.40 with high selectivity of 99.7 % for the epoxidation of norbornene. The characteristic features of this reaction are summarized,[16] as follows: (i) The formation of cation radical $[Ru(\cdot TMP)(CO)]^+$ upon the UV/Vis light irradiation was proposed, based on the experimental fact that the UV/Vis spectrum just after the light irradiation is similar to that of cation radical $[Ru(\cdot TMP)(CO)]^+$ which is produced by electrochemical oxidation. (ii) The oxidation state of the Ru center is proposed to change among +I, +II, and +III in the epoxidation reaction, suggesting that the Ru center is more electron rich than in [Ru(TMP)$(O)_2$] whose Ru center takes +VI oxidation state. (iii) $[Ru(TMP)(CO)(O)]^-$ was experimentally proposed as an active species. (iv) The isotope experiment with ^{18}O clearly indicated that the oxygen atom of epoxide comes from H_2O involved in the reaction system.[16] This result suggests that $[Ru(\cdot TMP)(CO)]^+$ reacts with H_2O to form either [Ru(TMP)(CO)(OH)] in neutral solution or $[Ru(TMP)(CO)(O)]^-$ in basic solution. (v) The product selectivity is higher and the quantum yield is much larger in basic solution than in neutral solution, suggesting that $[Ru(TMP)(CO)(O)]^-$ is an active species.

From synthetic point of view, this photo-induced epoxidation is useful because strong oxidizing agent is not necessary. Also, this reaction is interesting from the viewpoint of fundamental chemistry, as follows: Many reaction mechanisms were proposed for metal-catalyzed epoxidation, as shown in Scheme 1(B). Though the carboradical mechanism is considered to be plausible, as mentioned above, it is necessary to elucidate the reaction mechanism with theoretical evidence and to clarify geometries and electronic structures of active species, important intermediates, and transition states. Also, it is of considerable interest to clarify the reason why this catalyst can be applied to various substrates.

In this work, we theoretically investigated the epoxidation reaction by $[Ru(TMP)(CO)(O)]^-$ (eq 1) to present theoretical answers to above-mentioned questions.

$$[Ru(TMP)(CO)(O)]^- + Olefin \rightarrow [Ru(TMP)(CO)]^- + Epoxide \quad (1)$$

Although metalloporphyrins have been theoretically investigated in many works,[17] theoretical studies of their epoxidation catalyses have been rather limited.[5-10] We wish to emphasize that clear understanding is presented here on the electronic process of this epoxidation reaction including re-distribution of electron and spin populations.

3.2 Models and Computational Details

We constructed the model system, as follows: The mesityl groups of Ru(TMP) were replaced by hydrogen atoms. Ethylene was employed as substrate unless otherwise noted. We mainly investigated the singlet and triplet states of neutral [Ru(Por)(CO)] and the doublet states of $[Ru(\cdot Por)(CO)]^+$, $[Ru(\cdot Por)(CO)]^-$, and $[Ru(Por)(CO)(O)]^-$. For brevity, we employ following abbreviations hereafter, (i) **1S** and **1T** for the singlet and triplet states of [Ru(Por)(CO)], respectively. (ii) $\mathbf{1D}^+$ and $\mathbf{1D}^-$ for the doublet states of $[Ru(\cdot Por)(CO)]^+$ and $[Ru(\cdot Por)(CO)]^-$, respectively, and (iii) $\mathbf{2D}^-$ for the doublet state of $[Ru(Por)(CO)(O)]^-$. **1S** is calculated by the restricted DFT method and other species are calculated by the unrestricted DFT (UDFT) method.

Besides, we employed the CASSCF method to take the multi-reference character into consideration in $[Ru(TMP)(CO)(O)]^-$. Remember the experimental proposal that the oxidation state of the Ru center changes among +I to +III in the reaction.[16] In such unusual +I and +III oxidation states, we must be careful for the multi-reference character.

All geometries were optimized with the DFT method using the B3PW91 functional.[18-21] The vibrational frequency was evaluated with the same method to ascertain that equilibrium geometry has no imaginary frequency and transition state has one imaginary frequency.

Two basis set systems (BS-I and BS-II) were employed here: In BS-I, Stuttgart-Dresden-Bonn effective core potentials (ECPs) were employed to replace core electrons of ruthenium atom, and a (311111/22111/411) basis set was employed to represent its valence electrons.[22] Usual 6-31G(d) basis sets[23] were employed for carbon, nitrogen, and hydrogen atoms, and 6-311G(d) basis sets were employed for oxygen atom. In BS-II, cc-pVDZ basis sets[24] were employed for carbon, nitrogen, oxygen, and hydrogen atoms, while the same basis sets and ECPs as those of BS-I were employed for ruthenium atom. The BS-I was used for geometry optimization and calculation of vibrational frequency. The BS-II was used for evaluation of energy changes. Zero-point energy was evaluated with the DFT/BS-I method under assumption of harmonic oscillator.

For CASSCF calculations, BS-II was employed. **1S**, **1T**, $\mathbf{1D}^{+}$, $\mathbf{1D}^{-}$, and $\mathbf{2D}^{-}$ were calculated under the C_{2v} symmetry. We employed active spaces containing 14, 14, 13, and 15 electrons in such 14 orbitals as five a_1, three b_1, three a_2, and three b_2 orbitals for **1S**, **1T**, $\mathbf{1D}^{+}$, $\mathbf{1D}^{-}$, and $\mathbf{2D}^{-}$, respectively. These active spaces were determined, as follows: i) All 4d orbitals and 4d electrons of Ru must be included in the active space. ii) Ru 5d-like orbitals which correlate with usual 4d orbitals must be also included to incorporate "double-shell effect".[25] iii) Four π orbitals of the porphyrin ring known as Gouterman's four orbitals must be included, which are two occupied orbitals in a_1 and b_2 symmetries and two unoccupied orbitals in a_2 and b_1 symmetries.[26] For $\mathbf{2D}^{-}$, 15 electrons are included in the above-mentioned 14 orbitals and one more b_2 orbital which is added to represent the Ru-O anti-bonding interaction; see Figure A1 in Appendix for these active spaces.

Geometry optimization, frequency calculation, and energy evaluation by the DFT method were performed with Gaussian 03 program package.[27] CASSCF calculations were performed with MOLCAS 6.0 program package.[28] NBO analysis was carried out with NBO program version 3.1.[29]

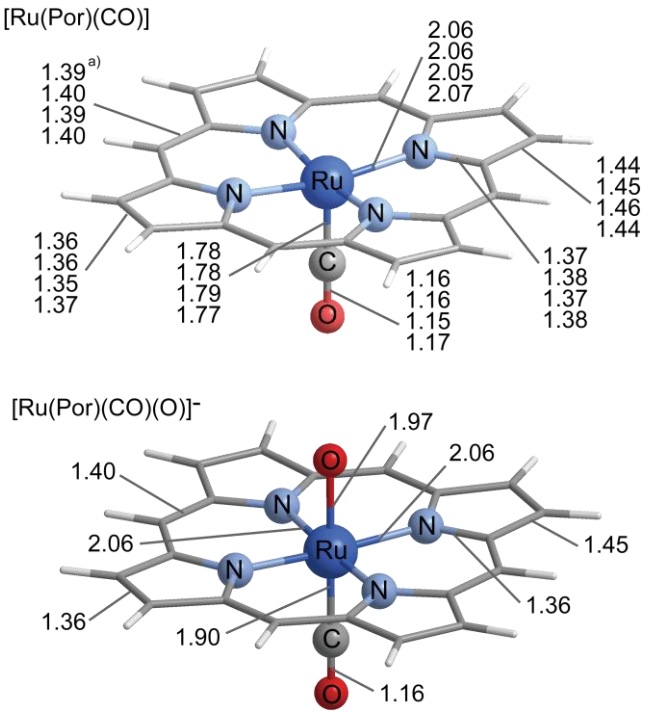

Figure 1. Selected bond lengths (Å) of optimized geometries of **1S**, **1T**, **1D**$^{+}$, **1D**$^{-}$, and **2D**$^{-}$. a) Bond lengths are presented in the order of **1S**, **1T**, **1D**$^{+}$, and **1D**$^{-}$.

3.3 Results and Discussions

3.3.1 Geometry and Electronic Structure of Active Species [Ru(Por)(CO)(O)]$^{-}$

First, we investigated [Ru(Por)(CO)] to characterize [Ru(Por)(CO)(O)]$^{-}$ by making comparison between these two compounds. Geometry of the singlet state of [Ru(Por)(CO)] **1S** was optimized, as shown in Figure 1. Geometry optimization of the triplet state **1T** was also carried out with the UDFT(B3PW91)/BS-I method. The geometry of [Ru(Por)(CO)] is C_{4v} symmetrical in **1S** and **1D**$^{+}$ and C_{2v} symmetrical in **1T** and **1D**$^{-}$. **1T** is much less stable than **1S** by 48.4 kcal/mol, indicating that **1S** is the ground state.

(A) Frontier molecular orbitals of 1S of [Ru(Por)(CO)]

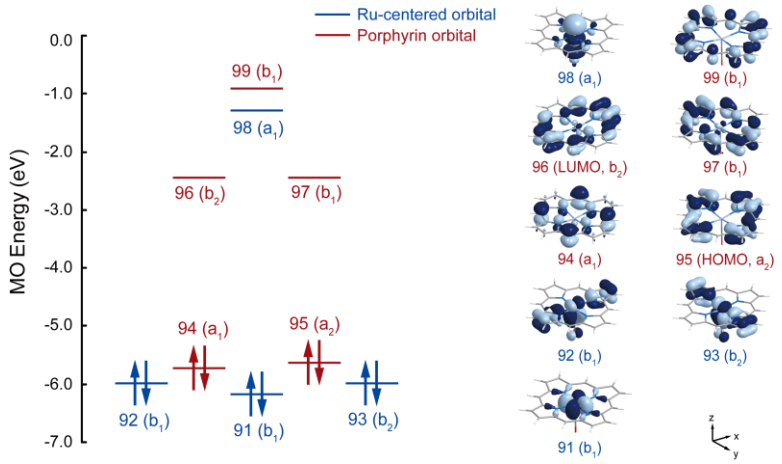

(B) UDFT natural orbital of $[Ru(Por)(CO)(O)]^-$ $2D^-$ a)

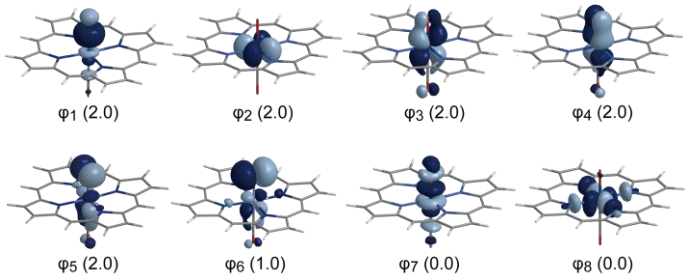

(C) Molecular orbital diagrams for frontier orbitals of $[Ru(Por)(CO)(O)]^-$ $2D^-$

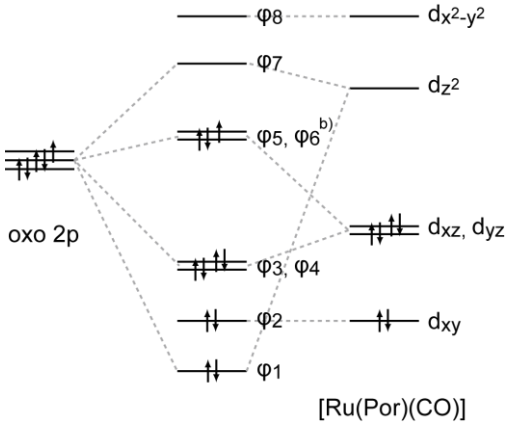

Figure 2. Important molecular orbitals of [Ru(Por)(CO)] and $[Ru(Por)(CO)(O)]^-$. a) Natural orbital occupation numbers are shown in parentheses. b) The φ_5 and φ_6 are split in energy by Jahn-Teller effect.

As seen in Figure 1, structural parameters of the porphyrin ring are similar between [Ru(Por)(CO)] and $[Ru(Por)(CO)(O)]^-$. However, the Ru-C bond of $[Ru(Por)(CO)(O)]^-$ is somewhat longer than that of [Ru(Por)(CO)] by about 0.1 Å. Because the C-O bond length of

the carbonyl ligand is similar to each other in these two compounds, the difference in the Ru-C bond length is attributed to the trans-influence of the Ru-oxo σ bond. Also, the Ru-oxo bond is affected by the trans-influence of the carbonyl ligand; the Ru-O bond length (1.97 Å) of [Ru(Por)(CO)(O)]$^-$ **2D**$^-$ is considerably longer than the typical Ru-O distance (1.70 ~ 1.77 Å).[30]

Here, we will discuss the electronic structure of [Ru(Por)(CO)] to make comparison with [Ru(Por)(CO)(O)]$^-$. Frontier orbitals of **1S** are the π and π* MOs of the porphyrin ring, as shown in Figure 2(A). Ru d_{xy} (91) orbital is found at somewhat lower energy of -6.15 eV than Ru d_{xz} (92) and d_{yz} (93) orbitals (-5.99 eV), where in parenthesis is the orbital number counted from the lowest energy orbital. Ru d_{xz} (92) and d_{yz} (93) orbitals are doubly occupied, while Ru d_z^2 (98) and $d_{x^2-y^2}$ (104) orbitals are unoccupied; the latter exists at much higher energy of +0.52 eV. These occupations of d orbitals indicate that the Ru center takes +II oxidation state with the d^6 electron configuration in **1S**. Complexes **1T**, **1D**$^+$, and **1D**$^-$ were calculated with the same method. In **1T**, unpaired electrons occupy the π and π* MOs of the porphyrin ring. In **1D**$^+$ and **1D**$^-$, unpaired electron occupies the π and π* MOs, respectively. Based on these results, it is concluded that the Ru center keeps +II oxidation state in all these species. The oxidation state of the Ru center is also investigated in more detail by the CASSCF method, which will be discussed in the next section.

For the investigation of the oxidation state of the Ru center in [Ru(Por)(CO)(O)]$^-$ **2D**$^-$, we analyzed natural orbitals calculated by the UDFT(B3PW91)/BS-II method. Natural orbitals **φ$_1$**, **φ$_2$**, and **φ$_3$** are localized on the Ru d_{xy}, d_{xz}, and d_{yz} orbitals, respectively, and **φ$_7$** and **φ$_8$** are localized on the Ru d_z^2 and $d_{x^2-y^2}$ orbitals, respectively, as shown in Figure 2(B). The occupation number is about 2.0 for **φ$_1$** to **φ$_5$**, but nearly 0 for **φ$_7$** and **φ$_8$**. These occupation numbers indicate that the Ru center takes +II oxidation state bearing d^6 electron configuration. The natural orbital **φ$_6$** is localized on the p_π orbital of the oxo ligand into which the Ru d_π orbital moderately mixes in an anti-bonding way. The occupation number of **φ$_6$** is 1.0. This

natural orbital is consistent with the total spin populations which are 0.95, 0.01, and 0.04 e on the oxo ligand, the porphyrin ring, and the Ru center, respectively; in other words, the $\boldsymbol{\varphi_6}$ almost determines the spin distribution in $[Ru(Por)(CO)(O)]^-$. NBO electron and spin populations shown in Table 2 indicate the presence of the considerably strong charge transfer (CT) from the oxo ligand to the Ru center. Apparently, the NBO charge of the oxo ligand in $\mathbf{2D}^-$ is much less negative than -1.0, indicating that the charge transfer occurs from the oxo ligand to the Ru center. As a result, the positive charge of the Ru center is somewhat smaller in $\mathbf{2D}^-$ than in **1S**. Also, the negative charge of the porphyrin ring is considerably larger and the positive charge of CO is considerably smaller in $\mathbf{2D}^-$ than in **1S**. These results indicate that the CT from the oxo ligand suppresses the CTs from the porphyrin ring and the CO to the Ru center. Because the spin population is almost localized on the oxo ligand, it is likely that these CTs occur via the σ-bonding interaction. Actually, the d_σ-p_σ anti-bonding overlap between the Ru center and the oxo ligand is observed in $\boldsymbol{\varphi_7}$. Its bonding counterpart is observed in occupied orbitals; see $\boldsymbol{\varphi_4}$ in Figure 2(B). In the $\boldsymbol{\varphi_4}$, the oxo p_σ orbital overlaps well with the Ru d_z^2 orbital, with which the CO lone pair also overlaps in an anti-bonding way. These orbital mixings indicate that the σ-bonding interaction between the Ru d_z^2 and the oxo p_σ orbitals weakens the bonding interaction between the Ru d_z^2 and the CO lone pair orbitals.

At the end of this section, we wish to mention the reason why the $\boldsymbol{\varphi_6}$ becomes SOMO: The Ru $d_{x^2-y^2}$ and d_z^2 orbitals are destabilized in energy by the anti-bonding overlaps with the N none pair orbitals of the porphyrin ring and the CO lone pair orbitals, respectively. The oxo p_π orbital exists at much higher energy than the Ru d_{xz} and d_{yz} orbitals. Considering them, the orbital energy diagram for $\mathbf{2D}^-$ is schematically shown in Figure 2(C). The $\boldsymbol{\varphi_6}$ mainly consists of the oxo p_π orbital into which the Ru d_{xz} mixes in an anti-bonding way. The $\boldsymbol{\varphi_2}$ is its bonding counterpart mainly consisting of the Ru d_{xz} orbital. Because seven electrons occupy these MOs, the $\boldsymbol{\varphi_6}$ becomes SOMO. In these MOs, we must consider such eleven electrons as six electrons on the Ru center and five electrons on the oxo ligand. Of those eleven electrons,

Table 1. The four largest weight CSFs of CASSCF calculations [a)]

Complex	Spin state	CSF [b,c)]				Oxidation state of Ru	Weight (%)
		a_1	b_1	a_2	b_2		
[Ru(Por)(CO)]	**1S**	$\varphi_1^2\varphi_2^2\varphi_3^2\varphi_4^0\varphi_5^0$	$\varphi_6^2\varphi_7^0\varphi_8^0$	$\varphi_9^2\varphi_{10}^2\varphi_{11}^0$	$\varphi_{12}^2\varphi_{13}^0\varphi_{14}^0$	+II	85.66
		$\varphi_1^u\varphi_2^2\varphi_3^2\varphi_4^0\varphi_5^0$	$\varphi_6^2\varphi_7^0\varphi_8^d$	$\varphi_9^u\varphi_{10}^2\varphi_{11}^0$	$\varphi_{12}^2\varphi_{13}^0\varphi_{14}^d$	+II	1.75
		$\varphi_1^2\varphi_2^2\varphi_3^u\varphi_4^0\varphi_5^d$	$\varphi_6^2\varphi_7^0\varphi_8^0$	$\varphi_9^2\varphi_{10}^2\varphi_{11}^0$	$\varphi_{12}^u\varphi_{13}^d\varphi_{14}^0$	+I	0.82
		$\varphi_1^2\varphi_2^2\varphi_3^u\varphi_4^0\varphi_5^d$	$\varphi_6^u\varphi_7^d\varphi_8^0$	$\varphi_9^2\varphi_{10}^2\varphi_{11}^0$	$\varphi_{12}^2\varphi_{13}^0\varphi_{14}^0$	+I	0.82
	1T	$\varphi_2^2\varphi_3^2\varphi_1^2\varphi_4^0\varphi_5^0$	$\varphi_6^2\varphi_8^u\varphi_7^0$	$\varphi_{10}^2\varphi_9^u\varphi_{11}^0$	$\varphi_{12}^2\varphi_{13}^0\varphi_{14}^0$	+II	89.40
		$\varphi_2^2\varphi_3^2\varphi_1^u\varphi_4^0\varphi_5^0$	$\varphi_6^2\varphi_8^0\varphi_7^0$	$\varphi_{10}^2\varphi_9^2\varphi_{11}^0$	$\varphi_{12}^2\varphi_{13}^u\varphi_{14}^0$	+II	0.97
		$\varphi_2^2\varphi_3^u\varphi_1^2\varphi_4^0\varphi_5^d$	$\varphi_6^u\varphi_8^u\varphi_7^d$	$\varphi_{10}^2\varphi_9^u\varphi_{11}^0$	$\varphi_{12}^2\varphi_{13}^0\varphi_{14}^0$	+I	0.76
		$\varphi_2^2\varphi_3^u\varphi_1^2\varphi_4^0\varphi_5^d$	$\varphi_6^2\varphi_8^u\varphi_7^0$	$\varphi_{10}^2\varphi_9^u\varphi_{11}^0$	$\varphi_{12}^u\varphi_{13}^0\varphi_{14}^d$	+0	0.63
$[Ru(\cdot Por)(CO)]^+$	$\mathbf{1D^+}$	$\varphi_2^2\varphi_3^2\varphi_1^2\varphi_4^0\varphi_5^0$	$\varphi_6^2\varphi_8^0\varphi_7^0$	$\varphi_{10}^2\varphi_9^u\varphi_{11}^0$	$\varphi_{12}^2\varphi_{13}^0\varphi_{14}^0$	+II	88.80
		$\varphi_2^2\varphi_3^u\varphi_1^2\varphi_4^0\varphi_5^d$	$\varphi_6^u\varphi_8^d\varphi_7^0$	$\varphi_{10}^2\varphi_9^u\varphi_{11}^0$	$\varphi_{12}^2\varphi_{13}^0\varphi_{14}^0$	+I	0.54
		$\varphi_2^2\varphi_3^2\varphi_1^2\varphi_4^0\varphi_5^0$	$\varphi_6^u\varphi_8^d\varphi_7^0$	$\varphi_{10}^2\varphi_9^u\varphi_{11}^0$	$\varphi_{12}^u\varphi_{13}^d\varphi_{14}^0$	+II	0.50
		$\varphi_2^2\varphi_3^u\varphi_1^2\varphi_4^0\varphi_5^0$	$\varphi_6^2\varphi_8^0\varphi_7^d$	$\varphi_{10}^2\varphi_9^0\varphi_{11}^0$	$\varphi_{12}^2\varphi_{13}^0\varphi_{14}^u$	+II	0.47
$[Ru(\cdot Por)(CO)]^-$	$\mathbf{1D^-}$	$\varphi_2^2\varphi_3^2\varphi_1^2\varphi_4^0\varphi_5^0$	$\varphi_6^2\varphi_8^0\varphi_7^0$	$\varphi_{10}^2\varphi_9^2\varphi_{11}^0$	$\varphi_{12}^2\varphi_{13}^u\varphi_{14}^0$	+II	88.02
		$\varphi_2^2\varphi_3^2\varphi_1^u\varphi_4^0\varphi_5^0$	$\varphi_6^2\varphi_8^0\varphi_7^d$	$\varphi_{10}^2\varphi_9^u\varphi_{11}^0$	$\varphi_{12}^2\varphi_{13}^0\varphi_{14}^0$	+II	1.00
		$\varphi_2^2\varphi_3^d\varphi_1^2\varphi_4^0\varphi_5^u$	$\varphi_6^2\varphi_8^0\varphi_7^0$	$\varphi_{10}^2\varphi_9^2\varphi_{11}^0$	$\varphi_{12}^u\varphi_{13}^u\varphi_{14}^d$	+I	0.73
		$\varphi_2^2\varphi_3^d\varphi_1^2\varphi_4^0\varphi_5^u$	$\varphi_6^u\varphi_8^d\varphi_7^0$	$\varphi_{10}^2\varphi_9^2\varphi_{11}^0$	$\varphi_{12}^2\varphi_{13}^u\varphi_{14}^0$	+I	0.68
$[Ru(Por)(CO)(O)]^-$	$\mathbf{2D^-}$	$\varphi_2^2\varphi_3^2\varphi_1^2\varphi_4^0\varphi_5^0$	$\varphi_6^2\varphi_8^0\varphi_7^0$	$\varphi_{10}^2\varphi_9^2\varphi_{11}^0$	$\varphi_{12}^2\varphi_{15}^u\varphi_{13}^0\varphi_{14}^0$	+II	85.65
		$\varphi_2^2\varphi_3^2\varphi_1^u\varphi_4^0\varphi_5^0$	$\varphi_6^2\varphi_8^0\varphi_7^d$	$\varphi_{10}^2\varphi_9^u\varphi_{11}^0$	$\varphi_{12}^2\varphi_{15}^u\varphi_{13}^d\varphi_{14}^0$	+II	1.22
		$\varphi_2^2\varphi_3^u\varphi_1^2\varphi_4^0\varphi_5^d$	$\varphi_6^u\varphi_8^d\varphi_7^0$	$\varphi_{10}^2\varphi_9^2\varphi_{11}^0$	$\varphi_{12}^2\varphi_{15}^u\varphi_{13}^0\varphi_{14}^0$	+I	0.62
		$\varphi_2^2\varphi_3^2\varphi_1^2\varphi_4^0\varphi_5^0$	$\varphi_6^2\varphi_8^0\varphi_7^0$	$\varphi_{10}^2\varphi_9^0\varphi_{11}^0$	$\varphi_{12}^2\varphi_{15}^u\varphi_{13}^2\varphi_{14}^0$	+II	0.61

a) For these φ_1 to φ_{14} natural orbitals, see Figure A2 in Appendix. b) "u" and "d" denote the up-spin and down-spin electrons, respectively. c) a_1: φ_1 = Por π, φ_2 = Ru $4d_{xy}$, φ_3 = Ru-CO σ,φ_4 = Ru $4d_{xy}$', φ_5 = Ru 4 d_z^2; b_1: φ_6 = Ru $4d_{yz}$, φ_7 = Ru $4d_{yz}$', φ_8 = Por π*; a_2: φ_9 = Por π, φ_{10} = Por σ, φ_{11} = Ru $4d_{x^2-y^2}$; b_2: φ_{12} = Ru $4d_{xz}$, φ_{13} = Ru $4d_{xz}$', φ_{14} = Por π*, φ_{15} = oxo p_π*

three electrons occupy the $\boldsymbol{\varphi_5}$ and $\boldsymbol{\varphi_6}$. Because the $\boldsymbol{\varphi_5}$ and $\boldsymbol{\varphi_6}$ are degenerate in the C_{4v} symmetry, this occupation induces the Jahn-Teller distortion. As a result, the geometry of $\mathbf{2D^-}$ becomes C_{2v} symmetry, in which the $\boldsymbol{\varphi_6}$ and $\boldsymbol{\varphi_6}$ are non-degenerate and the $\boldsymbol{\varphi_6}$ becomes SOMO.

3.3.2 Reliability of Single-reference Wavefunction and the Oxidation State of the Ruthenium Center

Because metalloporphyrins often exhibit multi-configuration character, we investigated the electronic structures of [Ru(Por)(CO)] and $[Ru(Por)(CO)(O)]^-$ with the CASSCF method.[32]

Besides **1S**, four important species are involved in the catalytic cycle (see Scheme 1(A)); (i) **1T** which is formed through UV/Vis light irradiation, (ii) $\mathbf{1D}^{+}$ which is formed through the oxidation of **1T**, (iii) $\mathbf{2D}^{-}$ which is proposed as an active species for the olefin epoxidation, and (iv) $\mathbf{1D}^{-}$ which is formed through the epoxidation process. Their natural orbitals are shown in Figure A2 in Appendix. In **1S**, the wave function mainly consists of the configuration state function (CSF), [(Por π)^2(Ru $4d_{xy}$)^2(Ru-CO σ)^2(Ru $4d_{xz}$)^2(Por π)^2(Por σ)^2(Ru $4d_{yz}$)^2], as shown in Table 1. This CSF corresponds to the Ru^{II} state, whose contribution is 85.7 % of the total wave function. The second leading CSF consists of the combination of two π-π* excitations in the porphyrin ring. This CSF also corresponds to the Ru^{II} oxidation state. Because the third and fourth leading CSFs include the excitation from the Ru-CO σ MO to the Ru $4d_z^2$, these correspond to the Ru^{I} oxidation state. However, the weights of these CSFs are very small (1.6 %). Based on these results, it should be clearly concluded that the Ru center takes +II oxidation state in **1S**.

In **1T**, $\mathbf{1D}^{+}$, and $\mathbf{1D}^{-}$, the main CSF corresponds to the Ru^{II} oxidation state. Their contributions to the total CASSCF wave function are about 90 %, as summarized in Table 1. These results indicate that the multi-configuration character is small even in the triplet excited state, cation radical, and anion radical of [Ru(Por)(CO)], and that the Ru center of [Ru(Por)(CO)] has +II oxidation state in these species like in **1S**.

In $[Ru(Por)(CO)(O)]^{-}$ $\mathbf{2D}^{-}$, the main CSF is [(Por π)^2(Ru $4d_{xy}$)^2(Ru-CO σ)^2(Ru $4d_{xz}$)^2(Por π)^2(Por σ)^2(Ru $4d_{yz}$)^2(oxo p_π)^1], which also corresponds to the Ru^{II} oxidation state. Its weight is about 86 % of the total CASSCF wave function, as shown in Table 1. The natural orbitals show that unpaired electron is almost localized on the oxo ligand and that each of the d_{xy}, d_{xz} and d_{yz} orbitals possess nearly two electrons, as shown in Figure A2. This result is consistent with the fact that the main CSF corresponds to the Ru(II) d^6 electron configuration. It is noted also that the UDFT-calculated natural orbitals are essentially the same as the CASSCF-calculated natural orbitals, as seen in Figures 2(B) and A2, suggesting that the DFT

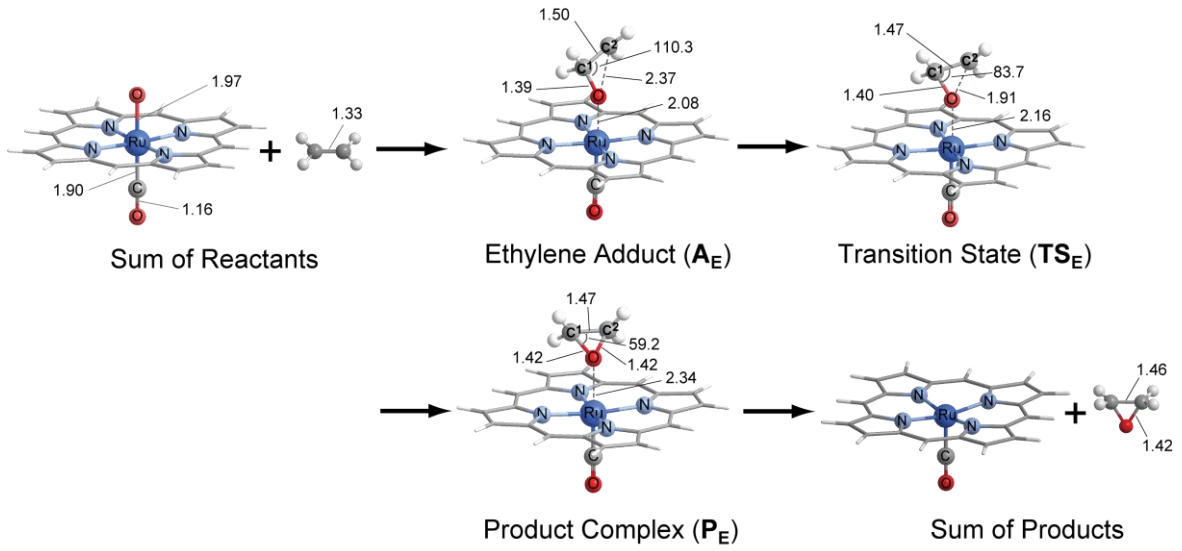

Figure 3. Optimized geometries of reactants ($[Ru(Por)(CO)(O)]^-$ and ethylene), ethylene adduct ($\mathbf{A_E}$), transition state ($\mathbf{TS_E}$), product complex ($\mathbf{P_E}$), and products ($[Ru(Por)(CO)]^-$ and epoxide) for the epoxidation reaction of ethylene

method presents reliable results of the ruthenium porphyrin complexes. Considering above results, we will employ the DFT method for the investigation of the olefin epoxidation process.

3.3.3 Olefin Epoxidation by $[Ru(Por)(CO)(O)]^-$

The approach of ethylene to $[Ru(Por)(CO)(O)]^-$ $\mathbf{2D^-}$ leads to formation of an ethylene adduct $[Ru(Por)(CO)(O)(C_2H_4)]^-$ $\mathbf{A_E}$. In $\mathbf{A_E}$, the C^1-O distance (1.39 Å) is much different from the C^2-O distance (2.37 Å), as shown in Figure 3; see Figure 3 for C^1 and C^2 atoms. These results indicate that $\mathbf{A_E}$ is not an oxene intermediate. It is noted that the Ru-O bond is somewhat elongated by 0.11 Å when going from $[Ru(Por)(CO)(O)]^-$ to $\mathbf{A_E}$. As will be discussed below, this structural change is explained by the CT from the π orbital of ethylene to the Ru-O d_π-p_π anti-bonding orbital. Starting from $\mathbf{A_E}$, the C^2 atom approaches the oxo ligand to reach transition state $\mathbf{TS_E}$. In $\mathbf{TS_E}$, the C^1-O and C^2-O bond lengths are still considerably different; R(C^1-O) = 1.40 Å and R(C^2-O) = 1.92 Å. In other words, $\mathbf{TS_E}$ does not possess the oxene character like $\mathbf{A_E}$. After $\mathbf{TS_E}$, the C^2 atom further approaches the oxo ligand

(A) Potential energy curves

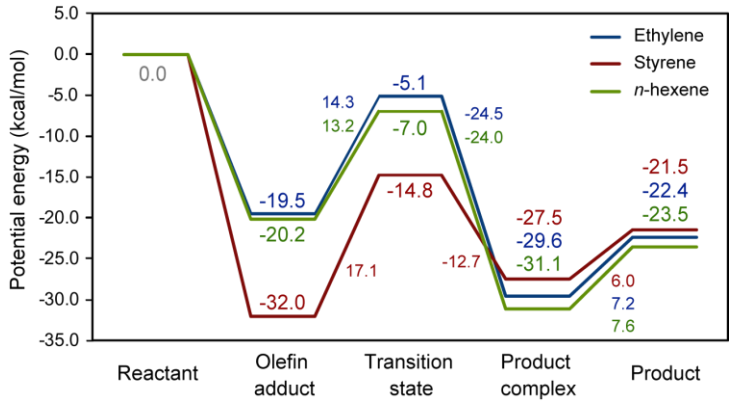

(B) Gibbs free energy curves

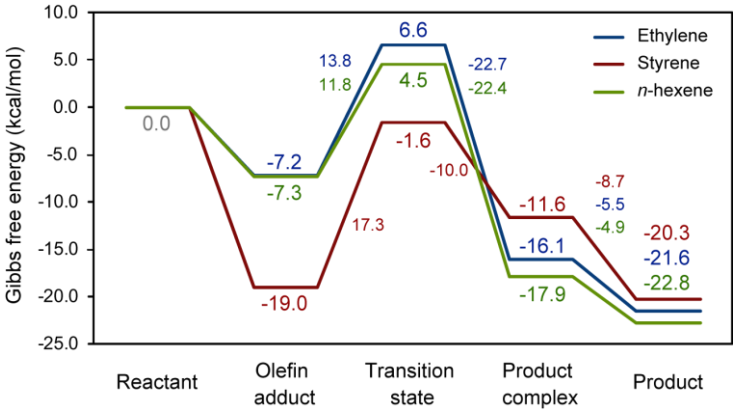

Figure 4. Potential energy (A) and Gibbs free energy (B) profile of the epoxidation of ethylene, styrene, and *n*-hexene.

to form a product complex $\mathbf{P_E}$. In $\mathbf{P_E}$, the C^1-O bond distance is almost the same as the C^2-O one and the Ru-O bond distance is still short in $\mathbf{P_E}$; R(C^1-O) = R(C^2-O) = 1.42 Å and R(Ru-O) = 2.34 Å, indicating that epoxide is almost formed but it still interacts with the Ru center through the O atom.

Potential (ΔE) and Gibbs energy changes (ΔG^0) in the epoxidation reaction are shown in Figure 4. The reaction energies ΔE_R and $\Delta G^0{}_R$, which are defined as energy differences between the reactant and the product, are calculated to be -22.4 and -21.6 kcal/mol, respectively, where the negative value represents that the reaction is exothermic. The activation barrier in the potential energy (E_a) and Gibbs energy ($\Delta G^{0‡}$) is defined as energy difference between $\mathbf{A_E}$ and $\mathbf{TS_E}$, because $\mathbf{A_E}$ is the most stable species before $\mathbf{TS_E}$. They are

Table 2. NBO charges and spin populations [a] of important species in olefin epoxidation reactions [b]

		Ru	O	Por	CO	C^1	C^2	C^2 Substituent	Olefin Total
	[Ru(Por)(CO)] (**1S**)	0.44	—	-0.64	0.20	—	—	—	—
	$[Ru(Por)(CO)(O)]^-$ ($\mathbf{2D^-}$)	0.35	-0.53	-0.87	0.05	—	—	—	—
		(0.04)	(0.95)	(-0.01)	(0.02)	—	—	—	—
Ethylene epoxidation	$\mathbf{A_E}$	0.35	-0.79	-0.83	0.10	-0.11	-0.36	0.15	0.16
		(0.00)	(-0.11)	(0.00)	(0.00)	(0.03)	(-0.96)	(0.00)	(-0.89)
	$\mathbf{TS_E}$	0.33	-0.61	-1.30	0.17	-0.10	-0.29	0.20	0.41
		(0.00)	(-0.12)	(-0.60)	(0.00)	(0.01)	(-0.30)	(0.01)	(-0.28)
	$\mathbf{P_E}$	0.33	-0.54	-1.62	0.19	-0.09	-0.09	0.19	0.65
		(-0.02)	(0.00)	(-0.98)	(0.00)	(0.00)	(0.00)	(0.00)	(0.00)
Styrene epoxidation	$\mathbf{A_S}$	0.35	-0.79	-0.81	0.11	-0.08	-0.12	-0.21	0.15
		(0.00)	(-0.06)	(0.00)	(0.00)	(0.03)	(-0.62)	(-0.33)	(-0.93)
	$\mathbf{TS_S}$	0.33	-0.61	-1.26	0.18	-0.07	-0.04	-0.16	0.37
		(-0.01)	(-0.09)	(-0.58)	(0.00)	(0.00)	(-0.14)	(-0.24)	(-0.32)
	$\mathbf{P_S}$	0.33	-0.54	-1.62	0.19	-0.08	0.07	-0.03	0.64
		(-0.02)	(0.00)	(-0.98)	(0.00)	(0.00)	(0.00)	(0.00)	(0.00)
n-hexene epoxidation	$\mathbf{A_H}$	0.35	-0.80	-0.82	0.10	-0.10	-0.16	-0.08	0.17
		(0.00)	(-0.09)	(0.00)	(0.00)	(0.03)	(-0.91)	(-0.04)	(-0.90)
	$\mathbf{TS_H}$	0.33	-0.63	-1.30	0.17	-0.09	-0.07	-0.03	0.43
		(0.00)	(-0.06)	(-0.60)	(0.00)	(0.01)	(-0.35)	(-0.02)	(-0.34)
	$\mathbf{P_H}$	0.33	-0.55	-1.62	0.19	-0.09	0.09	0.00	0.66
		(-0.02)	(0.00)	(-0.98)	(0.00)	(0.00)	(0.00)	(0.00)	(0.00)

a) In parentheses are NBO spin populations. b) At the B3PW91/BS-II level.

calculated to be 14.3 and 13.8 kcal/mol, respectively. It should be noted that the difference between E_a and $\Delta G^{0\ddagger}$ is small, because this step is an unimolecular process. These moderate activation barriers are consistent with the experimental fact that the epoxidation reaction easily occurs in the wide range of temperature.[16] Though $\mathbf{P_E}$ is more stable than $\mathbf{A_E}$ and the reactant, the sum of ethylene oxide and [Ru(Por)(CO)] is less stable than $\mathbf{P_E}$ on the potential energy surface. This is because epoxide coordinates with the Ru center in $\mathbf{P_E}$. However, the Gibbs energy change is negative upon epoxide dissociation from $[Ru(Por)(CO)]^-$, because the dissociation of epoxide from the Ru center increases entropy.

In order to give clear understanding of the ethylene epoxidation reaction, we

(A) The Formation of the $\varphi_{oxo-\pi}$

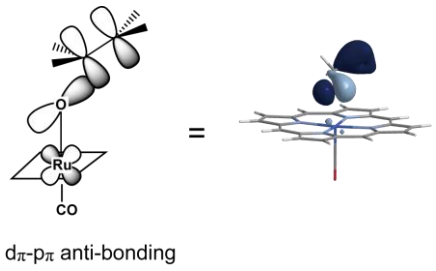

(B) The Formation of the φ_{SOMO}

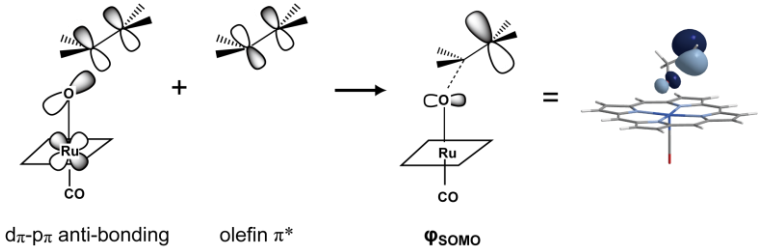

(C) Orbital energy diagrams of $[Ru(Por)(CO)(O)]^-$ and ethylene interaction

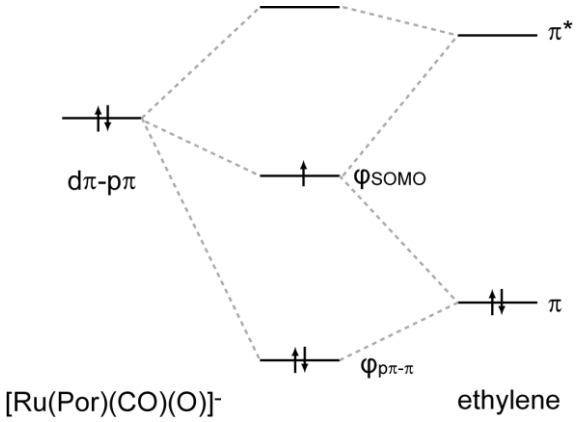

Scheme 2

investigated atomic and spin populations along the reaction, where NBO electron and spin populations are calculated with the UDFT(B3PW91)/BS-II method. As shown in Table 2, the electron population of ethylene decreases by 0.16 e but that of the oxo ligand increases by 0.25 e when going from [Ru(Por)(CO)(O)] to $\mathbf{A_E}$. Note that the electron population of Ru little changes upon the formation of $\mathbf{A_E}$. These population changes indicate that the ethylene interacts with $[Ru(Por)(CO)(O)]^-$ through the CT from its π orbital to the oxo ligand. The C^2

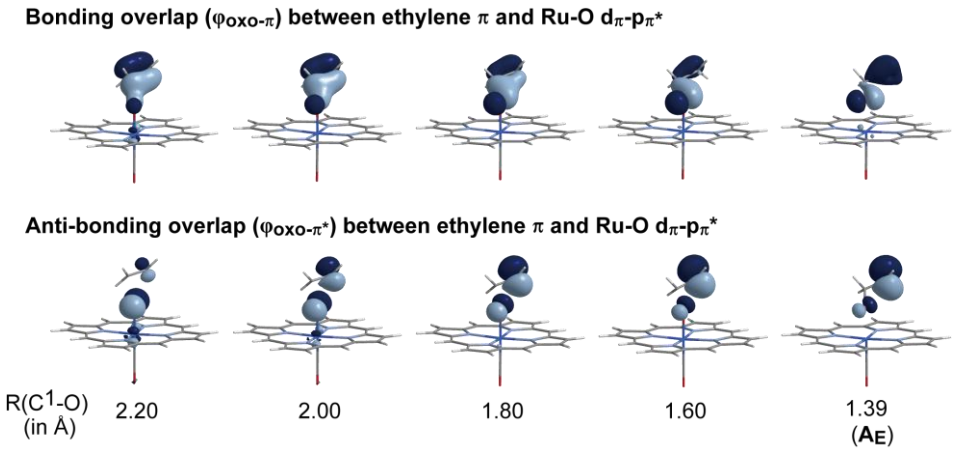

Figure 5. Changes in UDFT-calculated natural orbital upon the ethylene coordination to [Ru(Por)(CO)(O)]$^-$ **2D**$^-$.

atomic charge becomes considerably negative (-0.36 e) and the spin population of the C^2 atom (0.96 e) considerably increases. On the other hand, the C^1 atomic charge is moderately negative (-0.11 e) and its spin population is negligibly small (-0.03 e). These results indicate that not only the CT but also the polarization occurs in the ethylene moiety.

To elucidate why the spin population increases not in the C^1 atom but in the C^2 atom by the CT, we investigated natural orbitals calculated at the UDFT(B3PW91)/BS-II level with several C^1-O distances and found two important natural orbitals, $\boldsymbol{\varphi_{oxo\text{-}\pi}}$ and $\boldsymbol{\varphi_{oxo\text{-}\pi}^*}$; see Figure 5. The occupation number of $\boldsymbol{\varphi_{oxo\text{-}\pi}^*}$ is close to one, while that of $\boldsymbol{\varphi_{oxo\text{-}\pi}}$ is close to two. Thus, the spin distribution is mainly determined by $\boldsymbol{\varphi_{oxo\text{-}\pi}^*}$. At a long C^1-O distance, $\boldsymbol{\varphi_{oxo\text{-}\pi}}$ mainly consists of the π orbital of ethylene, but it changes to the C^1-O σ-bonding MO in the ethylene adduct $\mathbf{A_E}$. The $\boldsymbol{\varphi_{oxo\text{-}\pi}^*}$ is localized on the oxo p_π orbital at a long C^1-O distance, but the contribution of the oxo p_π orbital considerably decreases and that of the p orbital of the C^2 atom considerably increases in $\mathbf{A_E}$. These changes in $\boldsymbol{\varphi_{oxo\text{-}\pi}}$ and $\boldsymbol{\varphi_{oxo\text{-}\pi}^*}$ are interpreted, as follows: i) The ethylene π orbital overlaps with the oxo p_π orbital in a bonding way to form the $\boldsymbol{\varphi_{oxo\text{-}\pi}}$ orbital, as shown in Scheme 2(A). The π orbital also overlaps with the oxo p_π orbital in an anti-bonding way to form SOMO $\boldsymbol{\varphi_{oxo\text{-}\pi}^*}$, into which ethylene π* orbital mixes in a bonding way with the oxo p_π orbital, as shown in Scheme 2(B), because the π* orbital is at

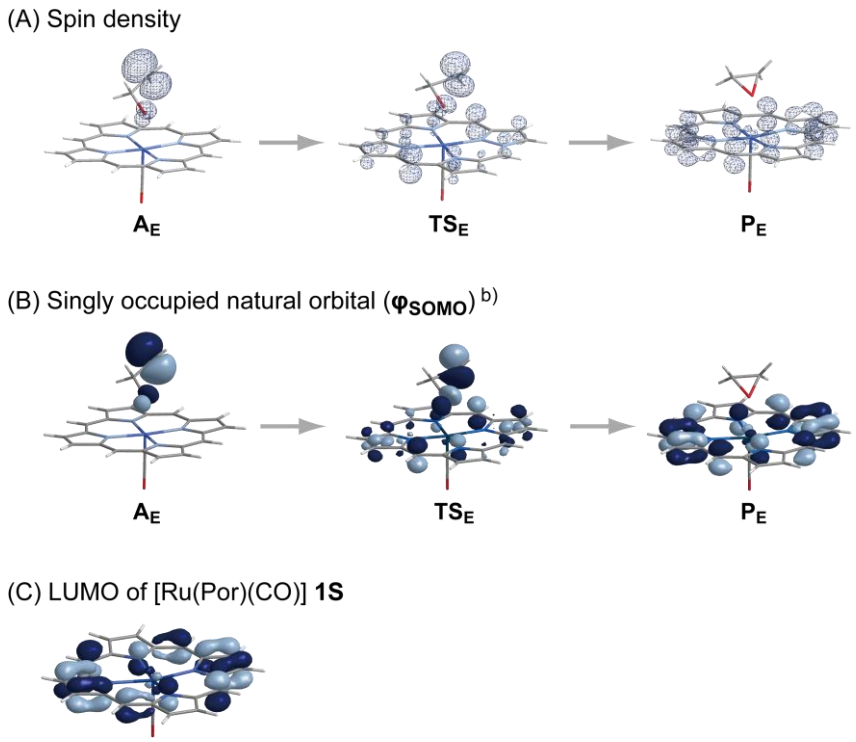

Figure 6. UDFT-calculated spin density and natural orbitals of $\mathbf{A_E}$, $\mathbf{TS_E}$, and $\mathbf{P_E}$. [a] a) UDFT(B3PW91)/BS-II method was employed. b) see ref.33.

higher energy than the oxo p_π orbital; see Scheme 2(C). This mixing of the π^* orbital considerably decreases the contribution of C^1 p_π orbital and considerably increases that of the C^2 p_π orbital, as shown in Scheme 2(B). As a result, the C^2 atom becomes considerably negative and the spin population considerably increases on the C^2 atom.

For the epoxidation of olefin, several intermediates and transition states were proposed, as shown in Scheme 1(B).[10] From our computational results, the concerted oxene-insertion mechanism is ruled out, as mentioned above, because the symmetric geometrical features of oxene are not observed at all in the optimized structure of $\mathbf{TS_E}$. Next question is which of the carbocation mechanism and the carboradical one is plausible. We further analyzed the electronic structures of $\mathbf{A_E}$, $\mathbf{TS_E}$, and $\mathbf{P_E}$ based on spin density and UDFT natural orbitals shown in Figure 6. In both $\mathbf{A_E}$ and $\mathbf{TS_E}$, considerably large spin density is observed on the C^2 atom, and moderately large spin density is found on the oxo ligand, as shown in Figure 6(A).

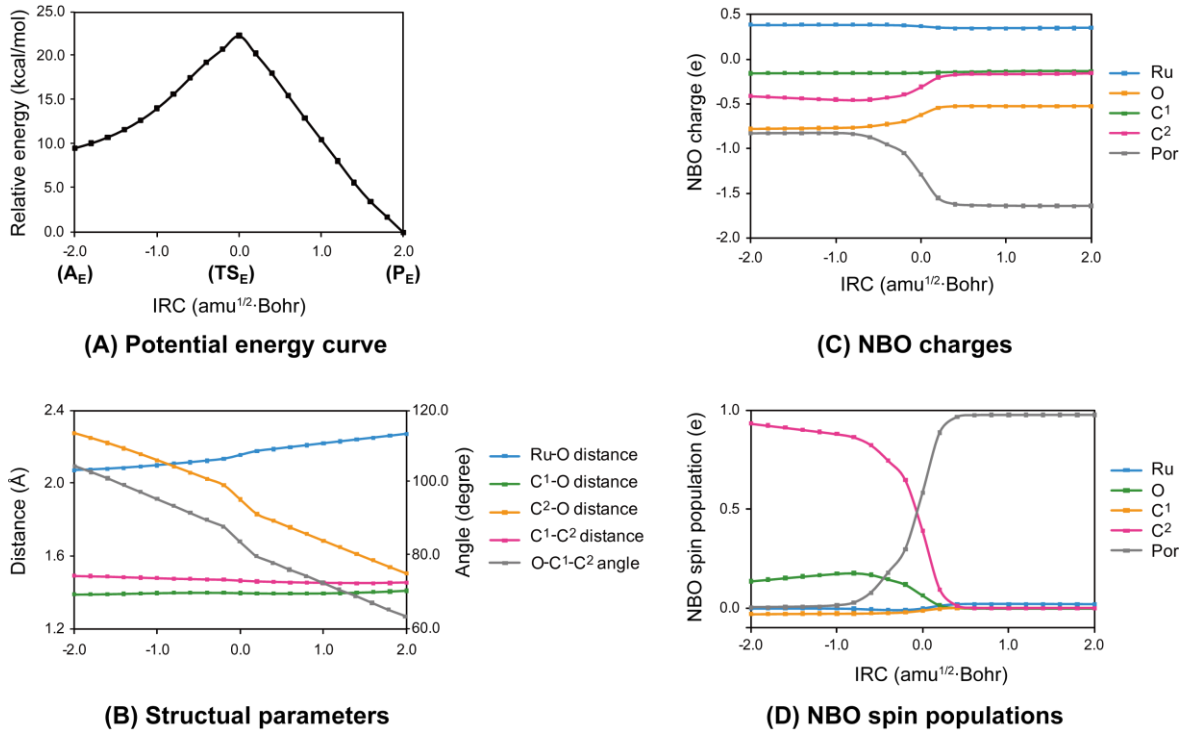

Figure 7. Potential energy curve (A), structural parameters [a)] (B), NBO charges (C), and NBO spin populations (D) along intrinsic reaction coordinate (IRC) for the ethylene epoxidation. a) see Figure 3 for the C^1 and C^2 atoms.

These results lead to the conclusion that not the carbocation mechanism but the carboradical mechanism is the most plausible. Also, it should be noted that the spin population of the C^2 atom considerably decreases when going to $\mathbf{P_E}$ from $\mathbf{A_E}$ through $\mathbf{TS_E}$, while that of the porphyrin ring considerably increases; the details of this change in spin distribution will be discussed later in this section.

The changes in geometry and electronic structure along the intrinsic reaction coordinate (IRC) provide clear understanding, as shown in Figure 7. The Ru-O, C^1-O, C^2-O, and C^1-C^2 bond distances and the O-C^1-C^2 angle are plotted against IRC in Figure 7(B). The significantly large geometrical changes are observed in the O-C^1-C^2 angle and the C^2-O distance; the O-C^1-C^2 angle considerably decreases to about 60° from about 100° and the C^2-O distance becomes shorter to 1.5 Å from 2.3 Å. On the other hand, the Ru-O and C^1-O distances moderately change. Because the C^2-O distance decreases concomitantly with the

decrease in the O-C^1-C^2 angle, it is concluded that the decrease of the C^2-O distance is the most important geometrical change in this reaction.

The NBO negative charges of the C^2 and O atoms somewhat decrease around $\mathbf{TS_E}$, while the NBO negative charge of the C^1 atom little changes in the reaction, as shown in Figure 7(C). On the other hand, the NBO negative charge of the porphyrin ring suddenly increases around $\mathbf{TS_E}$. The spin population on the C^2 atom suddenly decreases around the $\mathbf{TS_E}$ and finally disappears in $\mathbf{P_E}$, as shown in Figure 7(D). Consistent with this change, the spin population on the porphyrin ring considerably increases around $\mathbf{TS_E}$, and finally reaches about 1.0 e in $\mathbf{P_E}$. The spin population of the oxo ligand somewhat decreases around $\mathbf{TS_E}$, though the spin populations of the Ru and C^1 atoms little change. These results suggest that the CT from the ethylene moiety to the porphyrin ring occurs concomitantly with the transfer of unpaired electron from the C^2 atom to the porphyrin ring around $\mathbf{TS_E}$. As we have seen in the previous section, UDFT-calculated natural orbitals are useful for understanding the spin transfer process. One natural orbital $\boldsymbol{\varphi_{SOMO}}$ possesses occupation number close to 1.0 but other natural orbitals possess occupation number close to 2.0,[33] as mentioned above. These results indicate that the spin distribution is mainly determined by $\boldsymbol{\varphi_{SOMO}}$. This natural orbital contains the anti-bonding interaction between the C^2 and O atoms in $\mathbf{A_E}$ and $\mathbf{TS_E}$; see Figure 6(B). However, this anti-bonding interaction is no longer observed in $\mathbf{P_E}$ but the $\boldsymbol{\varphi_{SOMO}}$ is localized on the porphyrin ring in $\mathbf{P_E}$ (Figure 6(B)). In other words, unpaired electron transfers from the C^2 atom to the porphyrin ring when going from $\mathbf{A_E}$ to $\mathbf{P_E}$. The $\boldsymbol{\varphi_{SOMO}}$ in $\mathbf{P_E}$ is essentially the same as the π^* orbital (LUMO) of the porphyrin ring, as compared in Figure 6(B) and (C). Thus, it is concluded that the porphyrin π^* orbital plays important roles to receive unpaired electron from the olefin moiety.

The overall electronic process of the ethylene epoxidation is summarized based on the above discussion, as follows: In $\mathbf{A_E}$, the SOMO of $\mathbf{2D^-}$ overlaps with the π orbital of ethylene in a bonding way, as shown in Scheme 2(A), to form the O-C^1 σ-bond. Simultaneously, the

unpaired electron is localized on the C^2 atom by the orbital mixing of Scheme 2(B). Around **TS_E**, the O-C^2 σ-bond should be formed to complete the olefin epoxidation process. This bond is formed by the bonding overlap between the oxo p_π orbital and the p orbital of the C^2 atom. Because the C^2-O anti-bonding MO is singly occupied, this electron must move to the porphyrin π* orbital to complete the C^2-O σ-bond formation. Note that spin population of the Ru center little changes during the reaction, as shown in Figure 7(D). This is because the LUMO of the ruthenium porphyrin mainly consists of the porphyrin π* orbitals but little of the Ru orbitals; for example, see 96^{th} MO of Figure 2(A). Thus, not the Ru d orbital but the porphyrin π* orbital directly receives electron and spin populations from the C^2 atom.

3.3.4 Substrate Dependence on the Olefin Epoxidation Process

From the synthetic point of view, the catalyst must be applied to various substrates. In this regard, $[Ru(Por)(CO)(O)]^-$ is an excellent catalyst because this can be applied to epoxidation of a variety of substrates, as reported experimentally.[16]

To elucidate the reason why $[Ru(Por)(CO)(O)]^-$ can be applied to epoxidation of various substrates, we investigated the epoxidation reactions of *n*-hexene and styrene. In epoxidation reactions of *n*-hexene and styrene, we named their olefin adducts as **A_H** and **A_S**, their transition states as **TS_H** and **TS_S**, and their product complexes as **P_H** and **P_S**, respectively.

Geometries of **A_H** and **A_S** are similar to that of **A_E**; for instance, the Ru-O distance is 2.09, 2.09, and 2.08 Å for **A_H**, **A_S**, and **A_E**, respectively; see Figure A2 in Appendix. The O-C^1-C^2 angle is also similar in these olefin adducts; 110.1, 110.0, and 110.3° for **A_H**, **A_S**, and **A_E**, respectively. Geometries of **TS_H** and **TS_S** are similar to that of **TS_E** except for rather smaller O-C^1-C^2 angle of **TS_S** (78.4°) than those of the other two transition states **TS_H** (84.6°) and **TS_E** (83.7°). This feature indicates that **TS_S** is moderately more product-like than the other two transition states **TS_E** and **TS_H**. In **P_H** and **P_S**, the epoxide formation is almost completed, as clearly indicated by the O-C^1-C^2 angle (60.0 °) and the C^2-O distance (2.34 Å

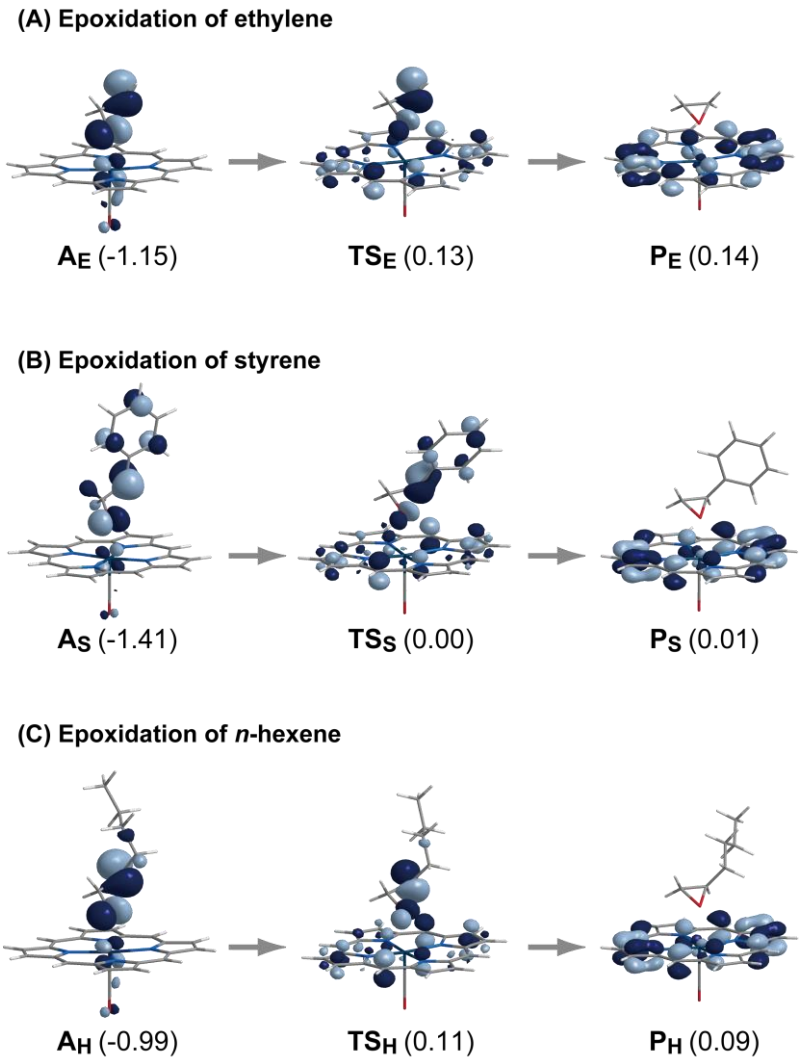

Figure 8. SOMOs [a)] of olefin adducts, transition states, and product complexes for the epoxidation of ethylene, styrene, and *n*-hexene (UB3PW91/BS-II). a) In parentheses are orbital energies in eV.

and 2.33 Å for $\mathbf{P_H}$ and $\mathbf{P_S}$, respectively). The Ru-O distance is little different in these product complexes; 2.33, 2.34, and 2.34 Å for $\mathbf{P_H}$, $\mathbf{P_S}$, and $\mathbf{P_E}$, respectively. These results indicate that the interaction between the epoxide and the $[Ru(Por)(CO)]^-$ moiety does not depend on the nature of substrate very much.

Potential and Gibbs energy changes of epoxidations of *n*-hexene and styrene are shown in Figure 4, together with those of the ethylene epoxidation. In both of potential and Gibbs energy changes, the largest difference is found in the olefin adduct with the ruthenium

porphyrin complex; the stabilization energy of the olefin adduct is -19.5, -32.0, and -20.2 kcal/mol for $\mathbf{A_E}$, $\mathbf{A_S}$, and $\mathbf{A_H}$, respectively. However, the E_a value is not different very much among the reactions of ethylene (14.3 kcal/mol), styrene (17.1 kcal/mol), and *n*-hexene (13.2 kcal/mol).

As discussed above, the formation of $\mathbf{A_E}$, $\mathbf{A_H}$, and $\mathbf{A_S}$ can be understood by the CT from the olefin π orbital to the oxo p_π orbital. Thus, the electron and spin populations of the olefin and Ru-O moieties would be helpful to understand the reason why the stabilization energy of $\mathbf{A_S}$ is much larger than those of $\mathbf{A_H}$ and $\mathbf{A_E}$. Upon formation of these olefin adducts, NBO electron population of the olefin moiety decreases by 0.15, 0.15, and 0.17 e for ethylene, styrene and *n*-hexene, respectively, as shown in Table 2, against our expectation that the CT is stronger in $\mathbf{A_S}$ than in $\mathbf{A_E}$ and $\mathbf{A_H}$. Consistent with the similar change in the electron population of the olefin moiety, the NBO population of the Ru-O moiety increases similarly by 0.27 e, 0.27 e, and 0.26 e upon $\mathbf{A_E}$, $\mathbf{A_H}$, and $\mathbf{A_S}$ formations, respectively. On the other hand, the spin population is significantly different among them; in $\mathbf{A_S}$, the spin population of the C^2 atom (+0.60 e) is much smaller than in $\mathbf{A_E}$ (+0.95 e) and $\mathbf{A_H}$ (+0.93 e), while the spin population of the phenyl group is much larger than those of the substituents on the C^2 atom of ethylene and *n*-hexene; see spin density of $\mathbf{A_E}$, $\mathbf{A_S}$, and $\mathbf{A_H}$ shown in Figure 8. Apparently, unpaired electron is delocalized on the phenyl group in $\mathbf{A_S}$, while such delocalization does not occur in $\mathbf{A_E}$ and $\mathbf{A_H}$.

Both of the large stabilization energy and large spin delocalization of $\mathbf{A_S}$ are easily interpreted in terms of the π and π* orbitals of styrene. Styrene π orbital is at higher energy than those of ethylene and *n*-hexene by almost 1.0 eV, and styrene π* orbital is at lower energy than those of ethylene and *n*-hexene by almost 1.4 eV, as shown in Figure A4 in Appendix. This is because the phenyl π and π* orbitals mix with the π and π* orbitals of the C=C double bond, as shown in Figure 8. As a result, the π and π* orbitals of styrene strongly interact with the oxo p_π orbital than the π and π* orbitals of the other olefins, which yields the

large energy stabilization of the styrene adduct. Because not only π but also π* participates in the interaction with the oxo p_π orbital, the CT from styrene to the oxo ligand is somewhat compensated by the CT from the oxo ligand to styrene, leading to the similar NBO charges in $\mathbf{A_E}$, $\mathbf{A_S}$, and $\mathbf{A_H}$, in spite of large stabilization energy of $\mathbf{A_S}$. The presence of conjugation between the phenyl group and the C=C double bond in styrene also induces more spin delocalization to the phenyl group than to the hydrogen atom and the alkyl group.

It is of considerable interest to clarify the reason why the E_a of the styrene epoxidation is not very large despite of the very large stabilization energy of $\mathbf{A_S}$. In $\mathbf{TS_S}$, the spin delocalization to the phenyl group is still considerably large, as indicated by the spin population in Table 2. The SOMO participates in this delocalization, as discussed above. The SOMO of $\mathbf{TS_S}$ shown in Figure 8 clearly displays the bonding interaction between the phenyl π* and the C^2 p_π orbitals. Because the C^2 p_π orbital overlaps with the oxo p orbital in an anti-bonding way in this SOMO, the bonding interaction between the phenyl π* and C^2 p_π orbitals contributes to the stabilization of $\mathbf{TS_S}$. On the other hand, such bonding interaction is absent in the SOMOs of $\mathbf{TS_E}$ and $\mathbf{TS_H}$; see Figure 8. In other words, the presence of the phenyl π* orbitals stabilized both of styrene adduct $\mathbf{A_S}$ and the transition state $\mathbf{TS_S}$. As a result, E_a of the styrene epoxidation is not very large. These results suggest that the olefin epoxidation reaction catalyzed by [Ru(Por)(CO)] occurs with similar E_a for versatile olefins.

3.4 Conclusions

In the present work, the olefin epoxidation catalyzed by [Ru(TMP)(CO)] is investigated theoretically. The CASSCF and DFT methods provide similar electronic structures of important ruthenium porphyrin species, indicating that the DFT method can be applied to this epoxidation reaction. Based on our computational results, the electronic process of the olefin epoxidation reaction is clearly disclosed, as follows: i) Both the olefin adduct [Ru(Por)(CO)(olefin)] and the transition state have unsymmetrical geometries with respect to

the Ru center and two C atoms of the olefin. This means that the reaction does not occur via concerted oxene insertion mechanism. ii) In the olefin adduct and the transition state, unpaired electron is localized on one C atom of the olefin. This clearly shows that the epoxidation reaction undergoes via carboradical mechanism. iii) Unpaired electron transfers from the olefin C atom to the porphyrin ring around the transition state. iv) The substrate dependence was investigated by employing *n*-hexene and styrene as examples. Though the stability of the olefin adduct is considerably different between them, the activation barrier does not depend very much on the substrate; it is within 5 kcal/mol. And, v) The electronic structure changes mainly occur in the olefin moiety, the porphyrin ring, and the oxo ligand though the Ru center keeps +II oxidation state during the epoxidation reaction.

Acknowledgements

This work was financially supported by Grand-in-Aids for Specially Promoted Science and Technology (No. 2200009), and Grand Challenge Project from the Ministry of Education, Science, Sports, and Culture. Some of theoretical calculations were performed with SGI workstations of Institute for Molecular Science (Okazaki, Japan), and some of them were carried out with PC cluster computers in our laboratory.

References

(1) (a) Kowan, J. A; *"Inorganic biochemistry"*, Wiley-VCH, New York, **1997**; (b) Lipperd, S. J.; Berg, J. M.; *"Principles of bioinorganic chemistry"*, University Science Books, Mill Vallay, **1994**

(2) (a) Sheldon, R. A.; ed., *"Metalloporphyrins in catalytic oxidations"*, Marcel Dekker, New York, **1994**; (b) Watanabe, Y.; Funabiki, T.; ed.; *"Oxygenases and model systems"*, Kluwer Academic Publishers, Netherlands, **1997**

(3) Nam W.; *Acc. Chem. Res.* **2007**, *40*, 522.

(4) Das, S.; Grudvig. G. W.; Crabtree, R. H.; *Chem. Commun.* **2008**, 413.

(5) Groves J. T.; Myers R. S.; *J. Am. Chem. Soc.* **1983**, *105*, 5791.

(6) Arasasingham, R. D.; He, G.; Bruice T. C.; *J. Am. Chem. Soc.* **1993**, *115*, 7985.

(7) Samsel, E. G.; Srinivasan, K.; Kochi, J. K.; *J. Am. Chem. Soc.* **1985**, *107*, 8273.

(8) Groves, J. T.; Quinn, R.; *J. Am. Chem. Soc.* **1985**, *107*, 5790.

(9) Camenzind, M. J.; James, B. R.; Dolphin, J.; *J. Chem. Soc, Chem. Commun.* **1986**, 1137.

(10) Ostovic, D.; Bruice, T. C.; *Acc. Chem. Res.* **1992**, *25*, 314.

(11) Groves, J. T.; Nemo, T. E.; *J. Am. Chem. Soc.* **1983**, *105*, 6243.

(12) Wonwoo, N.; Goh, Y. M.; Lee, Y. J.; Lim, M. H.; Kim, C.; *Inorg. Chem.* **1999**, *38*, 3238.

(13) Zhao, Y.-C.; Xiang, Y.-Z.; Pu, L.; Yang, M.; Yu. X.-Q.; *Applied Catalysis A* **2006**, *301*, 176.

(14) Collman, J. P.; Brauman, J.I.; Fitzgerald, J. P.; Sparapany, J. W.; Ibers, J. A.; *J. Am. Chem. Soc.* **1988**, *110*, 3486.

(15) Liu, C.-J.; Yu, W.-Y.; Che, C.-M.; Yeung, C.-H.; *J. Org. Chem.* **1999**, *64*, 7365.

(16) Funyu, S.; Isobe, T. Takagi, S.; Tryk, D. A.; Inoue, H.; *J. Am. Chem. Soc.* **2003**, *125*, 5734.

(17) (a) Shaik, S.; Hirao, H.; Kumar, D.; *Acc. Chem. Res.* **2007**, *40*, 532. (b) Sharma, P. K.;

de Visser, S. P.; Ogliaro, F.; Shaik, S.; *J. Am. Chem. Soc.* **2003**, *125*, 2291. (c) de Visser, S. P.; Ogliaro, F.; Harris, N.; Shaik, S.; *J. Am. Chem. Soc.* **2001**, *123*, 3037. (d) Shaik, S.; Kumar, D.; de Visser, S. P.; Altun, A.; Thiel, W.; *Chem. Rev.* **2005**, *105*, 2279. (e) Yoshizawa, K.; Kamachi, T; Yoshihito S. ; *J. Am. Chem. Soc.* **2001**, *123*, 9806

(18) Becke, A. D.; *J. Chem. Phys.* **1993**, 98, 5648.

(19) Becke, A. D.; *Phys. Rev. A* **1988**, *38*, 3098.

(20) Perdew, J. P.; Chevary, J. A.; Vosko, S. H.; Jackson, K. A.; Pederson, M. R.; Singh, D. J.; Fiolhais, C.; *Phys. Rev. B* **1992**, *46*, 6671.

(21) Perdew, J. P.; Burke, K.; Wang,Y.; *Phys. Rev. B* **1996**, *54*, 16533.

(22) Andrae, D.; Haussermann, U.; Dolg, M.; Stoll, H.; Preuss, H.; *Theor. Chem. Acta.* **1990**, *77*, 123.

(23) Ditchfield, R.; Hehre, W. J.; Pople, J. A.; *J. Chem. Phys.* **1971**, *54*, 724.

(24) Dunning, T. H., Jr.; *J. Chem. Phys*. **1989**, *90*, 1007.

(25) (a) Andersson, K; Roos, B. O.; *Chem. Phys. Lett.* **1992**, *191*, 507 (b) Merchán, M.; Pou-Amérigo, R.; Roos, B.O.; *Chem. Phys. Lett.* **1996**, *252*, 405.

(26) (a) Gouterman, M.; *J. Chem. Phys*. **1959**, *30*, 1139. (b) Gouterman, M.; *J. Mol. Spectrosc*, **1961**, *6*, 138.

(27) Pople, J. A.; et al. *Gaussian 03, ReVision C.02*; Gaussian: Inc.:Wallingford, CT, 2004.

(28) Karlstrom, G.; Lindh, R.; Malmqvist, P.-A..; Roos, B. O.; Ryde, U.; Veryazov, V.; Widmark, P.-O.; Cossi, M.; Shimmelpfennig, B.; Neogrady, P.; Seijo, L.; *Computational Material Science*, **2003**, *28*, 222.

(29) Carpenter, J. E; Weinhold, F; *J. Mol. Struct. (THEOCHEM)*, **1988**, *169*, 41

(30) Bytheway, I.; Hall, M. B., *Chem. Rev*. **1994**, *94*, 639

(31) For the optimized geometries of $[Ru(Por)(NH_3)(O)]^-$ and $[Ru(Por)(PH_3)(O)]^-$, see Figure A1 in Appendix.

(32) The composition of active orbitals are summarized in Figure A1.

(33) The $\boldsymbol{\varphi_{SOMO}}$ is the same as the $\boldsymbol{\varphi_{oxo\text{-}\pi}}$ in $\mathbf{A_E}$, however, it is renamed here as $\boldsymbol{\varphi_{SOMO}}$, because this MO completely changes to the π^* of the porphyrin ring when going to $\mathbf{P_E}$ from $\mathbf{A_E}$.

3.5 Appendix

Complete Representation of Ref. 27

Frisch, M. J.; Trucks, G. W.; Schlegel, H. B.; Scuseria, G. E.; Robb, M. A.; Cheeseman, J. R.; Montgomery, J. A., Jr.; Vreven, T.; Kudin, K. N.; Burant, J. C.; Millam, J. M.; Iyengar, S. S.; Tomasi, J.; Barone, V.; Mennucci, B.; Cossi, M.; Scalmani, G.; Rega, N.; Petersson, G. A.; Nakatsuji, H.; Hada, M.; Ehara, M.; Toyota, K.; Fukuda, R.; Hasegawa, J.; Ishida, M.; Nakajima, T.; Honda, Y.; Kitao, O.; Nakai, H.; Klene, M.; Li, X.; Knox, J. E.; Hratchian, H. P.; Cross, J. B.; Bakken, V.; Adamo, C.; Jaramillo, J.; Gomperts, R.; Stratmann, R. E.; Yazyev, O.; Austin, A. J.; Cammi, R.; Pomelli, C.; Ochterski, J. W.; Ayala, P. Y.; Morokuma, K.; Voth, G. A.; Salvador, P.; Dannenberg, J. J.; Zakrzewski, V. G.; Dapprich, S.; Daniels, A. D.; Strain, M. C.; Farkas, O.; Malick, D. K.; Rabuck, A. D.; Raghavachari, K.; Foresman, J. B.; Ortiz, J. V.; Cui, Q.; Baboul, A. G.; Clifford, S.; Cioslowski, J.; Stefanov, B. B.; Liu, G.; Liashenko, A.; Piskorz, P.; Komaromi, I.; Martin, R. L.; Fox, D. J.; Keith, T.; Al-Laham, M. A.; Peng, C. Y.; Nanayakkara, A.; Challacombe, M.; Gill, P. M. W.; Johnson, B.; Chen, W.; Wong, M. W.; Gonzalez, C.; Pople, J. A. *Gaussian 03, Revision D.02*, Gaussian, Inc., Wallingford CT, 2004.

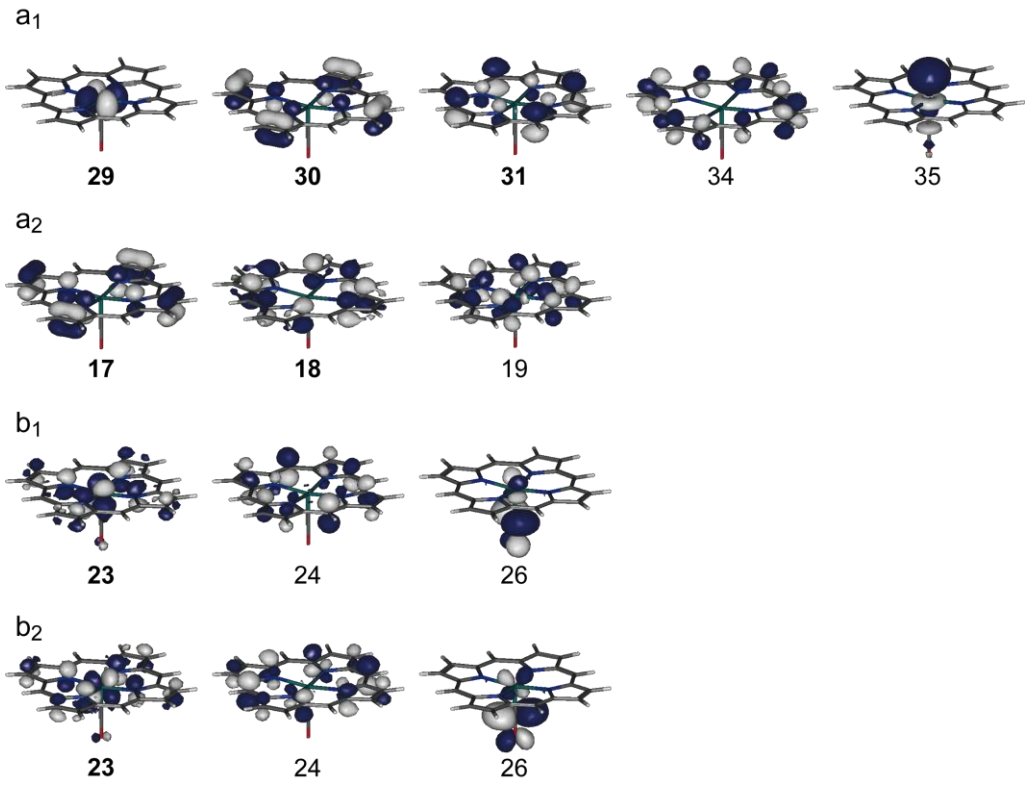

Figure A1. Hartree-Fock orbitals [a)] of [Ru(Por)(CO)] included in the active space for the CASSCF(14 in 14) calculation. a) Orbital numbers with bold face are occupied orbitals.

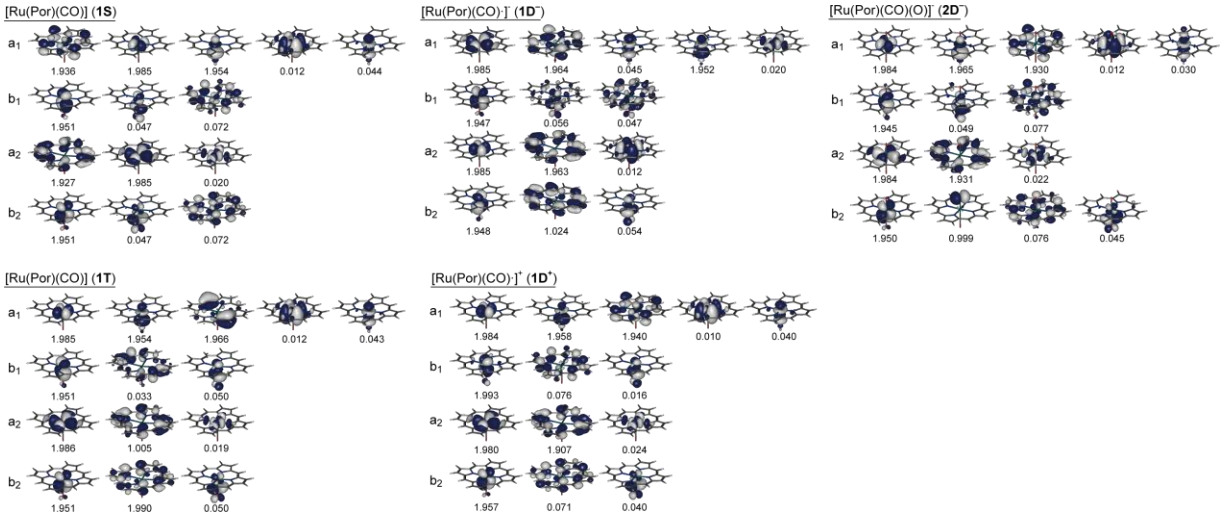

Figure A2. CASSCF-calculated natural orbitals and their occupation numbers of [Ru(Por)(CO)] and $[Ru(Por)(CO)(O)]^{-}$.

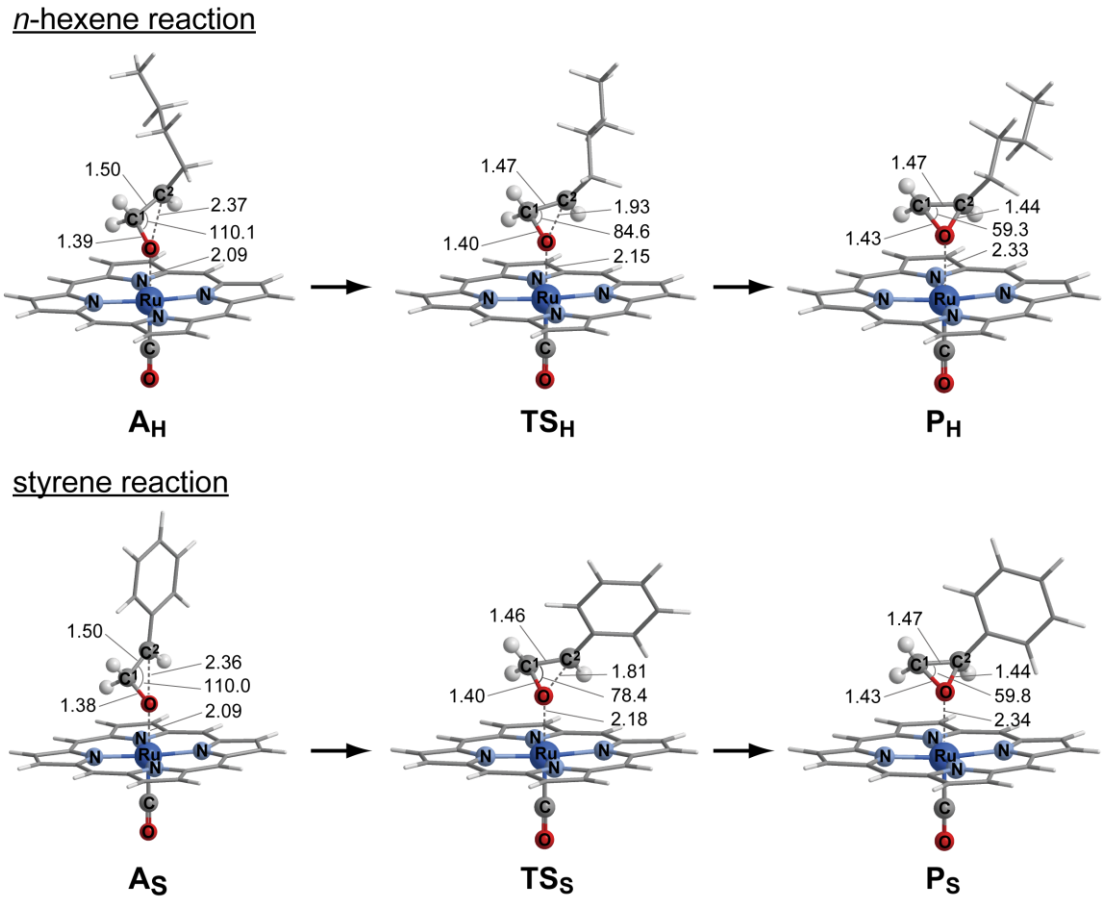

Figure A3. The optimized structure of olefin adducts, transition states, and product complexes for the epoxidation reaction of *n*-hexene and styrene.

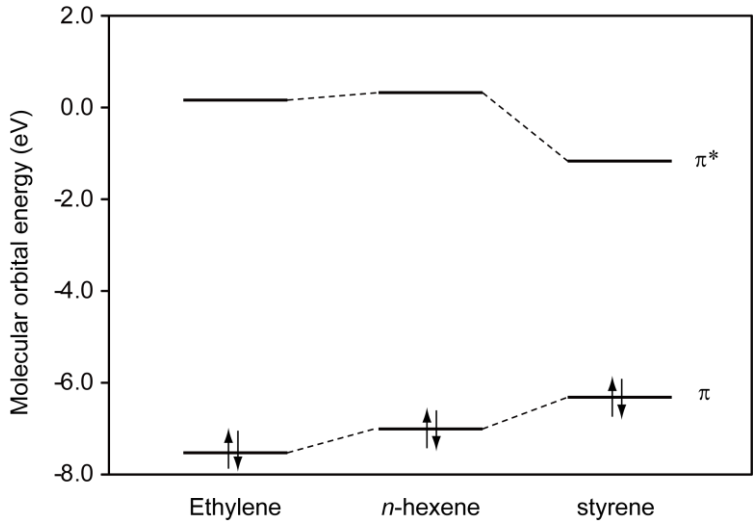

Figure A4. Molecular orbital energies of π and π* orbitals of ethylene, styrene, and *n*-hexene (B3PW91/BS-II).

Part II

Developing Highly Accurate Electronic Structure Theory:

Exact Solutions of the Schrödinger and Dirac Equations

Chapter 4

Solving the Schrödinger and Dirac Equations of Hydrogen Molecular Ion Accurately by the Free Iterative-Complement-Interaction Method

Abstract

The non-relativistic Schrödinger equation and the relativistic four-component Dirac equation of H_2^+ were solved accurately in an analytical expansion form by the free ICI (iterative complement interaction) method combined with the variational principle. In the non-relativistic case, we compared the free ICI wave function with the so-called 'exact' wave function as two different expansions converging to the unique exact wave function and found that the free ICI method is much more efficient than the 'exact' method. In the relativistic case, we first used the inverse Hamiltonian to guarantee Ritz-type variational principle and obtained accurate result. We also showed that the ordinary variational calculation also gives a nice convergence when the g function is appropriately chosen, since then the free ICI calculation guarantees a correct relationship between the large and small components of each adjacent order, which we call ICI balance. This is the first application of the relativistic free ICI method to molecule. We calculated both ground and excited states in good convergence, and not only the upper bound but also the lower bound of the ground-state energy. The error bound analysis has assured that the present result is highly accurate.

4.1 Introduction

Schrödinger equation (SE) is the most fundamental equation in the fields of quantum physics and chemistry, but its solution for general system has long been thought to be impossible.[1] However, recently, we have proposed and developed a general methodology for solving the Schrödinger equation in an analytical expansion form. The methodology is based on the study of the structure of the exact wave function.[2-4] The ICI (iterative complement interaction) method was proposed to construct the exact wave function but it included the integrals of higher-powers of Hamiltonian, which diverge for atoms and molecules for the existence of singular Coulomb potential. This singularity problem has been overcome by introducing the scaled Schrödinger equation (SSE),[3] which is equivalent to the original SE. The ICI method and the free ICI[3] method based on the SSE converge to the exact wave function without encountering the singularity problem. This has enabled us to calculate highly accurate solutions of the SE of various atoms and molecules[2-5]: some were actually the most accurate solutions of the SE so far obtained. Not only the energy, but also the nuclear and electron cusp values and the local energy were shown to be highly accurate[4]. Furthermore, due to its simplicity and generality, the ICI and free ICI methods have been extended to solve the relativistic Dirac equation and the Dirac-Coulomb equation, and accurate solutions of the one- and two-electron atoms have been reported,[6] but applications to molecules have not yet been done. Here, we describe our ICI formalism for solving the hydrogen molecular ion (H_2^+) at both non-relativistic and relativistic levels.

H_2^+ is the simplest molecule and recognized important as an interstellar molecule. Quite accurate descriptions of this molecule have been necessary for the assignment of astronomical spectroscopy.[7] Extensive non-relativistic studies has been done for many years and the exact solutions of H_2^+ and other two-center one-electron systems have been presented[8-10] in analytical expansion form. Relativistic calculations were also made by various methods[11-17] and the major emphasis was the accuracy of the calculated energy: in particular, the

finite-element method (FEM)[11,16] and the direct perturbation theory (DPT)[12] gave accurate results. To date, the FEM result has been regarded to be most accurate in energy. However, in these calculations the variational property was not guaranteed. Further, the FEM does not give an analytical expression of the wave function covering all over the coordinate space. Though there exist the calculations using Gaussian-type orbitals[14] and Slater-type orbitals,[17] their results were not as accurate as those of the FEM and DPT.

In this paper, we present variational solutions of the non-relativistic SE and the relativistic Dirac equation of H_2^+ in analytic expansion forms by applying the free ICI methodology developed in our laboratory. Further, in addition to the upper bound energy, we calculate lower bound energy from the calculated wave function, which guarantees that the present results are highly accurate.

4.2 Theory

4.2.1 Definition of the system

The SE for the non-relativistic H_2^+ is

$$H\psi = E\psi \tag{1}$$

where the Hamiltonian is given in the Born-Oppenheimer (BO) approximation as

$$H = -\frac{1}{2}\nabla_e^{\,2} - \frac{1}{r_a} - \frac{1}{r_b} + \frac{1}{R} \tag{2}$$

a and *b* denote two protons, and *R* the inter-nuclear distance. Owing to the BO approximation, this three-body problem is converted into a two-center one-particle problem, for which one favorably uses elliptic coordinate.

$$\lambda = \frac{r_a + r_b}{R}, \quad \mu = \frac{r_a - r_b}{R}, \quad \omega \tag{3}$$

In this coordinate, the kinetic operator is written as

$$-\frac{1}{2}\nabla_e{}^2 = -\frac{2}{R^2\left(\lambda^2-\mu^2\right)}\left\{\frac{\partial}{\partial\lambda}\left(\lambda^2-1\right)\frac{\partial}{\partial\lambda}+\frac{\partial}{\partial\mu}\left(1-\mu^2\right)\frac{\partial}{\partial\mu}+\frac{\left(\lambda^2-\mu^2\right)}{\left(\lambda^2-1\right)\left(1-\mu^2\right)}\frac{\partial^2}{\partial\omega^2}\right\} \quad (4)$$

and the electron-nucleus Coulomb interaction operator by

$$V = V_{en} = -\frac{2\lambda}{R\left(\lambda^2-\mu^2\right)}. \quad (5)$$

The Dirac equation for the relativistic H_2^+ is written similarly to the SE (Eq. (1)) and its Hamiltonian is defined as

$$H = \begin{bmatrix} (V+c^2)I_2 & c\boldsymbol{\sigma}\cdot\mathbf{p} \\ c\boldsymbol{\sigma}\cdot\mathbf{p} & (V-c^2)I_2 \end{bmatrix} \quad (6)$$

where V represents the electron-nuclei attraction potential given by Eq. (5), $\mathbf{p} = -i\nabla$ is the momentum operator, $\boldsymbol{\sigma}$ the Pauli matrix, and I_2 the 2×2 identity matrix. In all relativistic calculations, we used $c = 1/\alpha = 137.0359895$.[18]

4.2.2 Free ICI method

The SE can be written equivalently in the form of the SSE[3] as

$$g\left(H\psi - E\psi\right) = 0 \quad (7)$$

where the function $g(r) \geq 0$ scales the singularities of the potential to be finite. The choice of *g* in the actual calculations will be described in the next section. The simplest ICI (SICI) based on the SSE,

$$\psi_{n+1} = \left[1 + C_n g(H - E_n)\right]\psi_n \quad (8)$$

is proved to become exact at convergence[3] without encountering the singularity problem for the presence of the scaling function *g*. When one uses variation principle, the energy becomes lower and lower, is bounded from below, and is guaranteed to become exact at convergence, so that it should converge to the exact solution. The free ICI method is defined by gathering all the independent analytical functions from the right-hand side of Eq. (8) as $\{\phi_k\}^{(n)}$, $k = 1...M_n$, and giving independent coefficient to each function as

$$\psi_{n+1} = \sum_{k=1}^{M_n} c_k \phi_k \ . \tag{9}$$

Because of the increased freedom, the free ICI method converges faster to the exact wave function than the original SICI. The variables $\{c_k\}^{(n)}$ of the free ICI wave function are calculated by applying the variational principle to Eq. (9).

Since the ICI formalism is guaranteed to reach the exact solution, this free ICI method gives the best possible wave function at each iteration cycle. Note that in the free ICI method, the next iteration cycle does not require the variables $\{c_k\}^{(n)}$ of the former cycles, so that *n* may be understood as designating the order rather than the iteration cycle. One can get the *n*-th order free ICI functions $\{\phi_k\}^{(n)}$ directly from the initial function ψ_0 by applying the operator part of Eq. (8) *n* times. The accumulation of errors during iterations does not occur in the free ICI calculations. For the determination of the variables $\{c_k\}^{(n)}$, the secular equation should be solved in high accuracy. For this purpose, we used the GMP (GNU multiple precision arithmetic) library[19] and the symbolic operation program, MAPLE.[20]

In the free ICI formalism, we have a freedom in the choices of the *g* function and the initial function ψ_0. The *g* function should be a functional of the inverse of the Coulomb potential, from its purpose to eliminate the singularity of the Coulomb potential. The initial function should have the symmetry of the state we want to calculate: because the Hamiltonian is totally symmetric, the symmetry of the generated functions is always the same as that of the initial function.

The Dirac equation can also be written in a scaled form as

$$g\left(H\psi - E\psi\right) = 0 \tag{10}$$

where the scaling function *g*, which is scalar, is defined similarly to the non-relativistic case. The SICI for the Dirac equation is defined similarly to Eq. (8) as

$$\psi_{n+1} = \left[1 + C_n g(H - E_n)\right]\psi_n \tag{11}$$

and the free ICI by

$$\psi_{n+1} = \sum_{k=1}^{M_n} c_k \phi_k \tag{12}$$

with C_n and c_k here being four-dimensional diagonal matrices and ϕ_k being four-component spinor functions.

Unlike the non-relativistic case, we have to take "variational collapse" problem into account for the Dirac equation. Many studies have been explored to overcome this problem[21] and various methods have been developed. Generally, the variational collapse has its origin in an improper limited representation of the wave function: if the description is enough wide and proper, it should not occur.[22] Actually, however, such description is not an easy task as stated below. Hill and Krauthauser[23] proposed an inverse Hamiltonian method to guarantee the Ritz-type variational property in a rigorous sense. Previously, we applied this method to solve the relativistic Dirac-Coulomb equation of one and two electron atoms.[6]

In the inverse Hamiltonian method, the Dirac equation is rewritten as

$$H^{-1}\psi = E^{-1}\psi \tag{13}$$

Just like in our case of the inverse Schrödinger equation,[24] it is easy to show the equivalence between the original Dirac equation and the inverse one. For the inverse Dirac equation, the lowest positive energy state (corresponding to the electronic ground state) is mapped to the top of the spectrum i.e. the highest solution against the complete vacuum, and therefore the following Ritz-like variational principle holds for the inverse Hamiltonian operator

$$E^{-1} = \frac{\left\langle \psi \middle| H^{-1} \middle| \psi \right\rangle}{\left\langle \psi \middle| \psi \right\rangle} \leq E_0{}^{-1} \tag{14}$$

where ψ is a variational trial function for ψ and E_0 is the true energy of the ground electronic state. Here a difficult problem arise, that is, how we write H^{-1} explicitly in a closed form. A clever trick was introduced by Hill and Krauthauser and enabled us to avoid the explicit use of the inverse Hamiltonian. Namely, we choose our variational function ψ in the form of

$$\psi = H\varphi \tag{15}$$

In which φ represents a free variation. Then, the variational equation above is written as

$$E^{-1} = \frac{\langle\varphi|H|\varphi\rangle}{\langle\varphi|H^2|\varphi\rangle} \le E_0^{-1} \tag{16}$$

and all the quantities can be calculated without an explicit use of the inverse Hamiltonian. At the diagonalization step of the relativistic free ICI, we utilize the above Ritz-like variational equation to ensure the bound property. However, the choice of the trial function ψ in the form of Eq. (15) imposes some restriction on φ, since ψ must be square integrable. The existence of the singular potential in H makes the basis function form of φ to be more limited.

In addition, we calculated the following expectation value

$$\langle E\rangle = \frac{\langle\varphi|H|\varphi\rangle}{\langle\varphi|\varphi\rangle} \tag{17}$$

using the eigenvector φ calculated by the above inverse method. We call this energy as Inverse-Regular (I-R) energy. Since φ of Eq.(17) was calculated with the use of the inverse Hamiltonian method that avoids the variational collapse, the energy expectation value of this φ would be reliable. To distinguish from this I-R energy, we call the energy calculated by the inverse method given by Eq.(16) as Inverse-Inverse (I-I) energy. Throughout the paper, we call these inverse Hamiltonian-based methods as “the inverse method”.

On the other hand, we may also use the ordinary variational method based on the standard regular Hamiltonian. We call such method “regular method”. The energy calculated from the wave function of the regular method has the form of Eq.(17), so that this energy may be called Regular-Regular (R-R) energy. The I-R and R-R energies are not bounded from above but have the following interesting features characterized by the ICI method.

It is well known that the Dirac equation connects the large and small components:[22] the exact connection is called “atomic” balance and an approximate one “kinetic” balance. So,

when one imposes such balancing condition between the basis sets of the large and small components, one can avoid the variational collapse. Actually, in our free ICI formalism, the correct relationship between the large and small components is imposed between those of the adjacent orders:[6] within each order, the relationship is approximate, so that this balancing does not help much initially at low orders, but as the order increases, it approaches the correct balancing. We call this balancing as "ICI" balance. Thus, within the ICI methodology, even the ordinary variational method based on the regular Hamiltonian may give correct variational solutions as far as the order *n* is large enough. On the other hand, the I-I method is always guaranteed to have the bound property as expressed by Eq. (16).

4.2.3 Calculation of the lower bound

All types of the energies given in the previous section correspond to the upper bounds to the exact energy. If we can calculate accurate lower bound of the exact energy from the wave function we are at hands, we can estimate correctly the error bars of the calculated energy. From this point of view, the calculation of the lower bound is as important as that of the upper bound and so, many researches for the lower bound have been made (see for example, Ref.25). Most of them are related to the variance of the energy given by,

$$\sigma^2 = \frac{\langle\psi|H^2|\psi\rangle}{\langle\psi|\psi\rangle} - \left[\frac{\langle\psi|H|\psi\rangle}{\langle\psi|\psi\rangle}\right]^2 . \tag{18}$$

In spite of its importance, the calculation of the lower bound is not as popular as that of the upper bound, because the calculation of the integral $\langle\psi|H^2|\psi\rangle$ is generally more difficult than that of $\langle\psi|H|\psi\rangle$. Additionally, it is known[25] that one cannot obtain a lower bound as accurately as an upper bound unless we have a quite accurate wave function. Our free ICI wave function gives quite accurate upper bound to the exact energy, so that we can expect that it may also give accurate lower bound to the exact energy. When we use the inverse method, the integral $\langle\psi|H^2|\psi\rangle$ is necessary also for the upper-bound calculation. This means that we

can calculate the upper and lower bounds at the same time.

Among the various formulas of the lower bound, we utilized the Temple's lower bound[27] given by

$$E_{low} = \langle \psi | H | \psi \rangle - \frac{\sigma^2}{E_{ex} - \langle \psi | H | \psi \rangle} \tag{19}$$

where E_{ex} is the energy of the first excited state having the same symmetry as the ground state. The calculation of E_{ex} is also easy in the free ICI method, because the excited states are obtained as the higher-energy solutions of the diagonalization for the ground state. Since the lower bound nature is ensured for the inverse method, the same nature is also ensured to the calculated energy of the excited state. So, the inequality $E < E_{ex}$ is assured. Thus, we can safely apply Temple's method even to the relativistic case.[28]

4.3 Results and Discussions

4.3.1 Non-relativistic case

Here, we performed the free ICI calculations for solving the SE of H_2^+. The g function was chosen as the inverse of the electron-nuclear Coulomb potential written in the elliptic coordinate as

$$g = -\frac{1}{V} = \frac{R\left(\lambda^2 - \mu^2\right)}{4\lambda} \tag{20}$$

For the $1\sigma_g$ ground state, the initial function was the Slater-type function

$$\psi_0 = \exp\left[-\frac{\alpha'}{R}\left(r_a + r_b\right)\right] = \exp\left(-\alpha\lambda\right) \tag{21}$$

where α and α' are nonlinear parameters with $\alpha' = R\alpha$. In this choice, the free ICI wave function is generated in the analytical expansion form of

$$\Psi = \sum_i c_i \lambda^{m_i} \mu^{n_i} \exp\left(-\alpha\lambda\right), \tag{22}$$

TABLE II. Non-relativistic energy for the ungerade excited state ($1\sigma_u$) of H_2^+ (R=2.0 a.u.).

Order	Dimension	α	Energy (a.u.)
0	1	0.9	**-0.66**2993039443155452436195
1	4	0.8	**-0.667**236686962501148195507
2	13	1.1	**-0.66753**4068275070663143593
3	26	1.0	**-0.667534392**107704479296447
4	43	1.0	**-0.667534392202**280580231750
5	64	1.1	**-0.667534392202382**893318000
6	89	1.1	**-0.667534392202382930**343919
7	118	1.1	**-0.667534392202382930361968**
Our best result (Order=14,Dim.=433)		1.2	-0.667534392202382930361970211 49
Exact wave function [31]			-0.6675343922024
Correlated wave function [32]			-0.6675078
Finite element method [34]			-0.6675331
Finite difference method [35]			-0.667534392205

where c_i is the variational parameter and m_i is positive or negative integer. Since the $1\sigma_g$ ground state has a gerade symmetry, n_i should be zero or positive even integer. A simple function given by James[29]

$$\psi = \exp(-\alpha\lambda)\left(\mu^2 + \gamma\right) \tag{23}$$

where γ is a variable coefficient, is regarded as a special example of our form of the exact wave function. We summarize in Table I the calculated energies for the ground state $1\sigma_g$ at different orders. Alpha values were optimized at each order. The convergence of the free ICI energy was quite good. Our best energy is the known best of the exact energy.

The first excited state $1\sigma_u$ (ungerade) was also calculated, starting from the initial function of the ungerade symmetry

$$\psi_0 = \mu \exp(-\alpha\lambda). \tag{24}$$

The free ICI wave function of the $1\sigma_u$ state is also expressed in the analytical expansion form given by Eq. (22) where n_i should be positive odd integers. The *g* function was the same as for the $1\sigma_g$ state given by Eq. (21). The results are given in Table II. Just as for the gerade states, the convergence of the free ICI was very good and quite accurate energy was

TABLE III. The deviations of ICI wave functions from the exact wave function. (R=2.0 a.u., α 's are same as in Table 1).

Order	Dimension	σ^2
0	1	1.2635×10^{-2}
1	4	1.0723×10^{-3}
2	13	2.4902×10^{-6}
3	26	7.0255×10^{-10}
4	43	4.8703×10^{-13}

calculated.

For H_2^+, the exact wave function for the non-relativistic SE is known and given by[8]

$$\psi(\lambda,\mu,\phi)=\Lambda(\lambda)\mathrm{M}(\mu)\exp(im\phi) \tag{25}$$

where

$$\begin{aligned}\Lambda(\lambda)&=(1+\lambda)^{\sigma}(\lambda^2-1)^{\frac{|m|}{2}}\exp(-\alpha\lambda)\sum_{k=0}^{\infty}g_k\left(\frac{1-\lambda}{1+\lambda}\right)^k\\ \sigma&=\frac{R}{\alpha}-|m|-1\\ \mathrm{M}(\mu)&=\sum_{l=0}^{\infty}f_lP_l(\mu)\end{aligned} \tag{26}$$

m corresponds to the magnetic quantum number and $P_l(\mu)$ is associated Legendre function. g_k and f_l are the coefficients determined by the differential equations obtained from the SE by separating the variables. Note that the exact wave function is given also in the analytical expansion form as our free ICI wave function given by Eq. (22). They are two different expressions of the analytic expansion of the one unique exact wave function.

We now want to compare the present free ICI wave function with the exact wave function. However, the exact wave function is defined in the infinite expansion form and, practically, we have to truncate this expansion, which was first introduced by Wind[9] and more elaborate and general cases were studied by Hunter and co-workers.[10] We followed the method of Ref.10 and determined the coefficients g_k and f_l of Eq. (26). Then, we compare this 'truncated exact' wave function with the free ICI wave function. For this purpose, we

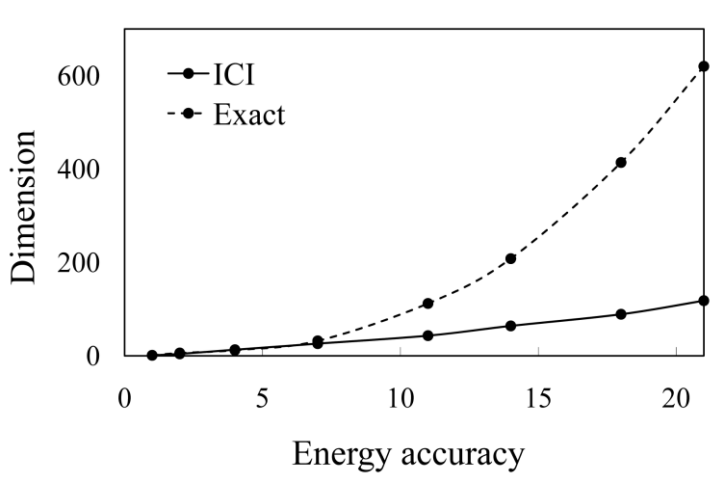

FIG. 1. The efficiency comparison between the free ICI wave function and the 'exact' wave function. The digits in x-axis is defined as the energy eigen value that has 10^{-N} (a.u.) accuracy.

introduce

$$\sigma^2 = \int \left(\psi_{t.exact} - \psi_{fICI} \right)^2 d\tau \tag{27}$$

which shows the deviation of the ICI wave function from the 'truncated exact' one. This quantity is zero, when ψ_{fICI} and $\psi_{t.exact}$ are identical everywhere in the coordinate space.

Here, the exact series of Eq. (26) were truncated at the orders of λ and μ to be less than 23 and 14, respectively, which assures E = -1.10 263 421 449 49 (a.u.). The criteria for the energy accuracy and the truncation level are essentially the same as those in Ref.10. We show in Table III the convergence behavior of σ^2. We see that as the order increases, the ICI wave function converges very rapidly to the 'truncated exact' wave function. This is reasonable, since the free ICI wave function is also guaranteed to converge to the exact wave function as the order n increases, likewise the exact series given by Eq. (26). In other words, now, we have two different series of analytical wave functions that converge to the exact wave function. So, a question is which is more efficient? We examine it below.

First, how many basis functions are necessary for obtaining the similar accuracy? Figure 1 shows a comparison between the 'truncated exact' method and the free ICI method to get the similar energy accuracy. The abscissa corresponds to the energy accuracy in the number of correct figures. Apparently, the convergence of the free ICI wave functions is quite

efficient. To calculate the 'truncated exact' wave function, one must iteratively solve the eigenvalue equations and estimate the λ and μ truncation error. They are not an easy task as the dimension grows.[10] Different from the method of Ref.10, the calculations based on the variational principle is also possible for the 'truncated exact' form. This gives, for example, -1.10 263 421 449 494 646 150 897 (a.u.) by 110 functions (the order of λ and μ is less than 10 and 18 respectively), to be compared with -1.10 263 421 449 494 646 150 880 a.u. (with 118 functions) of the free ICI results. Both energies are much more accurate than the 'non-variational truncated exact' energy -1.10 263 421 449 49 au for the 322 functions. Note that the variational energy of the 'truncated exact' form is lower than that of the free ICI wave function. However, the variational treatment of the 'truncated exact' wave functions is quite difficult because the functions involved in the series are almost linearly dependent to each other and so, the Hamiltonian and overlap matrices must be calculated in very high accuracy. Moreover, the integrations are also difficult because of the existence of the nonlinear terms in Eq. (26). Therefore, it is not practical to perform variational calculations with the 'exact' wave function series.

In conclusion, we could say that the free ICI procedure is much more efficient way of solving the non-relativistic exact wave function of H_2^+ than even the exact treatment of the SE of H_2^+.

4.3.2 Relativistic case

Next, we solved the relativistic Dirac equation of H_2^+ by the free ICI method. The initial function we used for the $1\sigma_g$ state was given by[30]

$$\Psi_0 = \begin{bmatrix} \exp(-\alpha\lambda)\exp\left[i\left(j_z - 1/2\right)\phi\right] \\ \left(\lambda^2-1\right)^{1/2}\left(1-\mu^2\right)^{1/2}\exp(-\alpha\lambda)\exp\left[i\left(j_z + 1/2\right)\phi\right] \\ i\exp(-\alpha\lambda)\exp\left[i\left(j_z - 1/2\right)\phi\right] \\ i\left(\lambda^2-1\right)^{1/2}\left(1-\mu^2\right)^{1/2}\exp(-\alpha\lambda)\exp\left[i\left(j_z + 1/2\right)\phi\right] \end{bmatrix} \tag{28}$$

TABLE IV. Relativistic energy for the ground state ($1\sigma_g$) of H_2^+ with the *g* function given by Eq. (21) (R=2.0 a.u., $\alpha = 2.0$: The numbers of the spinor components are shown in the parenthesis).

Order	Dimension	I-I Energy (a.u.)
0	4 (1,1,1,1)	-0.6594969133727
1	11 (1,3,6,1)	**-1.**0834484339038
2	47 (12,10,16,9)	**-1.10**13653644609
3	95 (25,22,29,19)	**-1.102**4339663805
4	159 (41,37,47,34)	**-1.102**5870474807
5	239 (62,57,68,52)	**-1.1026**221128247
6	335 (86,80,94,75)	**-1.1026**328935674
7	447 (115,108,123,101)	**-1.1026**369886193
8	575 (147,139,157,132)	**-1.1026**388097689
9	719 (184,175,194,166)	**-1.1026**397349807
10	879 (224,214,236,205)	**-1.10264**02566241
11	1055 (269,258,281,247)	**-1.10264**05774799
12	1247 (317,305,331,294)	**-1.10264**07890222
13	1455 (370,357,384,344)	**-1.10264**09366510
14	1679 (426,412,442,399)	**-1.102641**0443317
15	1919 (487,472,503,457)	**-1.102641**1254552
Finite element method [11]		-1.1026415810338
Direct perturbation theory [12]		-1.102641579453
Finite Difference method [35]		-1.1026415709
Monte Carlo method [13]		-1.102565
Four component Gaussian type spinor [14]		-1.1026415801
Minimax theory [15]		-1.102481

where j_z describes the projection of the total angular momentum on the inter-nuclear axis and equals to 1/2 for σ symmetry. We examined two sets of g functions and the first one is the same as that given by Eq. (20). Utilizing this set of initial and *g* functions, the free ICI procedure generates the analytical wave function given by

TABLE V. Relativistic energy for the ground state ($1\sigma_g$) of H_2^+ with the *g* function given by Eq. (31) (R=2.0 a.u., $\alpha = 2.0$: The numbers of the spinor components are shown in parenthesis and the energy overshooting are noted by bold italic).

Order	Dimension	Energy (a.u.)		
		I-I	I-R	R-R
0	4 (1,1,1,1)	-0.65949691337272	**-1.*275***91016235589	**-1.*275***91016222465
1	20 (8,4,4,4)	**-1.**09946179447425	**-1.10*361***557960033	**-1.10*492***476160926
2	93 (26,19,25,23)	**-1.10264**084007285	**-1.10264**102311906	**-1.10264*255***845192
3	196 (56,45,49,46)	**-1.102641**57774844	**-1.102641**57840721	**-1.10264158*596***662
4	336 (90,76,88,82)	**-1.10264158**098489	**-1.1026415810**1802	**-1.10264158103*477***
5	512 (141,122,126,123)	**-1.1026415810**0940	**-1.10264158103**210	**-1.10264158103*370***
6	724 (191,167,186,180)	**-1.1026415810**1594	**-1.10264158103**256	**-1.10264158103**49
7	975 (262,234,242,237)	**-1.1026415810**2005	**-1.10264158103**11	**-1.10264158103**58
8	1262 (330,297,321,314)	**-1.1026415810**2283	**-1.10264158103**11	**-1.10264158103**56
9	1585 (418,383,395,389)	**-1.1026415810**2492	**-1.10264158103**36	**-1.1026415810335**952
10	1944 (506,464,491,483)	**-1.1026415810**2637	**-1.10264158103**38	**-1.1026415810335**912
11	2341 (611,567,585,578)	**-1.1026415810**2753	**-1.10264158103**44	**-1.1026415810335**980
12	2774 (719,668,698,689)	**-1.1026415810**2843	**-1.10264158103**50	**-1.1026415810335**981
	Finite element method [11]		-1.1026415810338	
	Direct perturbation theory [12]		-1.102641579453	
	Finite Difference method [36]		-1.1026415709	
	Monte Carlo method [13]		-1.102565	
	Minimax theory [15]		-1.102481	
	Four component Gaussian type spinor [14]		-1.1026415801	

$$\Psi = \sum_i \left\{ \begin{bmatrix} c_i^1 \\ 0 \\ 0 \\ 0 \end{bmatrix} \lambda^{m_i} \mu^{n_i} \exp(-\alpha\lambda) + \begin{bmatrix} 0 \\ c_i^2 \\ 0 \\ 0 \end{bmatrix} (\lambda^2 - 1)^{1/2} (1-\mu^2)^{1/2} \lambda^{m_i} \mu^{n_i} \exp(-\alpha\lambda) \exp(i\varphi) \right\} \quad (29)$$
$$+ \left\{ \begin{bmatrix} 0 \\ 0 \\ c_i^3 \\ 0 \end{bmatrix} i\lambda^{m_i} \mu^{n_i} \exp(-\alpha\lambda) + \begin{bmatrix} 0 \\ 0 \\ 0 \\ c_i^4 \end{bmatrix} i(\lambda^2 - 1)^{1/2} (1-\mu^2)^{1/2} \lambda^{m_i} \mu^{n_i} \exp(-\alpha\lambda) \exp(i\varphi) \right\}$$

Obviously, the first element of the large component has the same form as the non-relativistic wave function and this means that the wave functions generated by the *g* function of Eq. (20) have the same structure as the non-relativistic case. Table IV shows the results of I-I energy

calculations. The I-I energy converges from above as the order increases and we did not encounter any variational collapse difficulty. However, the speed of the convergence was very slow.

So, we next chose the *g* function given by

$$g = 1 - \frac{1}{V} = 1 + \frac{R\left(\lambda^2 - \mu^2\right)}{4\lambda} \tag{30}$$

where we added the factor unity on the right hand side of Eq. (20). With the use of the same initial wave function as above, the free ICI method generated the analytical wave function written as

$$\Psi = \sum_i \begin{bmatrix} c_i^1 \cdot \lambda^{m_i} \mu^{n_i} \exp\left(-\alpha\lambda\right) / \left(\lambda^2 - \mu^2\right)^{l_i} \\ c_i^2 \cdot \left(\lambda^2 - 1\right)^{1/2} \left(1 - \mu^2\right)^{1/2} \lambda^{m_i} \mu^{n_i} \exp\left(-\alpha\lambda\right) \exp\left(i\varphi\right) / \left(\lambda^2 - \mu^2\right)^{l_i} \\ c_i^3 \cdot i\lambda^{m_i} \mu^{n_i} \exp\left(-\alpha\lambda\right) / \left(\lambda^2 - \mu^2\right)^{l_i} \\ c_i^4 \cdot i\left(\lambda^2 - 1\right)^{1/2} \left(1 - \mu^2\right)^{1/2} \lambda^{m_i} \mu^{n_i} \exp\left(-\alpha\lambda\right) / \exp\left(i\varphi\right) \left(\lambda^2 - \mu^2\right)^{l_i} \end{bmatrix}. \tag{31}$$

The above function includes the function given by Eq. (29) when $l_i = 0$, and so it is more general than that of Eq. (29). Note that the *g* function of Eq. (30) produces also the functions that are not square integrable, so that they have to be eliminated because the wave function must be square integrable. Table V shows the results of the I-I, I-R and R-R energies when we use the *g* function of Eq. (30). It is remarkable that the energy convergence in Table V is considerably faster than that in Table IV, which shows the importance of the g function given by Eq.(30). The wave function of the form of Eq.(31) was firstly obtained by the present free ICI method. Actually, this type of functions has not been used in the previous studies of H_2^+.

Here, a remark on the numbers of the complement functions between the inverse and regular methods given in Table V. Generally speaking, the inverse and regular methods have different dimensions because the inverse method involves $\left\langle \phi_i \middle| H^2 \middle| \phi_j \right\rangle$ integration. The functional form of ϕ_i in the inverse method is more limited, because there are some

functions ϕ_i that $\langle \phi_i | H | \phi_j \rangle$ is finite but $\langle \phi_i | H^2 | \phi_j \rangle$ is infinite. However, in the present case, the denominator of Eq. (31) includes only integer indices and therefore the dimensions of the inverse and regular methods are the same.

A reason of the accelerated convergence brought about by this new type of functions lies in the balance condition between the large and small components, which is a necessary condition for the exact solution of the Dirac equation. The *g* function of Eq. (30) is desirable for satisfying this balancing condition between the large and small components. From the large ψ_n^l and small ψ_n^s components of ψ_n, the ICI generates the functions $cg(\boldsymbol{\sigma}\cdot\mathbf{p})\psi_n^l$ into the small component of ψ_{n+1} and the functions $cg(\boldsymbol{\sigma}\cdot\mathbf{p})\psi_n^s$ into the large component of ψ_{n+1}. The factor unity in Eq. (30) assures that ψ_{n+1} contains $c(\boldsymbol{\sigma}\cdot\mathbf{p})\psi_n^l$ in its small component and $c(\boldsymbol{\sigma}\cdot\mathbf{p})\psi_n^s$ in the large component. They are the kinetic-balancing functions which are of zero-th order of the true balancing. However, with the *g* function of Eq. (20) that does not contain unity, the ICI cannot generate the zero-th order kinetic-balancing functions in the next order. This is the main reason of the very slow convergence in Table IV. Thus, it is quite significant for the relativistic calculations to contain the factor unity into the *g* function. The *g* function of Eq. (30) includes not only unity but also the first order function (1/V) and, therefore, the higher-order exact balancing functions are automatically generated into the wave function of the next order. This is the ICI balance and is very close to the true balancing (atomic balance) [37]: a difference is only that it is between neighboring order, not within the same order, which is really necessary. This is one of the most beneficial points of the present free ICI method for solving the relativistic DE.

In Table V, all the energies (I-I, I-R, and R-R) show good convergence. The I-I method is safer than the others since the upper-bound nature of the energy is guaranteed. The I-I energy, however, seems to be less rapidly convergent than the I-R and R-R energies. The I-R and R-R energies at *n*=12 and *M*=2774 are **-1.10 264 158 103 3**50 (a.u.) and **-1.10 264 158 103 3**59 81 (a.u.), respectively. In comparison with the best energy **-1.10 264 158 103 3**8

(a.u.) in the literature obtained with the finite element method, these energies show very good agreement with each other except for the final digit of 10^{-13} (note we used the same c=137.0359895 for all). The converged value of the R-R energy showed the same value to the digit of 10^{-14}, **-1.10 264 158 103 3**59 (a.u.) from *n*=9 to *n*=12, which indicates that the correct energy of the relativistic H_2^+ with c=137.0359895 is **-1.10 264 158 103 3**60 (a.u.) and the energy from the finite element method might be slightly overshooting at the 10^{-13} digit.

We must note that the I-R and R-R energies overshoot the true energy (as shown by bold italic) at the earlier stage of free ICI, because the balancing between the neighboring order is particularly insufficient in the earlier stages. The overshooting is seen for the I-R energies of n = 0 and 1 and for the R-R energies of n = 0 to 5. As the order n increases, almost variational results are achieved. The I-R energy is slightly more stable and safer than the R-R energy because the wave function was determined in the constrained variational space by the inverse method. In the R-R case, its energy steadily converges to the exact one as the order increases, since the exact balancing is almost attained by the ICI balance at higher orders.

Further, we must note in the table that the convergence becomes slow in the higher-order steps of the calculations. We think that the reason lies in the limited description of the mild singularity with the present g and initial functions. The exact solution of the DE should have a mild (non-integer close to zero) singularity at the position of the nucleus. Our wave function of Eq. (31) has the denominator $\left(\lambda^2-\mu^2\right)^{l_i}$ ($l_i \geq 0$: integer), which causes a singular behavior of the wave function at the position of the nucleus. However, since l_i is integer, it may be difficult to describe effectively the non-integer mild singularity. Previously, we introduced 'mild singular' g function like $g = r^{99/100}$ in the calculations of the relativistic hydrogen atom, obtaining good convergence.[6] However, a straightforward application of this idea to the present H_2^+ molecule would cause difficult integrations. So, we postpone such calculations in the future.

TABLE VI. Relativistic energy for the ungerade excited state ($1\sigma_u$) of H_2^+ with the *g* function given by Eq. (31) (R=2.0 a.u., $\alpha = 2.0$: The numbers of the spinor components are shown in parenthesis and the energy overshooting are noted by bold italic).

Order	Dimension	I-I Energy (a.u.)	I-R Energy (a.u.)
0	4 (1,1,1,1)	0.9851699389728	***-1.47***26941318426
1	30 (10,7,7,6)	**-0.6**574541639251	**-0.66**52990615903
2	112 (29,26,33,24)	**-0.667**3614750319	**-0.667**3806927312
3	222 (58,55,60,49)	**-0.6675**462755479	**-0.6675**466299705
4	369 (92,89,102,86)	**-0.667552**5401111	**-0.667552**5594780
5	555 (145,138,146,126)	**-0.6675527**655176	**-0.6675527**662534
6	778 (193,189,211,185)	**-0.66755277**17710	**-0.66755277**18000
7	1038 (268,261,269,240)	**-0.667552771**9766	**-0.667552771**9889
8	1336 (332,326,357,321)	**-0.667552771**9857	**-0.667552771995**0
9	1672 (428,421,431,392)	**-0.667552771**9876	**-0.667552771995**5
Finite element method [11]		-0.667552771996	
Direct perturbation theory [12]		-0.667552771493	
Finite Difference method [36]		-0.6675527640	
Minimax theory [15]		-0.669175	

We applied further the present method to the excited state of σ_u symmetry. We used the *g* function given by Eq. (30) and, in order to represent the ungerade symmetry, the initial function is

$$\Psi_0 = \begin{bmatrix} \mu \exp(-\alpha\lambda) \\ (\lambda^2-1)^{1/2}(1-\mu^2)^{1/2}\mu \exp(-\alpha\lambda) \\ i\mu \exp(-\alpha\lambda) \\ i(\lambda^2-1)^{1/2}(1-\mu^2)^{1/2}\mu \exp(-\alpha\lambda) \end{bmatrix}. \tag{32}$$

As in the non-relativistic calculations, just switching the symmetry of the initial function is sufficient to satisfy the symmetry of the wave function. The convergence behaviors of the I-I and I-R energies are shown in Table VI. As in the gerade symmetry case, quite accurate relativistic energy of the $1\sigma_u$ state was calculated. Again, the I-I energy converges more slowly than the I-R energy, though a overshooting of the energy was seen in the I-R energy of the initial function. The excited state having the same symmetry as the ground state was calculated at the same time and the result will be shown below.

As stated above, the calculations of the energy lower bounds, in addition to the upper bounds, are important. For using the Temple's method, we also have to calculate the energy upper bound for the first excited state with the σ_g symmetry. For this purpose, it is necessary to include in ψ_0 the functions appropriate to the ground and first excited states. Then, the $2\sigma_g$ state is calculated at the same time as the ground $1\sigma_g$ state as the second lowest state. For this reason, we introduced the double-exponent initial function given by

$$\Psi_0 = \begin{bmatrix} \exp(-\alpha_1\lambda) + \exp(-\alpha_2\lambda) \\ (\lambda^2-1)^{1/2}(1-\mu^2)^{1/2}\{\exp(-\alpha_1\lambda) + \exp(-\alpha_2\lambda)\} \\ i\{\exp(-\alpha_1\lambda) + \exp(-\alpha_2\lambda)\} \\ i(\lambda^2-1)^{1/2}(1-\mu^2)^{1/2}\{\exp(-\alpha_1\lambda) + \exp(-\alpha_2\lambda)\} \end{bmatrix} \tag{33}$$

where α_1 and α_2 corresponds to the exponents of the ground and excited states, respectively. We here simply assumed α_2 to be one half of α_1 from the analogy to the hydrogen atom where an orbital exponent is proportional to the reciprocal of its principal quantum number.

Table VII shows the result of the lower bound calculation at each order. Clearly, the lower bound converged to the exact energy from below as contrasted with the usual variational energy (upper bound) converging from above. As the order increases, the width between the lower and upper bounds becomes narrower and narrower. Considering the fact that the lower bound corresponds to the variance of the energy, the present results indicate that a quite accurate wave function is obtained by the free ICI procedure. From the result of Table VII, we can show the absolute error of the calculated energy by the difference between the upper and lower bounds. For the order 8 result in Table VII, this is 1.97×10^{-7} a.u. which is in cm^{-1} unit 4.3×10^{-2} cm^{-1}: this may be compared to the uncertainty of the recent experimental result, 2×10^{-2} cm^{-1}.[38] Actually, from the theoretical reason, the true value should be much closer to the calculated upper bound energy.

The energy of the $2\sigma_g$ state, an excited state belonging to the same symmetry as the

ground state, is shown in Table VIII. It corresponds to E_{ex} of Eq. (19). It was calculated as the second lowest energy of the same eigenvalue problem, together with the energy of the $1\sigma_g$ state. The present result seems to be better than the DPT result and would be the best one so far obtained.

4.4 Conclusions

We have already shown in the previous papers[3-6] that the free ICI method provides a general method of solving not only the non-relativistic SE but also the relativistic Dirac and Dirac-Coulomb equations in analytical expansion forms. In this paper, we have shown that the free ICI method combined with the variational principle gives very accurate analytic wave functions of H_2^+ efficiently in both non-relativistic and relativistic cases. For the non-relativistic case, we compared two analytical expansions conversing to the exact wave function: the so-called 'exact' wave function and the present free ICI wave function. It was shown that the free ICI method was even more efficient than solving the 'exact' wave function of H_2^+.

For the relativistic case, this study represents the first application of the free ICI method to molecule. An appropriate choice of the g function was shown important for describing the correct ICI balance between the large and small components of the neighboring ICI wave functions. By using the inverse Hamiltonian method, we could avoid the variational collapse problem and the calculated I-I energy was an upper bound of the ground-state energy. For the ICI balance, even the variational calculations with the regular Hamiltonian were stable giving rapidly converging result. We compared the converging behaviors of the I-I, I-R, and R-R energies. The I-I energy was rather slow in convergence, though it always satisfied upper-bound nature. The present relativistic free ICI calculations showed reasonably fast convergences for both the ground and excited states.

We have further calculated the lower bounds of the relativistic energy. The knowledge

of both the upper and lower bounds of the relativistic energy showed that the present relativistic wave function and energy are very accurate with the energy error being less than 4.3×10^{-2} cm^{-1}. Actually, the true value should be much closer to the calculated upper bound energy. Generally speaking, the lower bound calculations will become more and more important in future for both the non-relativistic and relativistic calculations, since we cannot assure the accuracy of the calculated results if the system includes more than five electrons, since there are no highly accurate calculations for the solutions of the SE equation for such systems. For the relativistic case, the calculations of both upper- and lower-bounds give us further a clear criterion on the occurrence of the variational collapse problem.

Thus, we have shown that the free ICI methodology can give quite accurate solutions for both the Schrödinger equation and the Dirac equation of H_2^+ molecule. In principle, this method can be applicable to any systems if the Hamiltonian is well defied in an analytical form. When analytical integrations over the free ICI complement functions are possible, the wave functions and energies are calculated by the variational method, and if such integrations are impossible, they are calculated by the local Schrödinger equation (LSE) method developed in our laboratory[39], both in high accuracy.

Acknowledgements

This research was supported by the Grant for Creative Scientific Research from the Ministry of Education, Science, Culture, and Sports of Japan.

References

(1) Dirac, P. A. M.; *Proc. R. Soc., A.*, **1929**, 123, 714.

(2) (a) Nakatsuji, H.; *J. Chem. Phys.* **2000**, 113**,** 2949. (b) Nakatsuji, H.; Davidson, E. R.; *ibid.* **2001**, 115, 2000. (c) Nakatsuji, H.; *ibid.* **2001**, 115, 2465; (d) **2002**, 116, 1811. (e) Nakatsuji, H.; Ehara, M.; *ibid.* **2002**, 117, 9. (f) **2005**, 122, 194108. (g) Nakatsuji, H.; *Bull. Chem. Soc. Jpn.* **2005**, 78, 1705.

(3) (a) Nakatsuji, H.; *Phys. Rev. Lett.* **2004**, 93, 030403. (b) *Phys. Rev. A* **2005,** 72 062110.

(4) Kurokawa, Y.; Nakashima, H.; Nakatsuji, H.; *Phys. Rev. A* **2005**, 72**,** 062502.

(5) Nakashima, H.; Nakatsuji, H.; *J. Chem. Phys.* **2007**, 127, 224104-1-14.

(6) Nakatsuji, H.; Nakashima, H.; *Phys. Rev. Lett.* **2005**, 95, 050407.

(7) Khersonskii, V. K.; *Astrophysics and Space Science*, **1984**, 98, 255.

(8) Baber, W. G.; Hasse, H. R.; *Proc. Cambridge Phil. Soc.* **1935**, 31, 564.

(9) Wind, H.; *J. Chem. Phys.* **1965**, 42, 2371.

(10) (a) Hunter, G.; Gray, B. F.; Pritchard, H. O.; *J. Chem. Phys.* **1966**, 45, 3806. (b) Hunter, G.; Pritchard, H. O.; *ibid.* **1967**, 46**,** 2146. (c) Hunter, G.; Pritchard, H. O.; *ibid.* **1967**, 46, 2153.

(11) Kullie, O.; Kolb, D.; *Eur. Phys. J. D.* **2001**, 17, 167.

(12) Franke, R.; Kutzelnigg, W.; *Chem. Phys. Lett.* **1992**, 199, 561.

(13) Alexander, S. A.; Coldwell, R. L.; *Phys. Rev. E* **1999**, 60, 3374.

(14) Parpia, F. A.; Mohanty, A. K.; *Chem. Phys. Lett.* **1995**, 238, 209.

(15) L. La John and J. D. Talman, Chem. Phys. Lett. **189**, 383 (1992)

(16) Kullie, O.; Kolb, D.; Rutkowski, A.; *Chem. Phys. Lett.* **2004**, 383, 215.

(17) Pavlik, P. I. ; Blinder, S. M.; *J. Chem. Phys.* **1967**, 46, 2749.

(18) Baylis, W. E.; Drake, G. W. F.; *Atomic, Molecular, & Optical Physics Handbook*, edited

by G. W. F. Drake (AIP Press, New York, 1996)

(19) About the GMP library, see http://swox.com/gmp/ and http://www.sc.nyu.edu/exact/gore/gmp/

(20) Computer code MAPLE, Waterloo Maple Inc., Waterloo, Ontalio, Canada.

(21) Kutzelnigg, W.; *Chem. Phys.* **1997**, 225, 203.

(22) (a) Grant, I. P.; *Atomic, Molecular, & Optical Physics Handbook*, edited by G. W. F. Drake (AIP Press, New York, 1996). (b) Grant, I. P.; Quiney, H. M.; *Phys. Rev. A* **2000**, 62, 022508.

(23) Hill, R. N.; Krauthauser, C.; *Phys. Rev. Lett.* **1994**, 72, 2151.

(24) Nakatsuji, H.; *Phys. Rev. A* **2002**, 65, 052122.

(25) Weinhold, F.; *J. Math. Phys.* **1970**, 11, 2127.

(26) Stevenson, A. F.; Crawford, M. F.; *Phys Rev.* **1938**, 54, 375.

(27) Temple, G.; *Proc. R. Soc., A.* **1928**, 119.

(28) Chen, Z.; Fonte, G.; Goldman, S. P.; *Phys Rev. A.* **1994**, 50, 3838.

(29) James, H. M.; *J. Chem. Phys.* **1935**, 3, 9.

(30) Yang, L.; Heinemann, D.; Kolb, D.; *Phys. Rev. A.* **1993**, 48, 2700.

(31) Peek, J. M.; *J. Chem. Phys.* **1965**, 43, 3004.

(32) Weinhold, F.; Chinen, A. B.; *J. Chem. Phys.* **1972**, 56, 3798.

(33) Wells, B. H.; Wilson, S.; *J. Phys. B* **1989**, 22, 1285.

(34) Schulze, W.; Kolb, D.; *Chem. Phys. Lett.* **1985**, 122, 271.

(35) Laaksonen, L.; Pyykko, P.; Sundholm, D.; *Int. J. Quantum Chem.* **1983**, 23, 309.

(36) Laaksonen, L.; Grant, I. P.; *Chem. Phys. Lett.* **1984**, 109, 485.

(37) Pestka, G.; *Physica Scripta*,**2004**, 69, 203.

(38) Zhang, Y. P.; Cheng, C. H.; Kim, J. T.; Stanojevic, J.; Eyler, E. E.; *Phys. Rev. Lett.* **2004**, 92, 203003.

(39) Nakatsuji, H.; Nakashima, H.; Kurokawa, Y.; Ishikawa, A.; *Phys. Rev. Lett.* **2007**, 99,

240402-1-4.

4.5 Appendix

In this appendix, we explain some necessary operations and integrals appearing in the non-relativistic and relativistic cases. Commonly, *m* stands for integers and *n* for zero and positive integers.

4.5.1 Non-relativistic case

For the ground state, the overlap and Hamiltonian integrals of H_2^+ molecule are easily done when the wave function is given by Eq. (22), i.e.,

$$\Psi = \sum_i c_i \lambda^{m_i} \mu^{n_i} \exp(-\alpha\lambda) \tag{A1}$$

The index n_i for μ is related to the symmetry of the state: even index for gerade states, odd for ungerade states. The Jacobian and the integration area is $d\lambda d\mu d\phi = R^3(\lambda^2 - \mu^2)/8$ and $\lambda: 1 \sim \infty,\ \mu: -1 \sim 1,\ \phi: 0 \sim 2\pi$, respectively. The resulting integrals are written generally as

$$I = \int_0^{2\pi} d\phi \int_1^{\infty} d\lambda \int_{-1}^{1} d\mu \lambda^m \mu^n \exp(-\alpha\lambda) \tag{A2}$$

The integration for μ is readily done. For positive integer *m*, the integration for λ is done with the incomplete gamma function as

$$\int_1^{\infty} \lambda^m \exp(-\alpha\lambda) d\lambda = \alpha^{-m-1} \Gamma(m+1, \alpha), \qquad (m = 0, 1, 2...) \tag{A3}$$

and for negative *m*, we use the formula for *m* = $|m|$

$$\int_1^{\infty} \frac{\exp(-\alpha\lambda)}{\lambda^m} d\lambda = \begin{cases} \exp(-\alpha) \sum_{k=1}^{m-1} \frac{(k-1)!(-\alpha)^{m-k-1}}{(n-1)!} - \frac{(-\alpha)^{m-1}}{(n-1)!} \exp(\alpha) Ei[-\alpha], & m \geq 2 \\ -Ei[-\alpha], & m = 1 \end{cases} \tag{A4}$$

4.5.2 Relativistic case

In this paper, both the non-relativistic case and the relativistic case are written by the

elliptic coordinate with $\lambda,\ \mu$ for clarity. However, in the relativistic case, it is convenient to use the transformed elliptic coordinate defined by

$$\lambda = \cosh(s), \quad \mu = \cos(t) \tag{A5}$$

We performed actual calculations in this transformed coordinate. The momentum operators are written as

$$\begin{aligned}
p_x &= -i\nabla_x = -i\left[\left\{\frac{2}{R}\frac{\cosh(s)\sin(t)\cos(\varphi)}{\cosh(s)^2-\cos(t)^2}\right\}\frac{\partial}{\partial s} - \left\{\frac{2}{R}\frac{\sinh(s)\cos(t)\sin(\varphi)}{\cosh(s)^2-\cos(t)^2}\right\}\frac{\partial}{\partial t} - \left\{\frac{2}{R}\frac{\sin(\varphi)}{\sinh(s)\sin(t)}\right\}\frac{\partial}{\partial \varphi}\right] \\
p_y &= -i\nabla_y = -i\left[\left\{\frac{2}{R}\frac{\cosh(s)\sin(t)\sin(\varphi)}{\cosh(s)^2-\cos(t)^2}\right\}\frac{\partial}{\partial s} - \left\{\frac{2}{R}\frac{\sinh(s)\cos(t)\sin(\varphi)}{\cosh(s)^2-\cos(t)^2}\right\}\frac{\partial}{\partial t} + \left\{\frac{2}{R}\frac{\cos(\varphi)}{\sinh(s)\sin(t)}\right\}\frac{\partial}{\partial \varphi}\right] \\
p_z &= -i\nabla_z = -i\left[\left\{\frac{2}{R}\frac{\sinh(s)\cos(t)}{\cosh(s)^2-\cos(t)^2}\right\}\frac{\partial}{\partial s} - \left\{\frac{2}{R}\frac{\cosh(s)\sin(t)}{\cosh(s)^2-\cos(t)^2}\right\}\frac{\partial}{\partial t}\right]
\end{aligned} \tag{A6}$$

The Jacobian is $dsdtd\phi = R^3\sinh(s)\sin(t)\left(\cosh(s)^2-\cos(t)^2\right)/8$ and the integration area is $s:0\sim\infty,\ t:-\pi\sim 0,\ \phi:0\sim 2\pi$. Then, the integral has a general form given by

$$I = \int_0^{2\pi} d\varphi \int_0^{\infty} ds \int_{-\pi}^{0} dt \frac{\cosh(s)^m \sinh(s)^{n_1} \cos(t)^{n_2} \sin(t)^{n_3} \exp(-\alpha\cosh(s))}{\left(\cosh(s)^2-\cos(t)^2\right)^{n_4}} \exp\left[i\left(j_z - 1/2\right)\varphi\right]. \tag{A7}$$

When $n_4 = 0$, the above integral is the same as Eq. (A2). In $n_4 \geq 1$ cases, the denominator causes a singularity at the nuclear position i.e. $s=0,\ t=-\pi$ or 0. However, some of these integrations are not singular when $\sinh(s)$ and $\sin(t)$ exist in the numerator since they also go to zero at singular points. When $n_4 = 1$, the integrals of Eq. (A7) are calculated by using the relation

$$\int_{-\pi}^{0} \frac{\sin(t)\cos(t)^k}{\cosh(s)^2-\cos(t)^2} = \cosh(s)^{k-1}\left[\sum_{r=0}^{\frac{k}{2}-1}\frac{\cosh(s)^{-k+2r+1}}{k-2r-1}\left\{1-(-1)^{-k+2r+1}\right\} + \ln\left(\frac{\cosh(s)-1}{\cosh(s)+1}\right)\right] \tag{A8}$$

and consequently, the one-dimensional (s coordinate) integrals reduce to

$$\int_0^{\infty} ds \sinh(s)^n \cosh(s)^m \ln\left(\cosh(s)\pm 1\right)\exp(-\alpha\cosh(s)) \tag{A9}$$

Most of these integrals were calculated analytically and the others numerically by using the mathematical program MAPLE.[19]

In the case of $n_4 \geq 2$, we used the following formula for the integration over t

$$\int_{-\pi}^{0} dt \frac{\cos(t)^i \sin(t)^j}{\left(\cosh(s)^2 - \cos(t)^2\right)^k} = -\frac{1}{\cosh(s)^{2k}} B\left(\frac{j+1}{2}, \frac{i+1}{2}\right) {}_2F_1\left(\frac{i+1}{2}, k; \frac{i+j}{2}+1, \frac{1}{\cosh(s)}\right) \quad \text{(A10)}$$

where F is the hypergeometric function. After the conversion of F, the resulting s integrants have the form similar to Eq. (A9).

Chapter 5

Solving the Schrödinger Equation of Atoms and Molecules without Analytical Integration Based on the Free Iterative Complement Interaction Wave Function

Abstract

Local Schrödinger equation (LSE) method is proposed for solving the Schrödinger equation (SE) of general atoms and molecules without doing analytic integrations over the complement functions of the free ICI (iterative complement interaction) wave functions. Since the free ICI wave function is potentially exact, we can assume a flatness of its local energy. Variational principle is not applicable because the analytic integrations over the free ICI complement functions are very difficult for general atoms and molecules. The LSE method was applied to several 2 to 5 electron atoms and molecules, giving the accuracy of 10^{-5} hartree in total energy. The potential energy curves of H_2 and LiH molecules were calculated precisely with the free ICI LSE method. These results show high potentiality of the free ICI LSE method for developing accurate predictive quantum chemistry with the solutions of the SE.

5.1 Introduction

Schrödinger equation (SE), $H\psi = E\psi$ provides a governing principle of chemistry, physics and biology and has an accurate predictive power.[1] For over 80 years after its birth, however, this equation has been thought not to be soluble except for a few special cases. Since 2000, we are formulating a general method of solving the SE of atoms and molecules in analytical expansion form.[2-15] First, we clarified the *mathematical structure of the exact wave function* and proposed a method, called iterative complement (or configuration) interaction (ICI) method, that gives a series of functions converging to the exact wave function.[2,3] This has been confirmed by applying the method to model harmonic oscillator[5] and to finite-basis expansion method.[6,7] However, this method includes the integrals of higher-powers of Hamiltonian, which diverge when the Hamiltonian involves singular operators like Coulomb potential.[8,9] This problem, called *singularity problem*, always occurs when we apply the method to atoms and molecules. However, this difficulty has been solved by introducing the inverse Schrödinger equation (ISE)[8] and the scaled Schrödinger equation (SSE).[9,12] The method based on the SSE was easier and more general.

5.2 Theory

The SE has a freedom to be written as the SSE,

$$g(H-E)\psi = 0\,, \tag{1}$$

where the scaling function $g(r)$ is positive everywhere and can be zero only at the singular points to scale the singularity to be finite (for details, see ref. [9]). The simplest ICI (SICI) based on the SSE

$$\psi_{n+1} = [1 + C_n g(H-E_n)]\,\psi_n \tag{2}$$

is guaranteed to converge to the exact wave function without encountering the singularity problem for the existence of the *g*-function.[9,12] Next, we define *free ICI* wave function as follows. We collect all the independent functions in the right hand side of Eq. (2) as $\{\phi_i\}^{(n)}$ (*i*

= 1, .., M_n), which we call complement functions, and give independent coefficient to each as[9,12]

$$\psi_{n+1} = \sum_{i=1}^{M_n} c_i \phi_i \tag{3}$$

This free ICI wave function converges faster, for an increased freedom, than the original SICI to the exact wave function. In the free ICI method, the g function can be chosen more freely than in the original ICI: when diverging terms appear, they are simply thrown out, since they are physically not acceptable as elements of the wave function. Starting from appropriate g and ψ_0, and increasing the order n, one gets the free ICI wave function having essentially exact structure. By exact structure, we mean that after the variables $\{c_i\}$ are determined by the method equivalent to the SE, the wave function becomes exact.

When we apply variational principle to the free ICI wave function, we obtain secular equation that involves Hamiltonian and overlap integrals. When analytic integrations of these terms are possible, the variational principle gives very accurate results. Actually, we could calculate quite accurate wave functions of helium,[15] hydrogen molecule,[13] etc.: for helium, the free ICI method gave the energy correct to 40 decimal figures in comparison with 36 of the published result of Schwartz.[16] For H_2, the result given below is more accurate than before.[13,17] These are the numerical proofs of the accurateness and effectiveness of the free ICI method.

However, different from differentiations, analytic integrations are not always possible, in principle, for arbitrary analytic functions. This is true also for the ICI complement functions. Numerical integration methods are usually insufficient for accuracy and computational cost. We call this difficulty *integration difficulty*, because without solving this difficulty, we cannot apply the present methodology to general atoms and molecules. The purpose of this communication is to show a solution to this problem. We will use the SE directly instead of the variational principle. Our strategy lies in the constancy of the local

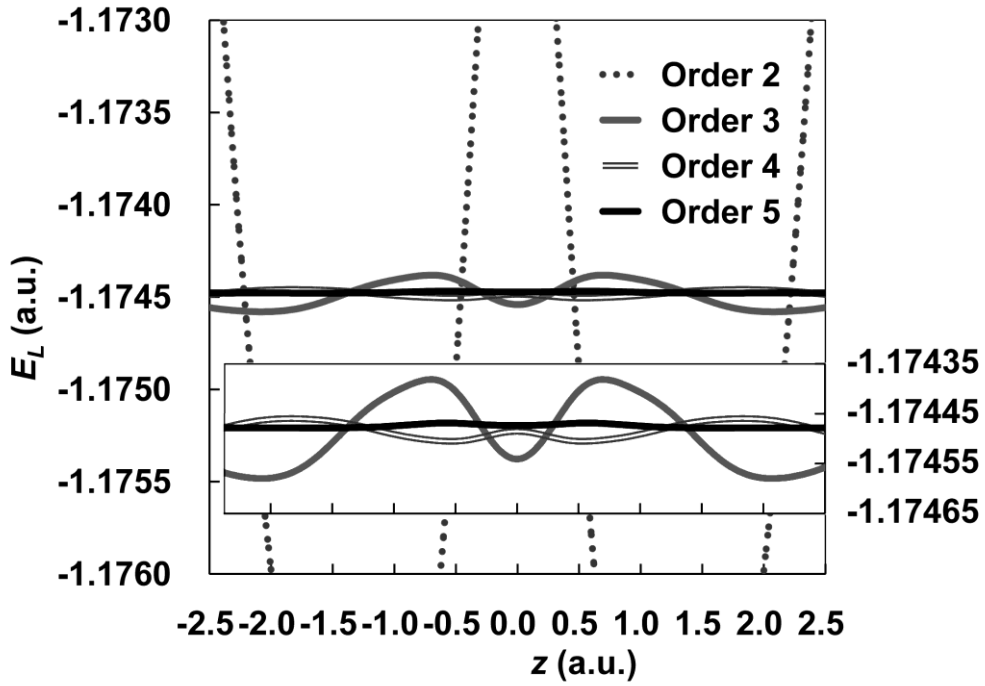

Fig. 1. Local energy plots (with enlargement) for the hydrogen molecule.

energy for the exact wave function.

5.1 Local energy of H_2

Previously, we reported the free ICI variational calculations of H_2 of order 4.[13] We have performed here the same calculations to order 5, which consisted of 6776 functions and gave the energy E = -1.174 475 931 400 027 au, which is lower than the energy E = -1.174 475 931 399 840 au of Sims and Hagstrom,[17] who used 7034 James-Coolidge type functions. So, the present free ICI wave function is variationally best. The structures of the two wave functions are similar, but ours has a bit larger freedom, so that it could give a better result.[13] We showed previously that the free ICI wave function satisfied accurately both nuclear and electron cusp conditions. We show here that it also satisfies the local energy relation, $H\psi(r)/\psi(r) = E_{\text{exact}}$, i.e., the SE itself, at any coordinate r except for the regions very near the nucleus or another electron. Fig. 1 shows the local energy plots, when one electron is at the center of the two protons at z = ±1.4011/2 au and the other moves 1 au apart from the H-H

axis. The local energy for n = 5 is essentially constant everywhere on this axis and is within -1.17447 ± 0.00001 au. This shows that the free ICI method gives not only accurate energy, but also accurate wave function even locally. This result also constitutes a supporting basis for developing the LSE method below.

5.2 LSE method

Precisely, the SE is a local equation: $H\psi(r_\mu) = E\psi(r_\mu)$ stands at any coordinate r_μ in atoms and molecules. Suppose that there are M unknown parameters in the ψ that has an exact structure. Then, we take M independent sampling points, μ = 1,.., M, in the coordinate space, which gives M independent simultaneous equations that connect these M unknown variables. Therefore, in principle, these M variables can be determined. Note that this argument is possible only when the wave function we are dealing with has an exact structure, or is potentially exact, so that its local energy can be assumed to become flat and E_{exact} everywhere: the SE itself is satisfied. Our free ICI wave function is certainly potentially exact, when the order n is sufficiently large. We have already seen in Fig. 1 that the local energy of the free ICI wave function of H_2 is flat and E_{exact} in high accuracy for n = 5.

Inserting the free ICI wave function into the SE, we obtain

$$\mathbf{AC} = \mathbf{BCE} \tag{4}$$

where $\{A_{\mu i}\} = \{H\phi_i(r_\mu)\}$, $\{B_{\mu i}\} = \{\phi_i(r_\mu)\}$, $\mathbf{C} = \{\mathbf{c}^0, \mathbf{c}^1, \cdots\}$, and $\mathbf{E}$ is a diagonal matrix with the elements, E_0, E_1, etc. The suffices 0, 1, etc. denote ground, first excited, etc. states. The free ICI coefficient vector $\mathbf{c}^k$ has the elements c_i^k for the k-th state. Both $\mathbf{A}$ and $\mathbf{B}$ are square matrices when we select M sampling points, but highly non-symmetric.

Multiplying $\mathbf{B}^T$ from the left, we obtain

$$\mathbf{HC} = \mathbf{SCE} \tag{5}$$

TABLE I. Results of the free ICI LSE calculations of small atoms and molecules.

	Elec.	Order	*M*	Energy (LSE) (a.u.)	Energy (Best ref.) (a.u.)	ΔE=LSE-Best ref.	Ref.
He	2	6	100	-2.903 724 52	-2.903 724 37	-1.5×10^{-7}	21
Li^+	2	6	100	-7.279 914 33	-7.279 913 41	-9.2×10^{-7}	22
H_2	2	5	388	-1.174 474 77	-1.174 475 93	1.2×10^{-6}	13,17,21
HeH^+	2	5	388	-2.978 718	-2.978 706	-1.2×10^{-5}	21
Li	3	6	1496	-7.478 043	-7.478 060	1.7×10^{-5}	21,23
Be^+	3	6	1496	-14.324 753	-14.324 763	1.0×10^{-5}	24
He_2^+	3	6	2632	-4.994 646	-4.994 644	-2.0×10^{-6}	21
Be	4	4	1770	-14.667 300	-14.667 355	5.5×10^{-5}	21
B^+	4	4	1770	-24.348 847	-24.348 883	3.6×10^{-5}	21
LiH	4	4	2645	-8.070 516	-8.070 553	3.7×10^{-5}	21
B	5	4	15038	-24. 653 872	(-24.653 93)[a]	(5.8×10^{-5})	25

[a] Estimated value from experiments.[25]

where $\mathbf{H} = \mathbf{B}^T\mathbf{A}$ and $\mathbf{S} = \mathbf{B}^T\mathbf{B}$, which are square matrices. The **S** matrix is symmetric and positive semi-definite and its element is $S_{ij} = \sum_\mu \phi_i(r_\mu)\phi_j(r_\mu)$: it becomes overlap integral when the sampling covers all the space. Similarly, the **H** matrix has the meaning of Hamiltonian matrix and is almost symmetric. Therefore, Eq. (5) is more easily handled than Eq. (4) as a diagonalization equation. We note that we may multiply $\mathbf{A}^T$, instead of $\mathbf{B}^T$, from the left of Eq. (4) and use the resultant equation for calculating **C** and **E**, which is useful for the relativistic case since it corresponds to the inverse Hamiltonian treatment.[10]

When we use Eq. (5), the number of the sampling points may exceed the number of the variables, *M*. This has a merit when we do random sampling where the independence among the sampling points may not be guaranteed. By increasing the number of the sampling points, the matrices **A** and **B** become rectangular but the matrices **H** and **S** are always square of dimension *M*. Note however that Eq. (4) is more informative than Eq. (5): for example, one can always get Eq. (5) from Eq. (4), but the converse is not true.

In the applications below, we used standard Monte Carlo sampling.[18] This does not mean that we solved the variational equation by Monte Carlo integration method, whose accuracy is generally not good enough. For the non-variational nature of the present method, the error in the wave function would be of the same order as that in the energy.

5.3 Results and Discussions

5.3.1 Applications to 2 to 5 electron atoms and molecules

The results of the free ICI LSE calculations are given in Table I. The calculations were performed in two steps: first, the free ICI complement functions $\{\phi_i\}$ were generated and then the unknown coefficients[31] were calculated by the LSE method.

In the first free ICI step, we used the g function of $g = 1 + \sum_{i,A} r_{iA} + \sum_{i<j} r_{ij}$, where A denotes nucleus and i,j electrons. The initial function ψ_0 was different for different systems. For helium, we used logarithmic function $\psi_0 = [1 + \ln(r_1 + r_2)]\exp[-\alpha(r_1 + r_2)]$, which describes the effect of three particle interaction near the nucleus.[19,20] For atoms, the ψ_0 including logarithmic functions gave faster convergence than the one not including them, so that we used them for the atoms except for B, for which we used double-zeta initial guess for the 1s core. For molecules, covalent plus ionic initial function was used because it gave better convergence than the covalent-alone one. For H_2, the covalent function is defined by $\psi_0^C = \exp(-\alpha r_{1A})\exp(-\alpha r_{2B})$ and the ionic one by $\psi_0^I = \exp(-\alpha r_{1A})\exp(-\alpha r_{2A})$. These expressions are short-handed: we imposed all the symmetries before calculations. For He_2^+ only covalent function was used.

In the second step, the variables $\{c_i\}$ were determined by the LSE method. The present calculations were done with the HS matrix method, Eq. (5) and the numbers of the sampling were $\sim 10^7$. Since we did not constrain any cusp conditions, we did not sample the points in the region near the nucleus or another electron, $r \le 0.03/Z$, where Z is the charge of the nucleus or electron. We calculated the wave function, energy, and H-square error (variance) σ^2 that is zero for the exact wave function. At the final stage of the sampling, we calculated σ^2 ten times at fixed interval and took minimum σ^2 data as the final result.

TABLE II. Comparison of full CI and free ICI LSE calculations for 4-electron Be and LiH.

	Exact energy (a.u.)	Full CI[a]				Free ICI LSE			
		Basis set	M	Energy (a.u.)	Δ^b	n	M	Energy (a.u.)	Δ^b
Be	-14.667 355	9s9p5d3f2g	3.1×10^6	-14.656 767	1.1×10^{-2} a.u. 6.6 kcal/mol	4	1770	-14.667 300	5.5×10^{-5} a.u. 0.034 kcal/mol
LiH	-8.070 553	11s8p6d1f /9s8p6d1f	4.45×10^7	-8.069 336	1.2×10^{-3} a.u. 0.76 kcal/mol	4	2645	-8.070 516	3.7×10^{-5} a.u. 0.023 kcal/mol

[a] Reference 26. [b] Difference from the best reference energy (see Table I).

The free ICI LSE calculations were done for two- to five-electron closed- and open-shell atoms and molecules and compared with the very accurate reference data.[21-24] For B, the value in parentheses is the estimated exact energy.[25] Table I shows that the present method is highly accurate, the energy errors being less than 6×10^{-5} hartree (0.04 kcal/mol). This is remarkable, since the present method involves no analytic integration at all. The order of ICI must be larger than 4 for getting sufficient accuracy for chemical studies. The numbers of the complement functions, M, were small. Though we used standard Monte Carlo sampling, we will examine more efficient sampling method.

Thus, being free from the integration difficulty, the present free ICI LSE method has a high potentiality as a useful tool for calculating accurate analytic solutions of the SE of general atoms and molecules. This is necessary for building up a new frontier of quantum chemistry as accurately predictive science.

For the small systems shown in Table I, very accurate reference data of the exact energy were available in the literature. However, for systems with larger number of electrons, very accurate reference data are scarcely available.[21] Therefore, to examine the accuracy of the calculated results, accurate theory of error bars would become necessary in future.[27,28]

Now, let us compare the present method with full CI, which was only one available general method of solving the SE within finite basis space. Table II gives a comparison for Be

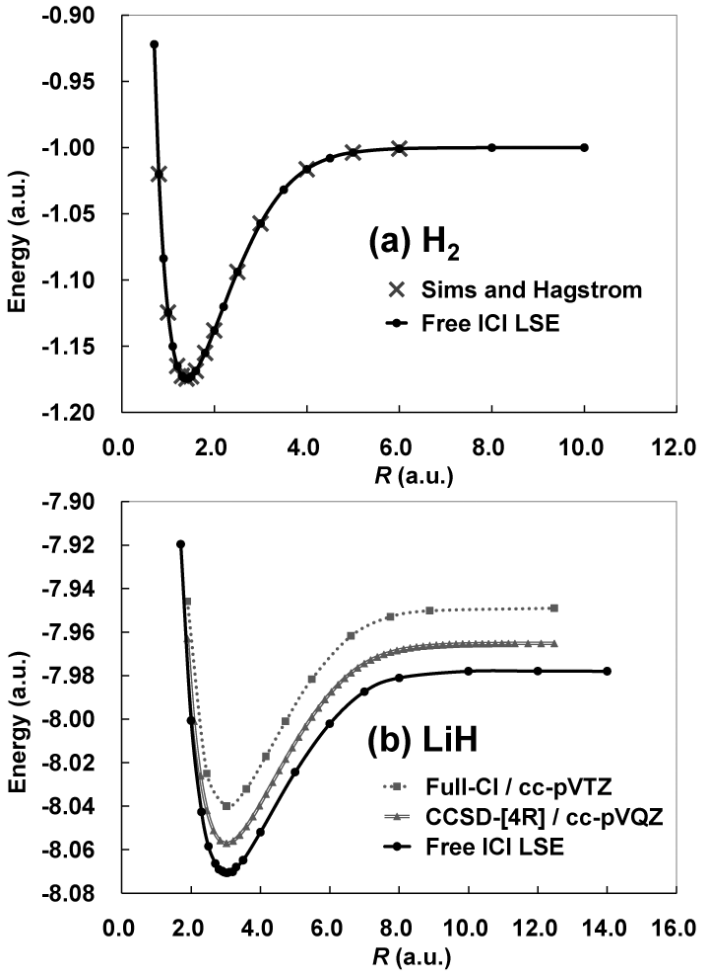

Fig. 2. Free ICI LSE potential curves of (a) H_2 compared with the accurate results[17] and (b) LiH compared with the full CI and CCSD-[MR] results.[29]

and LiH.[26] The basis sets used in the full CI were quite extensive including up to f and g functions, but the energy error was 6.6 kcal/mol for Be and 0.76 kcal/mol for LiH. Though the full CI requires very large number of variables, the solutions are usually far from the true solutions of the SE, because of the incompleteness of the basis sets. This is a reason why we need an analytical theory for solving the SE.

5.3.2 Potential curves of H_2 and LiH

In chemistry, potential energy curves provide basic information on the structures, spectroscopy and chemical reactions of molecules. Here, we apply the present free ICI LSE

method for calculating accurate potential energy curves of H_2 and LiH. The initial functions, the free ICI complement functions and their exponents (1.2 for H_2) were the same as in Table I for all the internuclear distances, *R*. This is different from other calculations.[17,21]

Fig. 2a shows the calculated potential curve of H_2. The free ICI LSE calculations were done for *R* = 0.7 - 10.0 au. We chose many distances to be the same as those of Sims and Hagstrom,[17] which permits a direct comparison with their accurate values. The maximum difference was 5.9×10^{-5} au at *R* = 0.8 au. The difference decreased gradually as *R* increased: at *R* = 5 au, the difference was 1.3×10^{-6} au. Actually, in this accuracy, the present potential curve of Fig. 2a overlaps completely with that of Sims and Hagstrom.

Fig. 2b shows the calculated potential curve of LiH. The calculations were done for 22 different distances from 1.7 to 14.0 au. Near the equilibrium distance, 3.015 au, we took dense sampling. As *R* was elongated, the energy approached the sum of the energies of Li and H atoms, -7.9780 au. The potential curves of the full CI method and the CCSD-[MR] method due to Li and Paldus[29] were given for comparison.

The potential energy curves of H_2 and LiH given in Fig. 2 and their associated wave functions include much information that is worth examined in detail. Such analyses will be published elsewhere.

5.4 Conclusions

We have shown in this communication that the accurate analytic solutions of the SE can be calculated by the free ICI LSE method without doing analytic integrations over the complement functions. The results calculated with this method were certainly precise. We note that the order *n* of the free ICI method need not increase as the size of the system increase, since the order is related to the number of electrons (2*n* electrons) directly correlated to each other.

Since the present free ICI LSE method is general, having no essential difficulty, it can

be formulated for solving the SE of general atoms and molecules. The problems left are to develop efficient algorithms and computing. We note that this method is suitable for super-parallel computers developed and being developed in recent years. This is different from other accurate quantum chemistry codes.

By making the present methodology efficient, we hope we would be able to construct truly accurate and predictive quantum chemistry based on the solutions of the SE. If we can further extend it to simulation methodology, we would be able to reproduce ‘nature’ itself from the principles of quantum mechanics alone. This is indeed our goal.

Acknowledgements

Thanks are due to the support from the Grant for Creative Scientific Research from the Ministry of Education, Science, Culture, and Sports of Japan.

References

(1) Dirac, P. A. M.; Proc. Roy. Soc. (London), A, **1929**, 123, 714.

(2) Nakatsuji, H.; *J. Chem. Phys.* **2000,** 113, 2949.

(3) Nakatsuji, H.; Davidson, E. R.; *J. Chem. Phys.* **2001**, 115, 2000.

(4) Nakatsuji, H.; *J. Chem. Phys.* **2001**, 115, 2465.

(5) Nakatsuji, H.; *J. Chem. Phys.* **2002**, 116, 1811.

(6) Nakatsuji, H.; Ehara, M.; *J. Chem. Phys.* **2002**, 117, 9.

(7) Nakatsuji, H.; Ehara, M.; *J. Chem. Phys.* **2005**, 122, 194108.

(8) Nakatsuji, H.; *Phys. Rev. A* **2005**, 65, 052122.

(9) Nakatsuji, H.; *Phys. Rev. Lett.* **2004,** 93, 030403.

(10) Nakatsuji, H.; Nakashima, H.; *Phys. Rev. Lett.* **2005,** 95, 050407.

(11) Nakatsuji, H.; *Bull. Chem. Soc. Jap.* **2005**, 78, 1705.

(12) Nakatsuji, H.; *Phys. Rev. A,* **2005**, 72, 062110.

(13) Kurokawa, Y.; Nakashima, H.; Nakatsuji, H.; *Phys. Rev. A*, **2005**, 72, 062502.

(14) Nakashima, H.; Nakatsuji, H.; *submitted.*

(15) Nakashima, H.; Nakatsuji, H.; *J. Chem. Phys. in press.*

(16) Schwartz, C.,; *Int. J. Mod. Phys. E,* **2006**, 15, 877.

(17) Sims, J. S.; Hagstrom, S. A.; *J. Chem. Phys.* **2006**, 124, 094101.

(18) Hammond, B. L.; Lester, Jr., W. A.; Reynolds, P. J.; *Monte Carlo Methods in Ab Initio Quantum Chemistry* (World Scientific, Singapore, 1994).

(19) Bartlett, J. H.; *Phys. Rev.* **1937**, 51, 661.

(20) Fock, V.; *Izv. Akad. Nauk. SSSR, Ser. Fiz.* **1954**, 18, 161.

(21) Rychlewski, J.; Komasa, J.; *Explicitly Correlated Wave Functions in Chemistry and Physics - Theory and Applications*, Ed. J. Rychlewski (Kluwer Academic, Dordrecht, 2003).

(22) Thakkar, A. J.; Koga, T.; *Theo. Chem. Acc.* **2003**, 109, 36.

(23) Puchalski, M.; Pachucki, K.; *Phys. Rev. A* **2006**, 73, 022503.

(24) Yan, Z.; Tambasco, M.; Drake, G. W. F.; *Phys. Rev. A* **1998**, 57, 1652.

(25) Galvez, F. J.; Buendia, E.; Sarsa, A.; *J. Chem. Phys.* **2005**, 122, 154307.

(26) Bendazzoli, G. L.; Monari, A.; *Chem. Phys.* **2004**, 306, 153.

(27) Temple, G.; *Proc. R. Soc. London, Ser. A* **1928**, 119, 276.

(28) Weinhold, F.; *Phys. Rev.* **1969**, 183, 142.

(29) Li, X.; Paldus, J.; *J. Chem. Phys.* **2003**, 118, 2470.

General Conclusion

In this thesis, the author developed the methods to solve exactly the Schrödinger and Dirac equations (SE and DE, respectively) and also applied modern electronic structure theory to large reaction systems containing transition metal element. In Part I of the thesis, the author presented theoretical studies on chemical reactions by transition metal complexes. In Part II, he developed the methodology to solve the SE and the DE. These studies provide the well understanding and reliable knowledge of complex chemical reactions by transition metal complexes and the exact solution of the SE and the DE. The main conclusions presented in this thesis are summarized, as follows:

In chapter 1, the oxygen atom transfer reactions of iridium and osmium complexes were theoretically investigated with the DFT method. In small model systems in which bulky substituents were replaced with methyl groups, the μ-oxo dinuclear iridium and osmium complexes were optimized as stable species, indicating that the oxygen atom transfer reaction does not occur in model systems. In real systems, on the other hand, the transition states of both iridium and osmium reactions were successfully optimized. The activation barrier in gas phase is calculated to be 3.9 and 33.3 kcal/mol for the iridium and osmium reaction systems, respectively, in the potential energy surface. The $\Delta G^{0\ddagger}$ value was evaluated to be 8.8 and 43.8 kcal/mol for the iridium and osmium reaction systems, respectively, in solution at 298.15 K. These results were consistent with experimental results that the oxygen atom transfer reaction rapidly occurs in the iridium system but very slowly in the osmium system. The origin of the large difference in the activation barrier was discussed in terms of nuclear and electronic factors. The nuclear factor arises from re-organization energy which is defined as the destabilization energy necessary to distort the complex from the reactant into the transition

state structure. The nuclear factor is much larger in the osmium system than in the iridium system. In the osmium reaction system, the activation barrier without re-organization energy is about 70 % of the total activation barrier, indicating that the nuclear factor largely contributes to the difference in the reactivity between the iridium and osmium complexes but the electronic factor also contributes to the difference. The larger nuclear factor of osmium system arises from the fact that substantially large structural changes must occur upon going from trigonal planar **Os(NAr)$_3$** to the tetrahedral-like transition state. The small re-organization energy of the iridium system arises from the fact that little structural change occurs upon going from the reactant to the transition state. The electronic factor was discussed in terms of the interaction between the donor orbital of ML_3 and the acceptor orbital of ML_3=O. Since the donor and acceptor orbitals are similar between the iridium and osmium complexes, it is likely that the extent of orbital overlap is similar between these two systems. However, the energy gap between the donor and acceptor orbitals is much larger in the osmium reaction system than in the iridium reaction system, which leads to the smaller electronic factor in the osmium system than in the iridium system. The large energy gap in the osmium system arises from both the electron donor and electron acceptor orbitals; the electron donor orbital of **Os(NAr)$_3$** is at much lower energy than that of **Ir(Mes)$_3$** since osmium center takes +6 oxidation state while iridium center takes +3 oxidation state.

In chapter 2, the synthetically useful arene cross-coupling reaction promoted by $Pd(OAc)_2$ was theoretically studied with the DFT, MP2 to MP4(SDQ), and CCSD(T) methods. Benzoquinone (BQ) is experimentally reported to be necessary for this cross-coupling reaction. The computational study elucidated the whole mechanism of this arene cross-coupling reaction and the role of BQ. In this reaction, two C-H activations occur independently. The first is the C-H activation of benzo[h]quinoline (Bzq), which leads to the formation of Pd(Bzq)(η^2-OAc). This process is understood in terms of heterolytic type C-H activation. BQ easily coordinates to Pd(Bzq)(η^2-OAc) to afford the trigonal bipyramidal

Pd(II) complex Pd(Bzq)(η^2-OAc)(BQ). The coordinate bond is formed by the CT from the Pd to the BQ. This complex Pd(Bzq)(η^2-OAc)(BQ) is as stable as the square planar Pd(Bzq)(η^2-OAc). Both E_a and $\Delta G^{0‡}$ are small for the BQ coordination step, indicating that this step easily occurs. Then, the C-H activation of benzene occurs with $\Delta G^{0‡}$ value of 27.5 kcal/mol to afford the intermediate. Finally, the reductive elimination (RE) readily occurs with nearly no barrier; the $\Delta G^{0‡}$ value for this step is quite small (0.4 kcal/mol). These computational results suggest that the rate-determining step is the C-H activation of benzene by Pd(Bzq)(η^2-OAc)(BQ). To clarify the role of BQ, we investigated the cross-coupling reaction of HBzq and benzene in the absence of BQ. The greatest difference from the reaction in the presence of BQ is observed in the structure of the intermediate before the RE; in the absence of BQ, the phenyl group is on the Pd-Bzq-HOAc planar in contrast to that in the presence of BQ in which the phenyl group takes the equatorial position of the trigonal bipyramidal structure. As a result, the RE step in the absence of BQ occurs with quite large geometry changes, but the RE occurs with moderate geometry changes in the presence of BQ. In addition to the smaller geometry changes, BQ stabilizes **TS_{3b}** and **P_3** by the back-donation from Pd(0) to BQ. Actually, the considerably large difference is observed in $\Delta G^{0‡}$ and ΔG^0 of the RE step; in the presence of BQ, the $\Delta G^{0‡}$ and ΔG^0 are 0.4 and -18.5 kcal/mol, respectively, while in the absence of BQ, the $\Delta G^{0‡}$ and ΔG^0 are 34.7 and 8.7 kcal/mol, respectively. Our theoretical study clearly shows that BQ plays very important role in the RE step to accelerate the arene-arene cross-coupling reaction.

In chapter 3, photoinduced epoxidation reaction of olefins catalyzed by [Ru(TMP)(CO)] was theoretically investigated. This reaction exhibits high quantum yield (0.60) and stereoselectivity of produced epoxides. However, the detailed mechanism of the reaction is not clear, especially at the olefin epoxidation step. The author mainly investigated the olefin epoxidation step catalyzed by $[Ru(TMP)(CO)(O)]^-$, and ascertained that the CASSCF and the DFT methods provided similar electronic structures of important

Ru-porphyrin species. From the computational results, the author clarified the electronic process of the olefin epoxidation reaction, as follows: i) Both the olefin adduct [Ru(Por)(CO)(olefin)] and the transition state have unsymmetrical geometries with respect to the Ru center and two C atoms of the olefin. This means that the reaction does not occur via concerted oxene insertion mechanism. ii) In the olefin adduct, the unpaired electron is localized on one C atom of the olefin. iii) The unpaired electron transfers from the olefin carbon atom to the porphyrin ring around the transition state. iv) The substrate dependence was investigated by employing *n*-hexene and styrene as examples. Though the stability of the olefin adduct is considerably different between them, the substrate dependence of the activation barrier is not large (within 5 kcal/mol). v) The Ru center keeps +II oxidation state during the epoxidation reaction. vi) The electronic structure changes mainly occur in the olefin moiety, the porphyrin ring, and the oxo lone pair orbital. The author believes that this study is helpful for the further development of the biomimetic reaction by metalloporphyrins.

In chapter 4, the author showed that the FC method combined with the variational principle provides very accurate analytic wave functions of H_2^+ efficiently in both nonrelativistic and relativistic cases. For the nonrelativistic case, the author compared two analytical expansions conversing to the exact wave function, the so-called exact wave function and the present FC wave function. It was shown that the FC method was even more efficient than solving the exact wave function of H_2^+. For the relativistic case, the first application of the FC method to molecule was presented. An appropriate choice of the *g* function is crucial for describing the correct balance between the large and small components of the FC wave function. By using the inverse Hamiltonian method, the variational collapse problem was avoided and the calculated energy was an upper bound of the ground state energy. The present relativistic FC calculations reasonably showed fast convergences in both the ground and excited states. The author further calculated the lower bounds of the relativistic energy. The knowledge of both the upper and lower bounds of the relativistic

energy showed that the present relativistic wave function and energy were very accurate with the energy error being less than 4.3×10^{-2} cm^{-1}. Thus, the author successfully presented that the FC methodology can give quite accurate solutions for both the SE and the DE of H_2^+.

In chapter 5, the author has shown that the accurate analytic solutions of the SE can be calculated by the FC method combined with the LSE method which does not need analytic integrations over the complement functions. The results calculated with this method were certainly precise. It should be noted that the order *n* of the FC wave function does not necessarily increase as the size of the system increases, since the order is related to the number of electrons (2n electrons) directly correlated to each other. Since the present FC-LSE method is general, and does not have essential difficulty, it can be formulated for solving the SE of general atoms and molecules. The remaining problems are developing efficient algorithms and computational techniques. It should be emphasized that the FC-LSE method is suitable for super-parallel computers developed and being developed in recent years. This is different from other accurate quantum chemistry codes. By making the present methodology efficient, the author hope that constructing truly accurate and predictive quantum chemistry based on the solutions of the SE would be possible in the near future.

As described above, the new and valuable understanding and correct knowledge of both the methodology and the application of *ab initio* electronic structure theory were presented in this thesis. The author successfully presented exact wave functions of small systems with the new FC method in both non-relativistic and relativistic cases. Also, the author reported that many valuable insights into the complicated reactions by the transition metal complex are successfully provided by the *ab initio* electronic structure theory such as DFT and post Hartree-Fock methods. The author believes that these results are invaluable for developing accurate theory and reliable application of theoretical and computations to the complex reactions.

List of Publications

Publications included in this thesis

Chapter 1

"Oxygen Atom Transfer Reactions of Iridium and Osmium Complexes: Theoretical Study of Characteristic Features and Significantly Large Differences Between These Two Complexes"

Atsushi Ishikawa, Yoshihide Nakao, Hirofumi Sato, and Shigeyoshi Sakaki

Inorg. Chem. **2009**, *48*, 8154-8163

Chapter 2

"Pd(II)-promoted Direct Cross-coupling Reaction of Arenes via Highly Regioselective Aromatic C–H Activation: A Theoretical Study"

Atsushi Ishikawa, Yoshihide Nakao, Hirofumi Sato, and Shigeyoshi Sakaki

Dalton Trans., **2010**, *39*, 3279–3289

Chapter 3

"Theoretical Study of Photoinduced Epoxidation of Olefins Catalyzed by Ruthenium Porphyrin"

Atsushi Ishikawa and Shigeyoshi Sakaki

J. Phys. Chem. A, submitted.

Chapter 4

"Solving the Schrödinger and Dirac Equations of Hydrogen Molecular Ion Accurately by

the Free Iterative Complement Interaction Method”

Atsushi Ishikawa, Hiroyuki Nakashima, and Hiroshi Nakatsuji

J. Chem. Phys. **2008**, *128*, 124103

Chapter 5

“Solving the Schrödinger Equation of Atoms and Molecules without Analytical Integration Based on the Free Iterative-Complement-Interaction Wave Function”

Hiroshi Nakatsuji, Hiroyuki Nakashima, Yusaku Kurokawa, and Atsushi Ishikawa

Phys. Rev. Lett. **2007**, *99*, 240402